



PhD course:

"Environmental and Energy Engineering Science"

XXXIII cycle

Title of thesis:

"Development and characterization of anti-bacterial and corrosion resistant surface treatments on medical grade Ti grade 2 and Ti grade 5"

PhD Student

Bruno Filipe Gomes Ribeiro

Supervisor

Prof. Lorenzo Fedrizzi

Co-supervisor

Dr. Maria Lekka

Ing. Elisa Salatin

2021

PREFACE

This Ph.D thesis is the result of 3 years of research performed under the project “Development and characterization of anti-bacterial and corrosion resistance surface treatments on micro-porous substrates”, under joint supervision of LimaCorporate, SpA and the University of Udine. This research was realized within the framework of the Innovative Training Network mCBEEs (Advanced integrative solutions to Corrosion problems beyond micro-scale: towards longterm durability of miniaturized Biomedical, Electronic and Energy systems).

The mCBEEs Innovative Training Network is a joint venture between academia and industry with a primary goal to train young researchers in the field of corrosion and corrosion protection of micro- and nanodevices. The network focuses on the study of corrosion mechanisms beyond microscale of components in miniaturized systems in different environments using localized techniques, and the development of multifunctional protective coatings to increase the long-term durability of such components. The ITN brought together 15 Early-Stage Researchers (ESRs) enrolled by 9 Universities, 3 Research Centers and 3 Companies belonging to 11 Countries.

Withing the mCBEEs network I was contracted by LIMACorporate SpA and enrolled in the PhD school of Environmental and Energy Engineering Science of University of Udine. The research activities were mainly undertaken at the department of Research and Development for Additive Manufacturing of LimaCorporate, under the supervision of Elisa Salatin, in close collaboration with the Polytechnic Department of Engineering and Architecture of the University of Udine, with the Materials Engineering research group led by prof. Lorenzo Fedrizzi. Parts of research work were performed in secondment periods to partner institutions of the mCBEEs network. Atomic layer deposition of Al_2O_3 and HfO_2 coatings onto TiO_2 nanotubes (not included in this thesis) was performed at the Department of Physical and Organic Chemistry of Jozef Stefan Institute, under the supervision of prof. Ingrid Milosev, in Ljubljana, Slovenia. Antibacterial and biocompatibility tests were performed in collaboration with the groups of NanoBiomaterials for Targeted Therapies, under the supervision of Prof. Ana Paula Pego, and BioEngineered Surfaces, under the supervision of Prof. Cristina Martins, at INEB, in Porto, Portugal.



This project has received funding by the European Union's Horizon 2020 research and innovation programme under the Marie Skłodowska-Curie grant agreement No. 76977.

ABSTRACT

Titanium alloys are widely used materials in orthopedic implants due to their superior mechanical and chemical compatibility, and their ability to osseointegrate in host bone, when compared with other commonly used alloys, namely, 316 L stainless steel and Co-Cr alloys. Nevertheless, these materials still face several challenges, and the focus of development has progressively shifted to an even more improved biocompatibility, in terms of bioactivity, reduced toxicity and fast osteointegration, as well as a decreased susceptibility to microbial colonization. In this aspect, infection around titanium implants continues to be a concern in the medical field. Implants provide niche environments, with decreased host-defenses where microorganisms such as bacteria can adhere and form biofilms, sessile communities that protect these microorganisms from the action of antibiotics or the host immune system, allowing them to replicate and propagate into various locations in the human body. Thus, the occurrence of infection results in the necessity of further antibiotic therapy and eventual removal of the device, with an increased hospitalization time and healthcare cost, posing a threat to the patient's life.

In this aspect, surface modification of Titanium-based alloys through the production TiO_2 nanotubes on their surface, has been widely regarded both as surface treatment that provides it with an increased bioactivity, but also as reservoirs and carriers for local delivery of antimicrobial agents. In this work, production of TiO_2 nanotubes on the surface of the most common medical grade titanium alloys, Cp-Ti and Ti6Al4V has been achieved through electrochemical anodization. It was shown that, by successfully controlling specific process parameters, namely, electrolyte composition, applied potential difference and process time, well-defined nanotubular structures with target inner diameters of 70-100 nm can be obtained on both alloys. Moreover, post-anodizing heat treatments were performed that successfully converted the produced amorphous anodic oxide into a crystalline anatase phase, which confers to these nanotubular structures an increased stability. This surface treatments were evaluated in terms of corrosion resistance through potentiodynamic polarization measurements and have been shown to lead to an overall improve of the corrosion resistance in the potential range of the human body. Lastly, when decorated, through electroless and electrochemical deposition processes, with inorganic antimicrobial agents (Ag, Cu and Zn) they have been shown to significantly decrease the viability of one of the most common implant infections pathogens, *Staphylococcus epidermidis*.

TABLE OF CONTENTS

Preface	i
Abstract	iii
Table of Contents	v
Abbreviations	ix
Acknowledgments	xi
1. Theoretical Remarks	1
1.1 Titanium and titanium alloys in orthopaedic implants	1
1.1.1 Microstructure of Ti alloys	4
1.1.2 Corrosion resistance	5
1.1.3 Mechanical properties	6
1.1.4 Biocompatibility	7
1.1.4.1 Protein adsorption to the surface of the biomaterial	8
1.1.4.2 Toxicity	9
1.1.4.3 Immune response and foreign body reaction	10
1.1.4.4 Osteointegration	11
1.2 Orthopaedic implant-associated infections and antimicrobial solutions.....	13
1.2.1 Microorganisms	14
1.2.2 Antimicrobial coatings and surface modifications	17
1.2.2.1 Design of antimicrobial surfaces	18
1.2.2.2 Antimicrobial agents; are inorganic compounds the ideal solution	19
1.3 TiO ₂ nanotubes in orthopaedic implants.....	21
1.3.1 Production of TNTs	23
1.3.2 Electrochemical anodization of Ti in F ⁻ containing electrolytes.....	25
1.3.2.1 Phase I: Initial stage of anodization	25
1.3.2.2 Phase II: Chemical dissolution of Ti and TiO ₂ by fluoride ions.....	27
1.3.2.3 Phase III: Self-organization the porous oxide to the nanotube layer	28
1.3.3 Parameters affecting TNTs growth and morphology	30
1.3.3.1 Applied potential and current density.....	32
1.3.3.2 Temperature	33
1.3.3.4 Counter Electrode	34

1.3.3.5 Electrode Distance	35
1.3.3.6 Time	35
1.3.3.7 Ti alloy composition and structure	36
1.3.4 Properties of TiO ₂ nanotubes produced through anodization	37
1.3.4.1 Morphology.....	37
1.3.4.2 Composition	39
1.3.4.3 Phase structure	40
1.3.4.4 Wettability	41
1.4 Bibliography.....	43
2. Research project Layout and Experimental Techniques	49
2.1 Research layout.....	49
2.2 Surface preparation	49
2.3 Microstructural characterization of Ti alloys	51
2.4 Electrochemical anodization.....	53
2.5 Surface analysis and morphology characterization of the produced TNTs.....	54
2.6 Evaluation of corrosion resistance.....	56
2.7 Antimicrobial decoration/functionalization	56
2.7.1 Electrodeposition of Zn and Cu.....	56
2.7.2 Electroless deposition of Ag.....	57
2.8 Antimicrobial tests.....	57
2.8.1 Bacterial strain and media	58
2.8.2 Antimicrobial activity evaluation of TNT-Zn and TNT-Cu	58
2.8.3 Antimicrobial activity evaluation of TNT-Ag.....	59
2.9 Biocompatibility assays	59
2.10 Bibliography.....	60
3. Microstructural characterization of the Ti alloys	61
3.1. Microstructure of Ti grade 2	61
3.2. Microstructure of Ti grade 5	63
3.3 Partial conclusions	65
3.4 Bibliography.....	65

4. Electrochemical anodization of Ti alloys	67
4.1. Electrochemical anodization of Ti grade 2.....	67
4.1.1 Influence of electrolyte aging on TiO ₂ nanotubes morphology	67
4.1.2 Morphology of TNTs grown on Ti grade 2	69
4.2 Electrochemical anodization of Ti grade 5	76
4.2.1 Morphology of TNTs grown on Ti grade 5	76
4.2.2 Growth process of TNTs on Ti grade 5.....	83
4.3 Partial conclusions	87
4.4 Bibliography	88
 5. Heat Treatment and corrosion resistance.....	 91
5.1Effect of anodization and heat-treatment on Ti grade 2 TNTs structure.....	91
5.1.1 Effect of heat treatment on bare samples.....	91
5.1.2 Effect of heat treatment on anodized samples	94
5.1.3 Effect of anodization and het treatment on corrosion resistance	99
5.2 Effect of anodization and heat-treatment on Tii grade 5 TNTs structure	103
5.2.1 Effect of heat treatment on bare samples.....	103
5.2.2 Effect of heat treatment on anodized samples	107
5.2.3 Effect of anodization and heat treatment on corrosion resistance.....	110
5.3 Partial conclusions	114
5.4 Bibliography	115
 6. Antimicrobial functionalization	 117
6.1 Electrodeposition of Zn and Cu.....	117
6.1.1 Antibacterial activity of Zn and Cu-decorated TNTs.....	122
6.2 Electroless deposition of Ag.....	124
6.2.1 Biocompatibility of TNT-Ag.....	126
6.2.2 Antimicrobial activity of TNT-Ag.....	127
6.3 Partial Conclusions.....	129
6.4 Bibliography	130
 7.Final Remarks	 131
7.1 Suggestions for future work	133
7.2 Bibliography	134

ABBREVIATIONS

AFM	Atomic force microscopy
AgNPs	Silver nanoparticles
ALP	Alkaline Phosphatase
AMPs	Antimicrobial Peptides
ATCC	American type culture collection
ASTM	American Society for Testing and Materials
CaP	Calcium phosphate
CFU	Colony formation units
Cp-Ti	Commercially Pure Titanium
CuNPs	Copper nanoparticles
CV	Cyclic voltammetry
DC	Direct current
DI H₂O	Deionized water, classified as type II
DMSO	Dimethyl sulfoxide
ECM	Extracellular Matrix
EDXS	Energy dispersive X-ray spectroscopy
EtOH	Ethylene glycol
EtOH+NH₄F	Ethylene glycol-based electrolyte with an unspecified amount of ammonium fluoride
EtOH+HF	Ethylene glycol-based electrolyte with an unspecified amount of hydrofluoric acid
FBGC	Foreign Body Giant Cell
FESEM	Field emission scanning electron microscopy
HAp	Hydroxyapatite
HT	Heat treatment
I-t curve	Current-time curve
LDH	Lactate dehydrogenase

MHB	Müller Hinton Broth
MG63	Human-derived osteosarcoma cell line
MSC	Mesenchymal stem cell
OCP	Open circuit potential
PBR	Pilling-Bedworth ratio
PBS	Phosphate buffered saline
PDGF	Platelet-derived growth factor
PDP	Potentiodynamic polarization
PMMA	Polymethyl methacrylate
ROS	Reactive oxygen species
RNS	Reactive nitrogen species
SEM	Scanning electron microscopy
<i>S. epidermidis</i>	<i>Staphylococcus epidermidis</i>
SHE	Standard hydrogen electrode
SKPFM	Scanning-Kelvin probe Force Microscopy
THA	Total Hip Arthroplasty
TGF-β	Transforming growth factor β
TNTs	TiO ₂ nanotubes
TNT-Ag	TiO ₂ nanotubes decorated/functionalized with silver
TNT-Ag-low	TiO ₂ nanotubes decorated/functionalized with a low amount of silver (4 wt.%)
TNT-Ag-high	TiO ₂ nanotubes decorated/functionalized with a high amount of silver (8 wt.%)
TNT-Cu	TiO ₂ nanotubes decorated/functionalized with copper
TNT-Zn	TiO ₂ nanotubes decorated/functionalized with zinc
VEGF	Vascular Endothelial Growth Factor
WFE	Working force of the element
XRD	X-ray diffraction
ZnNPs	Zinc nanoparticles

ACKNOWLEDGEMENTS

In the very long list of people to which I owe a very well-deserved thank you, the first very first would be my colleagues at Lima. To Ricardo Toninato, Frederico Asil, Alberto, Luca Pagin, thank you all for the kind introduction into the corporate environment and the reality of the business of orthopaedics. To my co-supervisor, Elisa Salatin, for the availability, the support and the help. Never once I received a “no” for an answer. To Nicoletta Giancesini, Alessia Lizzi, Francesca Giacomini, who welcomed me here and guaranteed all the bureaucracy for this project. A very special thank you for all their support and availability.

Equally important (if not even more), are the people at UNIUD. To Dr. Maria Lekka and Dr. Ruben Offoiach a very heartfelt thank you. It was a wonderful experience working with people with such passion, and with a scientific insight that goes beyond knowledge, that helped me overcome the several obstacles that came along the way. Your guidance, training and suggestions were unvaluable. More than that, you also guaranteed a warm welcome, going the extra mile, and offering help way beyond the issues of work. To my supervisor, Prof. Lorenzo Fedrizzi, for giving me this opportunity, all the help and advice, and the lessons. It was truly a privilege to be thought by you. And last but not least to my dear colleagues at Uniud: Ehsan Rahimi, fellow mCBEEs colleague (and neighbor during this period), for all the help and the tea, the talks and your insight into corrosion. To Jacopo, Denise, Daniela and Cristian for all the kind introductions into the group and the dinners. To Rosanna Pomeraj, for all the bureaucratic help. Similarly, a kind thank you to Prof. Carla de Leittenburg for the guidance with XRD.

At INEB-i3s, a very especial thank you to Dr. Claudia Monteiro, Dr. Cristina Martins, Miguel Morais, Maurizio Gulino, Ana Paula Filipe, Dalila Pedro e Dr. Ana Paula Pêgo. I had an incredibly awesome three-month period, in Porto, Portugal, in spite of Covid-19 related restrictions. They showed an incredible level of support and interest, going the extra mile for me and my project. It was a pleasure to work with you.

Another very special thanks to Gina and Gerard, my roommates, that in my initial period in Udine, really made sure I was properly introduced into city. To Gerard's supervisor, Professor Barbara Skerlavaj, who kindly allowed us to make initial biological tests for initial tests with Ag (and Gerard who was available for doing them) in their department.

To Prof. Ingrid Milošev, Peter Rodič, Ivan Spajić, Dolores, Barbara and all the people at Jožef Stefan Institute in Ljubljana, Slovenia. It was really a pleasure to work with you guys.

To all my other colleagues of mCBEEs: Salil, Chinmay, Maurizio, Don, Live, Iryna, Jiaen, Nourhan, Koushik, Konrad, Sabrina and Mirsajjad. I am going to miss you all.

Last, but not least, to my family, who I love very much, for all the support they gave me... you mean the world to me.

1 THEORETICAL REMARKS

1.1 Titanium and titanium alloys in orthopaedic implants

Orthopaedic implants are devices whose purpose is to replace, or assist, damaged or defective bone structures in the human body. They vary in shape, size, and complexity, being designed to address different challenges in bone regeneration, namely, fracture fixation, joint replacement, or dynamic stabilization of bone structures. Several examples are depicted in Figure 1-1, including reconstructive implants such as joint replacements used in arthroplasty interventions (Fig. 1a-b and 1d-f), fracture management products such as fracture plates, intramedullary devices, bone screws (Fig. 1c), among others.^[1] They constitute the largest segment in the market of medical implants, with a net worth of 55.8 billion USD (US dollars) in 2020, and an expectance of reaching 76 billion USD in 2026.^[2] This is a consequence of the high incidence of musculoskeletal diseases worldwide, which can range from bone fractures to chronic conditions such as rheumatoid arthritis, osteoarthritis or osteoporosis. These are conditions with no known cure, that progress over time and will inevitably result in the need of implants to either help bone healing, or to assist in function.^[3]

Titanium (Ti) alloys were developed in the late-1940s for the aviation industry and were first used in orthopaedics around the same time. Two post-World War II alloys, commercially pure Ti (Cp-Ti) and Ti6Al4V, remain the most used in implants today. Cp-Ti is 98-99.6% of pure titanium and is mostly used in maxilla and cranio-facial implants, wires, screws and staples for spinal surgery. The Ti6Al4V alloy, contains 6% of Al (aluminium) and 4% of V (vanadium), and is used for total arthroplasty components and bone fixation devices such as nails, screws and nuts. Their wide adoption can be attributed to the work of Branemark *et al.* in 1964, which first described the phenomenon of osteointegration, and reported on the ability of Ti-based implants to become tightly integrated with bone, decreasing the risk of loosening and failure.^[1,4]

The materials, as the ones used in orthopaedic implants, that are in contact and interact with biological systems are, by definition, biomaterials. In the discipline of materials science, a biomaterial must be understood as:

“A substance that has been engineered to take a form which, alone or as part of a complex system, is used to direct, by control of interactions with components of living systems, the course of any therapeutic or diagnostic procedures”^[5]

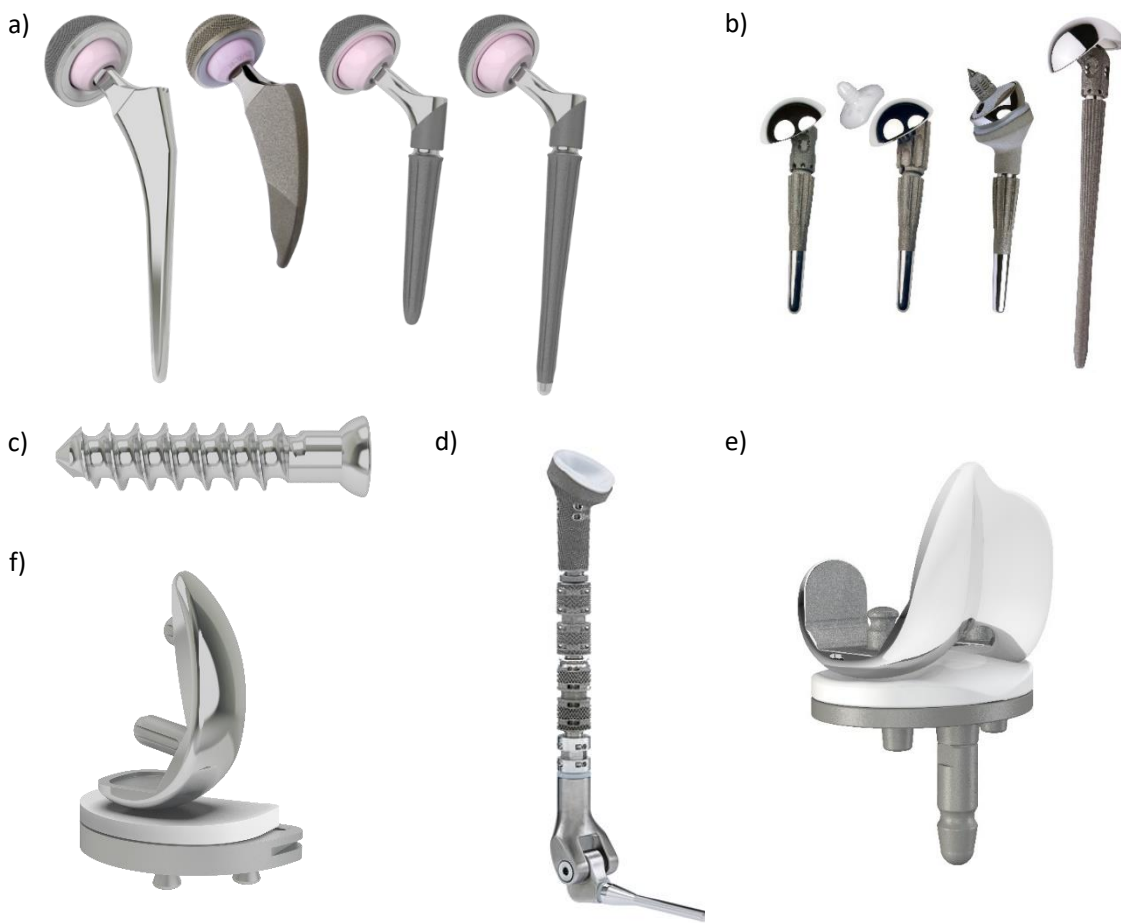


Figure 1-1: Examples of orthopaedic implants: a) total hip arthroplasty systems (THA), b) shoulder arthroplasty systems c) bone screw, d) a complete shoulder-elbow replacement system, e) total knee arthroplasty system and f) unicondylar (partial) knee arthroplasty system. [Courtesy of LIMACorporate, SpA]

Central to a biomaterial is the interaction with the biological environment which, with regard to its performance, could be summarized in terms of biocompatibility (in particular for orthopaedic implants, also its osteointegration), corrosion resistance and mechanical properties. Historically, metal implant materials usually stem from other industrial applications, due to easy manufacturing, processing, availability and well-known properties. Such was the case of Ti alloys, as well as other metals prior introduced, namely, stainless steel alloys (introduced in 1926), and CoCr based alloys, (introduced in the 1930s and developed for aircraft engines). Their long-term adoption, however, depends on them meeting the specific requirements mentioned above, which evolve over time.^[6,7] In the modern total hip arthroplasty implant (Figure 1-1 a and Figure 1-2), metals are employed mostly in the stem, the head and the cup, due to their unique mechanical properties such as high strength, ductility, fracture toughness, hardness and

formability. The stem and the cup have purpose of being integrated within bone, offering fixation and load transfer. The head, on the other hand, will articulate with the liner (which is placed inside the cup), as bearing surfaces of the implant. These components have distinct requirements and as such, the specific properties required of the materials are quite distinct.^[5,7]

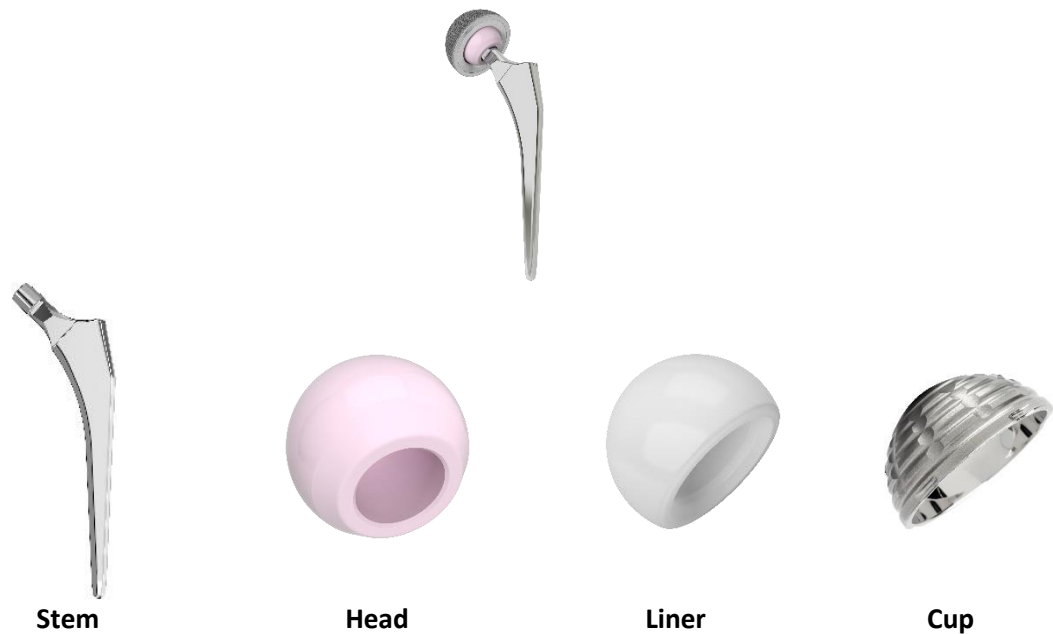


Figure 1-2: Components of a modern total hip replacement system. Based on image from^[5]. [Courtesy of LIMACorporate, SpA]

Stainless steels, the first to be adopted, were extensively used during the 1970s, but reports of failures after 9 to 21 years of service, led to its gradual replacement by, first CoCrMo, due to their corrosion resistance^[6], and then by Ti alloys, due both to their osteointegration capacity and corrosion resistance.^[4] Today, the stem and the cup of most THA are usually made of Ti alloys, with some solutions still existing in Co-Cr alloys and stainless steel. The austenitic 316LV stainless steel, is used mostly in temporary applications such as fracture plates, nails and screws. The head is made mainly of CoCrMo alloys, due to their high hardness. Indeed, the sliding parts of knee (Fig. 1d) and ankle replacement (Fig. 1a) devices are almost exclusively made of CoCrMo. Moreover, ceramic materials such as Al_2O_3 and/or ZrO_2 (so called Delta), can be used as alternatives.^[1,5,7]

The following sections present a brief description of the intrinsic attributes of Ti alloys that influence its performance in orthopaedics. In general, these alloys present outstanding properties that resulted in their preferred selection with regard to other alloys.

1.1.1 Microstructure of Ti

Ti exists in two allotropic forms, a hexagonal closed packed structure (hcp), known as α , at low temperatures, and a body centred cubic structure (bcc), termed β , at high temperatures. The β -transus temperature, below which α phase begins to nucleate in the microstructure of the β -Ti alloy and there is a transition from a pure β microstructure to a $\alpha+\beta$ phase microstructure (with distinct grains presenting an α and β microstructure), is commonly $882\pm 2^\circ\text{C}$. However, the addition of different alloying elements can increase or decrease the β -transus temperature (varying from 700°C to 1050°C). Elements such as Al, O, N, C tend to increase the β -transus temperature and stabilize the α phase at room temperature, being known as α stabilizers. Elements such as V, Mo, Nb, Fe or Cr depress the β -transus temperature, stabilizing the β phase at room temperature and are known as β stabilizers. Other elements, such as Zr, that do not affect the β -transus temperature, are known as neutral stabilizers. Ti alloys containing only of α (or neutral) stabilizers and presenting only α phase stable at room temperature, are known as α alloys. Alloys containing higher amounts of β stabilizers and about 10 to 30% of β phase stable at room temperature, are categorized as $\alpha+\beta$ alloys. Alloys with only β phase stable at room temperature and no α phase formed, are known as β alloys.^[8,9]

Ti alloys possess a wide spectrum of microstructures, defined by the size and arrangement of the two phases, that can be tailored through changes in the chemical composition or by thermal processing (stress relieving, annealing, ageing, etc). Alloys processed/treated above the β -transus temperature, present an acicular or lamellar structure. On the other hand, the alloys treated or processed below the β -transus temperature, in the $\alpha+\beta$ temperature range, present a mixture of equiaxed α and β grains. The American Society for Testing and Materials (ASTM) classifies the wide variety of Ti alloys in 39 distinct grades in several forms (seamless pipes, bars, strip, welded pipe, wire, among others), based on their chemical composition and thermomechanical treatment history. In orthopaedic implants, the grade 2 (Cp-Ti, pure α -alloy) and grade 5 (Ti-6Al-4V, $\alpha+\beta$ microstructure in annealed condition) alloys are the most widely used. Generally, the increase in β stabilizer content increases the strength. The $\alpha+\beta$ alloy has a higher strength and lower cycle fatigue than the α alloy, but it is less ductile.^[9,10]

1.1.2 Corrosion resistance

Corrosion of metallic implant leads to metal degradation, which can decrease the structural integrity, and degradation products (i.e., metal cations, debris), which may elicit an adverse reaction from the host (see 1.1.3.2).^[7,9,11,12] Ti alloys, medical stainless steel 316 L (316SS) and Co-Cr alloys are passive metals, owing their corrosion resistance to a stable oxide layer on their surface. 316LSS and Co-Cr are protected by a chromium oxide layer, Cr_2O_3 , while Ti alloys are protected by a titanium oxide (titania) layer, TiO_2 . Disruption of this oxide can result of local changes of pH, low oxygen concentration, reactive oxygen species (ROS), fretting or wear, among others. If disruption occurs, corrosion continues until eventual re-passivation, which will depend on the nature of the medium and of the metal itself. Thus, the corrosion resistance of a metal is determined by the ability of the oxide to not disrupt or to repassivate/regenerate in an environment.^[10,13]

Human body fluids are highly corrosive and can be generally described as a buffered NaCl solution (about 0.9% wt.) with a pH of 7.4, a temperature of 37°C and a quarter of the oxygen partial pressure of the atmosphere. It contains several anions such as PO_4^{3-} or carboxil $-\text{CO}_2\text{HO}$ and cations such as Ca^{2+} , Mg^{2+} or K^+ , among others. ^[14,15] Specific chemical and biological interactions can lead to corrosion in unique ways.^[5] For instance, enzymes such as peroxidases, can accelerate oxygen reduction and thus, the cathodic reaction.^[14] Disulphide compounds and several biomolecules can replace the typical role of O_2 .^[16] Carbohydrate components of the extracellular matrix possess anionic groups (carboxyl, phosphate, or sulphate, etc.) that bind to metal ions and transport them away from the implant surface.^[14] Moreover, this environment is prone to localized variations of pH and fluctuation in ionic strength. For instance, the implantation surgery leads to a local decrease of the pH to 3-4. Ion deposits can increase locally the ionic strength. Furthermore, the geometry of the implant can also induce specific corrosion processes. Crevice inducing geometries such as modular taper junctions or beneath the head of fixing screws, prevent diffusion of oxygen from the exterior, leading to its depletion in the inner area of the crevice, resulting in crevice corrosion.^[5]

Table 1-1 lists the rest and breakdown potential for common biomedical metals, after 480 hours of immersion in a deaerated 0.17 M NaCl solution. For Co-Cr alloys, the rest potential (0.5 V) is below the breakdown potential (0.87 V) and, thus, film breakdown is unlikely, although possible in controlled conditions. For Ti alloys, the difference between potentials is so great that breakdown is almost impossible (0.37 V vs 9 V for Cp-Ti, 0.23 V vs 25 V for Ti6Al4V). Thus, they should exhibit a truly passive

behaviour in simulated physiological solutions, such as Hanks or Ringer's. For stainless steels, however, the resting and breakdown potential are quite similar, being unlikely to resist corrosion in the human body. ^[9,11,17]

Table 1-1 – Resting and breakdown potentials of major Implant Metals and alloys. ^[17]

Material	Resting potential (V) after 480 h in deaerated 0.17 M NaCl	Breakdown potential (V) in deaerated 0.17 M NaCl
316 Stainless steel	0.3-0.5	0.4-0.48
Cast Co-Cr alloy	0.5	0.87
Cp-Ti (ASTM grade 2)	0.37	9
Ti6Al4V (ASTM grade 5)	0.23	25

1.1.3 Mechanical Properties

A biomaterial in an orthopaedic implant must exhibit similar mechanical properties to that of the bone. Bone is a light structure, strong and tough enough to sustain pressurized loads without irreversibly deforming or breaking. For the femur, during a step, most of the body weight pivots on only one leg at a time, with an estimated loading stress of five times that value. An orthopaedic implant, thus, must be light, to facilitate motion, but stiff enough to sustain the applied loads without permanent deformation or fracture. This is defined by the Yield Strength and Ultimate Strength of the material. Yield strength represents the maximum value of stress (tensile or compressive) that can be applied without permanent deformation. Ultimate Strength is the maximum amount of stress that can be applied before breaking (after permanent deformation occurs). The ideal material has an appropriately high yield strength with adequate ductility.^[5,7] Moreover, the femur carries the external loads from the hip joint and the muscle into adjacent bone. In hip replacement implants, it shares this load-carrying capacity with the stem.^[11] Huiskes *et al.* showed that, when there is a reduction in the tensile/compressive load to which the bone is exposed, decreased bone thickness, mass loss, and increased osteoporosis occur, which can lead to loosening of the implant.^[18] The capacity of the material to distribute the stress to adjacent bone is related with the Young modulus. This parameter represents the ability of the material to sustain loads under elastic deformation, i.e., to reversibly shorten and widen when compressed, or lengthen and narrow under tensile loads, without cracking. Ideally, the Young modulus should be close to that of bone.^[12,18] Table 1-2 lists the described mechanical properties for common biomedical metals. The Young Modulus of Ti6Al4V

and Cp-Ti is half of the modulus of both 316LSS and Co-Cr alloys (110 GPa and 105 GPa against 200 GPa and 230 GPa, respectively). Moreover, Ti alloys present the same strength as 316LSS while having 55% less density. As such, they represent the best set of these mechanical parameters for bone implants. Nevertheless, a modulus of around 100 GPa is still much higher than bone (~4-30 GPa), so these alloys do not completely prevent stress-shielding.^[5,7,8,11,19]

Table 1-2 – Mechanical properties of the most common biomedical metal alloys.^[19]

Alloy	Young Modulus (Gpa)	Yield Strength (Mpa)	Ultimate Tensile Strength (Mpa)
316LSS	200	170-750	465-950
CO-CR-MO	200-230	275-1585	600-1795
CP-TI	105	692	785
TI-6AL-4V	110	850-900	960-970

1.1.4 Biocompatibility

Biocompatibility is characterized by both the local or systemic response of the human body to the material, and the response of the material to the human body environment (i.e., the degree of degradation induced which depends not only on mechanical and corrosion properties, but also on cellular response). An implanted material can lead to tissue death if it is toxic, fibrous tissue formation if it is non-toxic but is biologically inactive, osteointegration if it is bioactive or be reabsorbed by the tissue. Depending on the triggered host reaction, it is classified, respectively, as non-biocompatible, biotolerant, bioinert, bioactive or bioabsorbable. This classification scheme is listed in more detail in table 1-3. It is important to note that bioresorbable, bioactive, bioinert and biotolerant materials are biocompatible.^[20] Generally, Ti alloys are classified as bioinert, not having any allergenic or immunogenic effects *in vivo*, while presenting contact osteointegration. In comparison, both CoCr alloys and Stainless steel are classified as biotolerant materials, with distance osteointegration, with the potential risk of loosening or allergies. On one hand, this could be attributed to the overall mechanical and corrosion properties of Ti alloys.^[12,20] On the other hand, the excellent properties of the native TiO₂ cannot be disregarded. This thin layer (4-6 nm thick), spontaneously formed upon contact of Ti metal with oxygen, is generally considered a chemically stable and inert material, which is also biocompatible. However, a host response to an implant can be variable and is under genetic regulation. Some hosts can

trigger a foreign body reaction to a material or be genetically predisposed to have allergies against it, while others can develop only sensitivity to these materials over time.^[19–22]

Table 1-3 - Classification of biomaterials according to the triggered host response.^[8,13,20]

Classification	Response	Examples	Effects
Biotolerant materials	Distance osteogenesis and formation of thin connective tissue capsules (0.1-10 μm). The capsule does not adhere to the implant surface.	Gold, 316LSS, Co-Cr, Polymethyl methacrylate (PMMA), etc.	Potential rejection, although not necessary, of the implant leading to failure.
Bioinert materials	Contact osteogenesis without the formation of a fibrous layer.	Ta, Cp-Ti and Ti alloys, Al oxide and Zr oxide	Implant is accepted. Suffers low degradation, with possible release of wear debris which can affect its long-term stability.
Bioactive materials	Elicit a response from the surrounding bone tissue. New bone is formed over their surface and ion exchange with the tissue lead to the formation of chemical and biologic bonding along the interface.	Bioglass, synthetic calcium phosphate inducing hydroxyl apatite (HAP)	Formation of bone tissue around the implant material with a strong integration with the material surface
Bioreabsorbable materials	Elicit a positive response from the bone tissue leading to the formation of new bone at the surface. The material is resorbed and completely replaced by the autologous tissue.	Polylactic acid, polyglycolic polymers, and processed bone grafts, composites of all tissue extracts or proteins and structural support system.	Acceptance of the implant leading to success of implantation, and almost complete bone healing with material disappearance.

1.1.4.1 Protein adsorption to the surface of the biomaterial

Seconds to minutes following implantation, the contact of the implant with blood or plasma, released due to injury from the surgical procedure, results in the adsorption of a protein layer on the surface of the device. Blood and plasma are complex mixtures that contain, besides blood cells, proteins, lipids, sugars and ions which adsorb to the surface of the material. The overall protein adsorption process is governed by a phenomenon known as Vroman effect, in which several factors such as the pH of the environment, the local relative concentration of available proteins as well as the chemistry, potential, topography or roughness of the surface of the biomaterial will determine the composition of the adsorbed protein layer.^[23] Moreover, the adsorbed proteins undergo conformational changes or even denaturation on the surface, which is related with their degree of structural stability and surface properties.^[12] Depending on the conformation

change, the protein can trigger a specific biological response. Adsorbed proteins typically include albumin, fibrinogen, fibronectin, vitronectin, immune globulins and several coagulation and complement factors. This layer of proteins will mediate the host reaction to the biomaterial, since cells primarily see the adsorbed protein layer, instead of the actual surface of the material. Fibrinogen and coagulation and complement factors are associated with the activation of the inflammatory response. Fibronectin and vitronectin, instead, enhance bone cell adhesion and modulate the inflammatory response.^[24,25] In general, water is readily absorbed by TiO_2 , resulting in the formation of TiOH groups, thus having high affinity for protein adsorption. A stable protein layer is formed in less than 3 hours, *in vivo*. Fibrinogen adsorbs greatly to both Cr_2O_3 and TiO_2 . However, Co-based alloys induce higher conformational change due to higher electron conducting properties of the surface oxide.^[26]

1.1.4.2 Toxicity

Toxicity refers to the ability of a material to provoke cell or tissue death (citotoxicity), cancer (carcinogenicity), genetic damage (mutagenicity), immune rejection (pyrogenicity and allergenicity) or blood clotting (thrombogenicity).^[13] The release of biomaterial components, due to corrosion or mechanical damage, into the human body environment, can trigger a biological effect at a tissue or systemic level, in the proximity of the implant or in other body locations. Elements like Ni, Mo, Co and Cr are found to be released from Co-Cr and 316LSS implants.^[8] Ni and Co are harmful to cultured bone cells and implanted pure nickel leads to severe local tissue reaction and necrosis. Ni^{2+} ions can cross the cell membrane, either by active uptake or endocytosis of nickel compounds, leading to DNA damage. High exposure levels of Co is associated with dermatitis, painful muscle fatigue, cramping dyspnoea, decline in cognitive function, memory difficulties, severe headaches and potential carcinogenicity. Chromates (Cr) also provoke severe dermatitis or skin ulcers, upon contact, with potential to be mutagenic or carcinogenic. Mo is less toxic than Co or Cr, but high exposure could lead to irritation of eyes and skin.^[5,7] Regarding Ti and its alloys, Ti is not present in the human body and does not have any known toxic effects. A daily intake of 0.8 mg of Ti by humans was found to be completely excreted without being digested or absorbed.^[8] However, in the case of Ti grade 5, both V and Al are released into the body. V toxicity is related with the oxide form, with potential carcinogenicity. Al has been linked to osteopenia in infants, brain neurotoxicity, dermatitis, and digestive disorders in people with kidney disease, as well as increased gene expression in human breast cancer cells. Thus, the concern exists that excessive exposure, can lead to breast cancer or neurological conditions such as

Alzheimer's disease. Nevertheless, there is lack of reports of adverse effects of V when in the Ti6Al4V alloy, although some reports of allergies have been registered.^[1,5,8]

1.1.4.3 Immune response and foreign body reaction

The implantation of orthopaedic devices triggers an immune response, which results in either bone regeneration around the implant, or fibrous encapsulation, i.e, the body forms a “wall” around it, isolating it. The outcome depends on several factors, including specific surface properties, release of degradation products, degree of implantation damage, insufficient mechanical compliance or poor *in situ* stabilization of the device. Initial protein adsorption (see 1.1.3.1) plays a determinant role.^[22,24]

By order of events and gravity, the immune response may comprise an acute inflammation stage, chronic inflammation stage, granulation tissue formation, foreign body reaction and fibrous encapsulation (fibrosis). The initial acute inflammation stage is characterized by local accumulation of neutrophils and monocytes, which secrete ROS and nitrogen reactive species to degrade and consume the implant, in a mechanism of “frustrated phagocytosis”. This could seriously damage neighbouring tissues, and cause material degradation. They also secrete chemoattractants to further promote the migration of other immune cells into the area. Neutrophils quickly disappear, but monocytes differentiate first to M1 macrophages (by adhered fibrinogen), which promote inflammation, or later into M2 macrophage, which promotes tissue reconstruction. The specific phenotype results of stimuli released by damaged tissue cells or other immune cells. Continuous “opsonization”, or micromotion of the implant, leads to the chronic stage, marked by foreign-body giant cells (FBGC -formed through the fusion of macrophages in order to increase their phagocytic capacity). FBGC may stay adhered to the biomaterial for years. Simultaneously, the granulation tissue forms, containing fibroblasts, vascular endothelial cells and presenting small blood vessels. Together, with FBGCs they define the foreign body reaction. The final stage is fibrotic encapsulation or fibrosis, in which growth factors synthesized by M2 macrophages and FBGCs, stimulate fibroblasts to produce collagen, resulting in a “fibrous capsule” around the implant, that isolates it and prevents further interplay with host tissues.^[22,27,28]

Figure 1-3 illustrates the possible outcomes of the immune response to a Ti implant. For metals, the biggest risk is ion release due to both reactive oxygen species (ROS) or reactive nitrogen species (RNS).^[29] Implanted Cp-Ti greatly activates the complement system, but also inhibits the inflammatory response. TiO₂ reacts with both H₂O₂ and peroxinitirite, forming the Ti-peroxide gel, which inhibits the further action of other reactive species, thus inhibiting phagocytosis.^[30] The transition from M1 to M2

macrophage phenotype, and the disappearance of neutrophils, will determine the outcome of the immune response. A prolonged M1 polarization, and neutrophil presence, signals a chronic inflammation, favouring the formation of the fibrous tissue. Generally, high surface to volume implants (porous implants) have higher ratios of macrophages and FBGC than smooth surfaces.^[27,31]

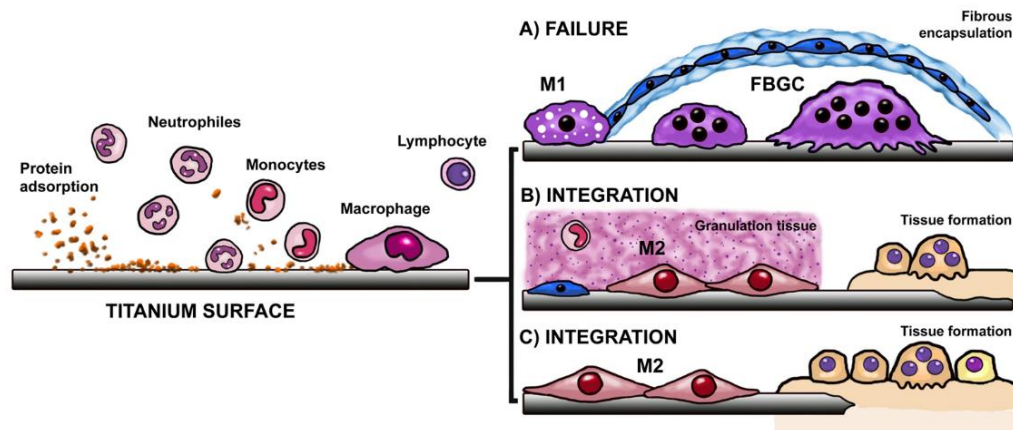


Figure 1-3: Hosts response to biomaterials. A) implant failure due to fibrous encapsulation. B) Integration with formation of a granulation tissue. C) Perfect osteointegration.^[28]

1.1.4.4 Osteointegration

Osseointegration is the establishment of a mechanically solid interface between biomaterial and bone. The implant becomes fused with bone to a point where separation is not possible without fracture, and there is no relative movement between them.^[8] Peri-implant osteogenesis can occur in contact or at a distance from the implant. In distance osteogenesis, peri-implant bone trabeculae forms from the host bone towards the implant surface. The existent bone tissues provide a population of osteogenic cells that lay down the new bone matrix, which, as osteogenesis continues, encroaches on the implant itself. In contact osteogenesis, peri-implant bone develops from the implant surface towards the healing bone. Previously, the implant surface has been colonized by a population of osteogenic cells. Generally, the process of bone healing around an implant comprises three different phases: osteoconduction, *De novo* bone formation and bone remodelling. During osteoconduction, non-differentiated osteogenic cells migrate to the implant surface. If the cells differentiate before reaching the surface of the implant, they will synthesize bone matrix that will not be in contact with the implant surface, if not, a mineralized matrix will be synthesized on the implant (contact osteogenesis), during the *De novo* Bone formation phase.^[32]

The ability of bone cells to attach to the implant surface, involve specific interactions with adsorbed proteins (see section 1.1.3.1), the extracellular matrix and

cytoskeleton proteins, including, collagen type I and V, osteocalcin, serum albumin, fibronectin or vitronectin. This interaction occurs through cadherins and integrins and is translated into internal signals that induce cell spreading or migration, as well as cell growth and differentiation.^[33]

Bone healing is highly modulated by the immune system (see section 1.1.4.3). The provisional matrix acts as a scaffold for migration of bone cells towards the implant surface. Neutrophils and leukocytes clear the wound area of damaged bone tissue, together with osteoclasts (bone resorbing cells), so that deposition of “new” bone can occur. Platelets and immune cells release chemoattractants such as transforming growth factor beta (TGF- β), vascular endothelial growth factor (VEGF) or platelet-derived growth factor (PDGF), that influence bone cell migration.^[21,26,27,31] In addition, as previously described, the continuum of distribution between M1 and M2 macrophage phenotype will decide between fibrous encapsulation or osteointegration. The M1 macrophage type, known as pro-inflammatory, secrete oncostatin M, a cytokine that induces the osteogenic differentiation of bone cells. M2 macrophages, also known as anti-inflammatory or pro-healing macrophages, secrete osteogenic/angiogenic molecules. They also serve as precursors of osteoclasts the cells responsible for bone resorption (active in bone remodelling processes). Local depletion of macrophages has been shown to lead to absence of bone formation, in *in vivo* studies.^[34,35]

1.2 Orthopaedic implant-associated infections and antimicrobial solutions

Orthopaedic implant-associated infections represent a high burden for the patient and healthcare providers. A recent screening in Italy, between 2012 and 2014, reported prevalence of cases of about 1.55% of all interventions, which resulted in a total of 72,091 days of extended hospitalization and a total cost over 93 million euros. The increased cost is associated with prolonged hospital stay and the need of additional treatment (see Figure 1-5). It is estimated that the costs will increase about 3 to 4-fold when compared to a single, successful implantation case. In the U.S., the economic burden of implant-related infections is estimated to have reached \$1.62 billion in 2020. Figure 1-5 presents a comparison of the increased hospital costs related with infection of prosthetic devices.^[36,37]

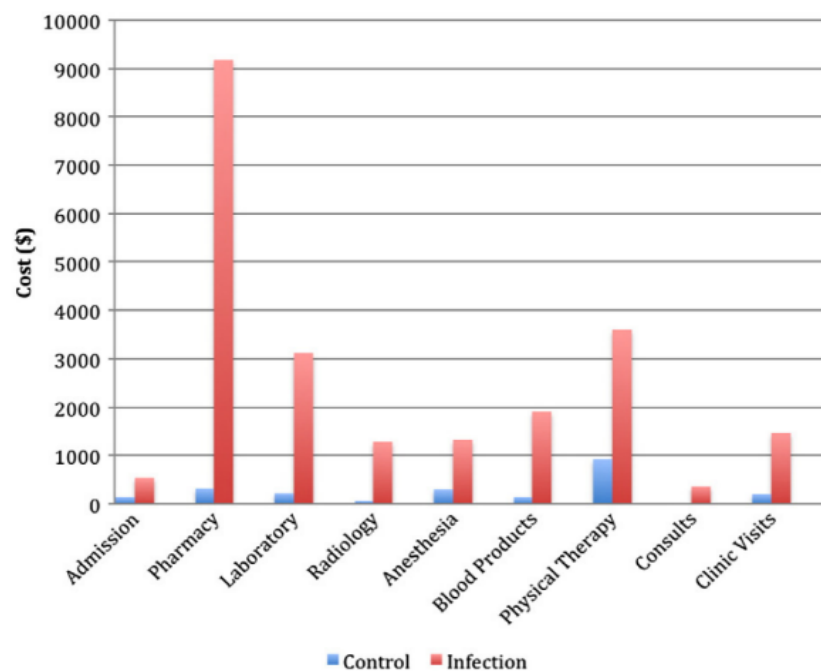


Figure 1-5 – Comparison of costs per service, in a hospital, between primary knee arthroplasty (blue) and in the secondary knee arthroplasty (red) due to infection.^[38]

Infection results of the synergy of various factors, namely, sterility of the operating theatre, surgical technique, and procedure duration (related with the patient's weight or implant size). The skin of the patient or surgeon is the main external source of infection, while airborne microorganisms (aerosol contamination) is a less common cause, although possible. Lastly, contiguous spread from an adjacent infected tissue or distant foci in the body is also a possibility. In this case, the clinical history of the patient, for instance an antecedent bacteraemia or fungemia (high risk in a period of 1 year

precedent to procedure) is the main factor. It can occur in the early postoperative period, due to an incomplete healing, or later, if the tissue is disrupted by trauma or surgery.^[39] Risk factors include rheumatoid arthritis (due to the use of corticosteroids immunosuppressants for inflammation and pain), diabetes mellitus, chronic kidney disease, malignancy or related medications that can lead to a global immunosuppression, i.e. a debilitation of the immune system which facilitates the colonization and growth of infectious microbiota. Moreover, after the implantation surgery, the local defence system at the implant/tissue interface is compromised due to the absence of local blood flow. Even after osteointegration, the number of blood vessels is relatively small.^[8] Post-operative complications, such as wound drainage or dehiscence are also associated with an increased infection risk.^[39]

1.2.1 Microorganisms

The most common microorganism in orthopaedic implant related infections are bacteria. Gram-positive bacteria represent 45 to 60% of the cases, while gram-negative bacilli represent 9% of the cases and anaerobic bacteria, in general, represent only 4%. A complete view of the relative prevalence of various organisms can be found in Table 1-4. The *Staphylococci* genus are the most frequent, mainly *Staphylococcus aureus* (*S. aureus*) in the US, *S. epidermidis* in Europe, followed by coagulase-negative *staphylococci*. Up to 15% of the cases are polymicrobial infections, which are more usual in early-onset cases (diagnosed up to 3 months after implantation), being associated with *Enterococcus* species, *S. aureus*, aerobic Gram-negative bacilli, specially *P.aeruginosa*, and anaerobic bacteria.^[40,41] Some fungus, mainly the genus *Candida*, have also been identified in less than 1% of the cases. Fungal organisms and atypical bacterial infections (anaerobic bacteria or mycobacteria) occur in patients with history of immunosuppression or autoimmune diseases, diabetes, malignant diseases, or that are submitted to long-lasting antibiotic treatments. In these cases, a specialized treatment is required since the typically applied two-stage revision is not as successfully as in common bacterial infections. The administration of antifungal agents, such as azoles or amphotericin, is recommended for a minimum of 6 weeks.^[39]

Infections can be planktonic, if microorganisms exist in suspension in the joint fluid, or biofilm-forming, if the cells are attached in communities to the implant surface. Usually, planktonic infections are easily cleared, but are less common, while biofilm are more typical, but much harder to clear.^[42] Biofilms are microbial sessile communities composed by cells irreversibly attached to a substratum, interface or to each other, embedded in an

Table 1-4- Most common microorganisms associated with prosthetic joint infections.^[39,40,42]

Class	Specie/Strain	Description	% cases
Gram-positive	<i>S. aureus</i>	The most common. Associated with general nosocomial infections, diabetes mellitus or rheumatoid arthritis.	27
	<i>Coagulase-negative staphylococcus species</i>	Members of the human microbiome of the skin. Are frequent both in early, delayed and late-onset cases.	27
	<i>S. Epidermidis</i>	It has a high ability to adhere to the implant surface and produce biofilms.	27
	<i>Streptococcus species</i>	A group of microbial species associated with malignancy. The infection is presumed to be hematogenous.	<10
	<i>Enterococcus species</i>	More common on early-onset infections, as part of polymicrobial infections, but may also be derived in single cases from hematogenous infection from the gastrointestinal or urinary tract.	3
Aerobic Gram-negative bacilli	<i>Escherichia Coli</i>	The most common of the group, representing 45% of these cases is <i>E. Coli</i> , followed by <i>P. aeruginosa</i> and <i>Non-E. coli Enterobacteriaceae</i> .	9
	<i>Pseudomonas aeruginosa</i>		
	<i>Non-E. coli enterobacteriaceae</i>		
Other anaerobic bacteria	<i>Propionobacterium acne</i>	<i>P. acne</i> is normally found on the skin and sebaceous glands, typically inoculated at the time of surgery. Very rare.	4
	<i>Chlostridium species</i>	Associated with gastrointestinal disease.	4
	<i>Bacteroides fragilis</i>	Associated with colonic diverticulosis	
Fungi	<i>Candida Spp.</i>	Candida represent 80% of fungal infections, but other filamentous fungus have been identified. Its more usual after revision surgery. Diabetes, prior bacterial infection and antimicrobial agents use are risk factors.	<1

extracellular matrix composed by polysaccharides, proteins and/or extracellular DNA.^[41]

The biofilm population can be monomicrobial, if they are formed by the same microorganism, or polymicrobial if formed by different microbial species or strains. However, even the monomicrobial biofilms may consist of subpopulations with different phenotypic and genotypic characteristics. This is one of reasons why biofilms are highly resistant to the immune system and antimicrobial agents, such as antibiotics. Resistant subpopulations (which can share resistance genes to non-resistant cells in the community), persister cells (which replicate at a lower growth rate and can reconstitute

the biofilm when treatment is stopped) or the microenvironment (which can hinder the action of the antimicrobial agent) all contribute to high virulence of biofilms.^[41,43]

Microorganism adhesion to biomaterials surface occurs in two stages. In a first, unspecific and reversible stage, the process is governed by physical forces, also known as “long range” forces, which depend mostly on the distance and free energy, and then by short range forces, such as Van der Waals or electrostatic (ionic, bipolar and hydrophobic) interactions. Thus, at this stage, the local microorganism concentration and specific biomaterial properties will govern the adhesion.^[39] A second, specific and irreversible stage, is governed by molecular interactions between microbial cells and the surface of the biomaterial or the protein layer adsorbed to it. Bacteria possess on their surface polysaccharides known as adhesins which are able to interact with the material surface or proteins such as fibrinogen, fibronectin, vitronectin or collagen (see 1.1.4.1 and 1.1.4.4) or even pre-adhered host cells. Moreover, some bacteria present filamentous cell appendages, known as nanofibers, bacterial pili and pilus-like structures, which also function as adhesins.^[39,41] The current model of bacterial colonization of biomaterial surfaces was first proposed by Anthony Gristina, in 1987, a work that described microbial colonization of an implanted device as a “race to the surface”, a competition between tissue integration and microbial adhesion which ultimately could lead to implant failure. This model is based on the idea that both bone cell or bacteria cell adhesion to the surface is achieved through interactions with either the surface itself or the layer of macromolecules that covers it.^[43] In vitro studies have indeed demonstrated that, on surfaces pre-colonized with bacteria, bone cell adhesion is drastically decreased. These interactions occur with degrees of sensitivity and selectivity for either type of cell, and depend on surface characteristics, environment factors and the adsorbed protein layer.^[40] Between 316SS, Co-Cr alloys and Ti and Ti alloys, the latter are the less prone to colonization by microorganisms. This has been attributed to the higher surface energy of the first two alloys, which promotes bacterial adhesion. Moreover, surface geometry as well as disruption of the surface due to wear or corrosion processes and the consequent release of metal ions and toxins will establish specific environmental conditions which may favour the adhesion and proliferation of specific cell types. In the case of stainless steel alloys, local accumulation of Fe^{2+} or Fe^{3+} , due to corrosion processes, could create an ideal spot for bacterial colonization, since this cation is a virulence factor associated with some pathogenic microorganisms such as *S. Epidermidis*.^[36,40] Maybe for this reason, metal-on-metal joint prostheses are more frequently infected than metal-to-polymer ones.^[44] Nevertheless, the initially adsorbed protein layer can make the surface prone to bacterial colonization and cases of infection of Ti implants have been reported.^[36,44]

1.2.2 Antimicrobial coatings and surface modifications

Antimicrobial coatings or surface modifications have risen as an alternative to systemic antibiotic prophylaxis treatments. Local antimicrobial action can avoid several issues of systemic prophylaxis, namely, low drug concentration reaching the target site, toxicity (since the drugs reach healthy tissues in high quantities before the target location), and emergence of antibiotic resistant microorganisms (such as *meticilin resitant S. Aureus* or *Candida auris*). Considering the strategy of action, they are classified as: ^[45–47]

- **Passive:** either killing by contact or hindering or repelling the adhesion of microorganisms into the surface of the implant. Is based on the modification of the physical and chemical surface properties (hydrophilicity and crystal structure), without the release of antimicrobial agents.
- **Active:** act by leaching pre-incorporated antimicrobial agents, over time, into the vicinity of the implant killing both planktonic and adhered microbial cells.
- **Peri-operative:** biodegradable or not-biodegradable antibacterial carrier or coating that is applied during surgery on the implant or around it. Acts by delivering high local concentrations of one or more pre-loaded antibacterial agents or it may have a direct or synergistic antibacterial activity.

Table 1-5 summarizes some ideal requirements for implant coatings. ^[45–47]

Table 1-5 –Requirements for the ideal antibacterial implant coating strategy. ^[46]

Requirements	Fulfilments			
Safety	No systemic toxicity	No local toxicity	No detrimental effects on bone healing	No unwanted long-term side effects
In vitro activity	No cytotoxicity or genotoxicity	Proven biocidal and antibiofilm activity on different surfaces	Large spectrum	No induction of resistance
Efficacy	Proven in vivo	Case series	Multicenter trials	Randomized trials
Ease of Use	Easy handling	Versatility	Resistance to press-fit insertion	Storage
Market	Acceptable cost	Large availability	Easy to manufacture	Overcomes regulatory issues

1.2.2.1 Design of antimicrobial surfaces

Based on the strategy of action, three distinct mechanisms are on the base of the design of antimicrobial surfaces: antimicrobial agent release (*active* or *peri-implant*), contact killing or anti-adhesion/microorganism repellent (both *passive*). Release-based designs preform local delivery of antimicrobial agents, through a controlled leaching process, over time, in the vicinity of the implant. This could be achieved through a direct diffusion processes, erosion/degradation of reservoirs or even hydrolysis of covalent bonds (in this case, the agent is a molecule covalently bond to the surface). Central to it is the drug delivery system, the structural component that acts as a reservoir and/or as controlled release system for the drug. It normally consists of a porous structure, impregnated with the desired antimicrobial compound (either the bulk material or an overlying surface structure obtained through surface modification or coating deposition). Common carriers include polymers such as poly(methacrylic acid), collagen or Poly-DL-Lactic Acid (PDLLA) as well as hydrogels or ceramics. Alternatively, the agents could be covalently grafted to the surface of the material and released through hydrolyzation of covalent bonds *in situ*.^[45,46,48]

On the other hand, contact-killing and anti-adhesion surface designs include polymer coatings such as hydrophilic poly(nethacrylic acid) or protein-resistance poly(ethylene glycol), which can prevent the adhesion of both *S. aureus* or *S. epidermidis*, or covalent grafting of bio or synthetic molecules that can either repel and prevent the adhesion of microorganisms or kill them by contact, such as chitosan or hyaluronic acid. In this case, killing is achieved through disruption of cell membrane, through lysis or charge disruption mechanisms. Alternatively, properties such as hydrophobicity, surface energy and conductivity or surface chemistry, that influence the amount and conformation of adsorbed proteins, could be targeted. However, determining the degree to which these parameters should be adjusted, while allowing good osteointegration is rather complex.^[41,48] A cheap but highly effective solution for Ti-based metals is UV irradiation, which leads to an increase in surface wettability of the naturally occurring TiO₂, and inhibits bacterial adhesion while enhancing is osteoconductive capacity. Other possibility is annealing treatments performed to obtain a crystalline anatase-type oxide which can reduce bacterial adhesion while promoting bone cell adhesion.^[46,48]

1.2.2.2 Antimicrobial agents: are inorganic compounds the ideal solution?

Various organic and inorganic compounds have been researched as antimicrobial agents for Ti implants. Organic compounds include antibiotics, some biomolecules and antimicrobial peptides (AMPs). Antibiotics are the most extensively researched and adopted due to their extensive use in clinical settings (thus having a well-known effective dose and toxicity). However, they face major drawbacks. The first is their narrow spectrum of activity, being active normally against a specific class of microorganisms.^[49,50] For instance aminoglycosides, such as gentamicin or tobramycin, target mainly gram-negative bacilli (although they can possess some synergistic activity against some gram-positive bacteria of the *Staphylococcus* and *Enterococcus* genus). Glycopeptides such as vancomycin, on the other hand, only target gram-positive bacteria. This poses a severe limitation in case of polymicrobial infections or biofilms.^[50] As an alternative to antibiotics, AMPs have some advantages. These are oligopeptides with fewer than 100 amino acids comprising lytic enzymes, pore-forming molecules (that target microorganism cell-wall) or substances that sequester essential nutrients. Their major advantage is their effectiveness against antibiotic resistant microorganisms, as well as a wider spectrum of action than antibiotics.^[51] Nevertheless, they have seen a very limited adoption since they can undergo proteolytic degradation *in vivo*, or suffer from potential denaturation under certain temperatures and pH conditions.^[52,53]

Inorganic compounds, on the other hand, generally possess a wide-spectrum action (effective against bacteria in general and fungi) as well as high effectiveness against antibiotic-resistant microorganism.^[45,47,49] Moreover, they present higher resistance to temperature and humidity variations, being more stable and durable than organic compounds.^[54] This class of antimicrobial agents comprises ceramic and metallic-based materials as well as their ionic forms or salts, owing their antimicrobial activity to their ionic or nano form, rather than the bulk material.^[30] The more highly regarded inorganic compounds are silver (Ag), copper (Cu) and zinc (Zn).^[45,49,54] Silver is the most prevalently used in biomedical applications. Ag^+ are biochemically active agents that interfere with bacterial cell membrane permeability and cellular metabolism. Moreover, these cations can also contribute to the formation of reactive oxygen species. Nevertheless they can also potentially affect eukaryotic cells, raising concerns regarding its toxicity. However, sensitivity is different among different cells. A concentration between 1.8% to 6.5 wt% has been found to inhibit bacteria proliferation without decreasing osteoblast activity.^[48,50,55,56]

Zinc (Zn) and Copper (Cu), also possess a broad spectrum antimicrobial action and effectiveness against antibiotic resistant microorganisms. Nevertheless, their antimicrobial action is not as strong as silver's, with Cu being the closest and Zn the less. On the other hand, both Zn and Cu possess better biocompatibility. Copper has a role in bone metabolism with its deficiency being linked to skeletal abnormalities and reported to inhibit osteoclast activity. Zinc is an essential trace element, being present in several tissues of the human body, which possesses efficient mechanisms, both on systemic and cellular levels, to maintain homeostasis over a broad exposure range. Moreover, it is a component of hydroxyapatite and has been shown to induce osteogenesis, by inducing bone deposition by osteoblasts, osteogenic differentiation of mesenchymal stem cells (MSC) cells and suppression of osteoclast differentiation (and thus bone resorption). Additionally, it has an immunomodulatory action, being able to neutralize macrophages, as well as stimulate monocytes to secrete pro-inflammatory cytokines. [54,57–59]

1.3 TiO₂ nanotubes in orthopaedic implants

The incorporation of nano topographic features on the surface of Ti alloys has been explored as way to increase their bioactivity (see Table 1-4 and section 1.1.4.4).^[60] Bone can be described as a nanostructured composite matrix, containing calcium phosphate, proteins and collagen. The extracellular matrix (ECM) itself, besides specific interactions between proteins, provides nanoscale features that provoke specific biological responses on bone cells. Thus, the incorporation of topographical or geometric nanofeatures that mimic the those of natural bone may offer surface and/or chemical cues (roughness, energy or wettability) that enhance osteointegration. Among the various approaches to provide nanofeatures to the surface of Ti-based implants, the fabrication of vertically oriented TiO₂ nanotubes (TNTs), has attracted a high interest recently. TNTs are one dimensional nanostructures that provide an increased surface area, nanotopography and highly controllable nanoscale roughness as well as an increased hydrophilicity, which makes them an interesting solution for surface modification of implant materials.^[61]

Indeed, TNTs have been shown to render the surface more attractive to cell attachment and tissue growth, enhancing osteointegration, in both *in vivo* and *in vitro* assays. Osteoblasts have shown increased alkaline phosphatase (ALP) activity and increased mineral deposition, which indicates a stronger bone forming ability. Similarly, MSC osteogenic differentiation is also more highly induced. Moreover, implantation of Ti implants with TNTs surface showed increased osteointegration, with absence of fibrous tissue formation in rats, as well as increased expression of collagen type-I (an early indicator of *De novo* bone formation) in pigs.^[62] The influence of nanotubes on bone cell response and bone regeneration has been attributed to several factors. For one, it is well known that, at physiological pH, TiO₂ gives up H⁺ ions forming negatively charged Ti-O⁻ groups, which attract Ca²⁺ ions in body fluids solutions to form a slightly positively charged calcium titanate layer, which subsequently attracts PO₄³⁻ ions resulting in the formation of unstable calcium phosphate (CaP) and, upon reaching thermodynamic stability, hydroxyapatite (Hap). In addition, the specific size of the nanofeatures of the produced nanotubes impact cell behaviour, specially the inner diameter of the nanotubes.^[61,62] This diameter dependent response was confirmed for different cell types, independently of chemistry (verified for TiO₂ and ZrO₂ nanotubes) and crystallization states.^[62] However, the triggered response varies depending on the cell. For MSC cells, diameters between 15 and 30 nm is optimal for increased cellular adhesion and proliferation as well as for ALP activity and bone matrix deposition. Higher nanotube

diameters of around 100 nm induce programmed cell death. For osteoblasts, on the other hand, larger diameters of 70 to 100 nm have been shown to accelerate cellular adhesion, proliferation, ALP activity and mineralization.^[61,62] This diameter effect seems to be related with integrin clustering on the cell membrane. In general, nanoscale topography present higher surface energy which translates into a higher protein adsorption (see section 1.1.4.1). Cellular adhesion to the material surface occurs through anchoring by the formation of focal points at cell membrane integrins. Filopodia and finger-like protrusions are produced to enable sensing of the optimum anchorage points, resulting in cell spreading over the surface. The higher the diameter, the more elongated it is the cellular morphology which, in turn, will elicit a cellular response due to mechanotransduction mechanisms. Bone cells possess various mechanosensors, namely, their cytoskeleton, mechanosomes, gap junctions and focal adhesion points (which transmit the mechanical stimulus into the cell). Mechanical stimulus will influence ALP activity, mineralization or even osteogenic differentiation of MSC cells.^[63] Similarly, TNTs may also have some immunomodulatory action (see section 1.1.4.3). Due to the same mechanotransduction cues that influence bone cells, macrophage elongation, upon adhesion to TNTs layers, can drive them towards the anti-inflammatory, pro-healing phenotype.^[35] Moreover, the interconnected spaces between the individualized tubes are thought to allow a continued flow of medium containing nutrients, gas and cell signalling molecules, a phenomenon that occurs naturally in human bone, but is not possible in bulk, flat surfaces.^[61,62]

Besides the increase in bioactivity, TNTs are also interesting as antimicrobial surface modification. Indeed, TiO₂ has a limited antimicrobial potential and various works on TNTs have described that these surfaces do intrinsically present some (if limited) antimicrobial action, which seem to increase with the increase in internal diameter.^[60] Thus, nanotubes seem to have a dual-action promoting on one side bone cell adhesion and on the other hand, hindering bacterial adhesion, tipping the race for the surface in favour of bone cells.^[43,64] However, their true potential lies in their nanoporous nature. The unique geometry of TNTs makes them useful as local drug-delivery systems, and thus they have been extensively researched as reservoirs for antimicrobial agents in active antimicrobial surface designs (see section 1.2.3.1). In this aspect, TNTs have been functionalized with compounds ranging from antibiotics and biomolecules (cell signalling) to inorganic agents such as Ag, Cu or Zn, presenting exceptional antimicrobial action, when compared with either non-functionalized TNTs or the deposition of the same agent in the bulk, flat surface of the substrate.^[61,65,66] However, the results are contradicting. Some reports show elution times over weeks while others report elution times of

minutes in the same conditions and for the same compounds. Usually, the kinetics of drug release from TNTs takes the form of an initial burst release, from the compounds accumulated in the initial open end of the tubes, which is followed by a steady release over time.^[67] Moreover, it seems to be dependent on TNTs length and diameter. Although some authors defend that burst release occurs in TNTs with diameters superior to 100 nm,^[66] other works suggest that higher lengths can allow to sustain a controlled release over time (with the effect being higher, the higher the diameter).^[67] A general consensus on this matter has established that in order to achieve a slow release, capping of the drug-loaded tubular structure with a biopolymer is required. A common strategies include plasma polymerization (which has been applied in delivery of water soluble drugs), or coating of biodegradable polymers (chitosan, glycosaminoglycans, etc.).^[66,67] In this last case, the application of simple cheap techniques such as dip coating or spin coating can decrease drug release by 30-60%.^[66]

1.3.1 Production of TNTs

The production of TNTs can be achieved through several processes (see Table 1-6). The first efforts relied on an electrochemical deposition method in an alumina template. These normally consist of nanotube/nanopore arrays of Al_2O_3 (obtained by anodic oxidation of an Al foil) that are later removed by selective chemical dissolution. The dimension of the nanotubes and pattern are determined by the dimension and pattern of the template. Later efforts included sol-gel techniques, hydro-solvothermal methods, chemical synthesis, atomic layer deposition among others, with or without templates. However, most of these methods are either costly, can have a high risk of contamination of the oxide layer, or do not guarantee an easy and reproducible production of the obtained nanotube morphology.^[67-69]

An important breakthrough was achieved in the work of Zwillig *et al.* in 1999^[70], which established that titania nanotubular structures can be also produced on the surface of Ti alloys, through an electrochemical anodization process in fluoride (F^-)-containing electrolytes.^[71] This is an electrolytic process in which the oxide grows through the action of an electric field, established by a DC power supply, that induces an ionic current in the electrolyte and forces electrons into the metal anode. As a result, metal cations are released into the electrolyte and will then react with oxygen (oxygen anions such as O_2^- or OH^- , usually provided by H_2O in solution or, in some degree, from the dissolution of pre-existent oxides or hydroxides) forming metal oxides at the surface

of the anode.^[69,72,73] Fluoride ions act as dissolution agents due to their ability to form water-soluble fluoro-complexes with metal cations, in this case, $[\text{TiF}_6]^{2-}$.

Table 1-6 – Comparison of some of the methods for the development of TNT.^[68]

FABRICATION METHOD	ADVANTAGES	DISADVANTAGES
TEMPLATE ASSISTED METHOD	<ul style="list-style-type: none"> ▪ Dimension of nanotubes can be controlled by the dimension and type of template used; ▪ Nanotubes formed are of uniform sizes; 	<ul style="list-style-type: none"> ▪ Large nanotubes are obtained; ▪ Time consuming due to the need of steps for the prefabrication and post-removal of templates; ▪ Contamination may occur during the dissolution of the template;
ANODIZATION	<ul style="list-style-type: none"> ▪ Dimension of nanotubes can be controlled by varying voltage, electrolyte, pH and anodizing time; ▪ Nanotubes produced are aligned with a high aspect ratio ▪ Reproducible, cheap and low temperature technique. 	<ul style="list-style-type: none"> ▪ Nanotubes produced have an amorphous phase; ▪ Annealing is required to crystallize the nanotubes produced but it can lead to collapse of the structure at elevated temperatures.
HYDROTHERMAL OR SOLVOTHERMAL TREATMENT	Pure phase nanotubes with good crystallinity can be obtained.	<ul style="list-style-type: none"> ▪ Long reaction time is needed ▪ Concentrated NaOH must be employed that can lead to excessive intercalation causing non-aligned nanotubes

In their absence, the resulting anodic oxide is a compact flat barrier layer, which is the normal outcome in classical anodization processes. In their presence, however, the process can result in either continuous metal dissolution, leading to electropolishing, or in the formation of a porous oxide, if a balance between the solvatization of the metal (or metal oxide) and oxide formation is established.^[67,69,74]

Numerous works in the following decades would establish electrochemical anodization as a cost-effective solution, that allows a direct control over the shape and size of the nanotubular arrays, in a reproducible way. Key to achieve a controlled growth, is to adjust the dissolution rate of TiO_2 by the fluorine species. For this purpose, several process parameters can be optimized such as the electrolyte composition, the applied potential difference, cathode material, the process time or the temperature. In this regard, several reviews are available in the literature that summarize the state of the art of the production of TNTs through electrochemical anodization. Of special interest to this work, are the ones of Roy, et al. 2011, Kowalski et al. 2013, Tan *et al.* 2012, Indira et al. 2015 and Regonini et al. 2013.^[61,67–69,75]

1.3.2 Electrochemical anodization of Ti in F^- containing electrolytes

Electrochemical anodization for the production TiO_2 nanotubes is usually carried out by applying a potential step (or ramp) at a constant voltage between 1-30V in an aqueous electrolyte or 5-150V in nonaqueous electrolytes containing approximately 0.05M-0.5M (0.1-1wt%) fluoride ions (and usually some background ion species). The anodization reaction can be characterized by current-voltage curves. From these curves, threshold voltages values for oxide formation (U_p), or the rates of electrochemical processes (for example ion migration) may be determined. A typical I - t curve for conditions that lead to nanotube formation is shown in Figure 1-5. The curve shows three stages: I) in the initial stage of anodization the curve essentially follows the fluoride-free case, with the formation of an initial compact oxide layer; II) a current increase leads to the initial formation of irregular nanoscale pores which penetrate the initial oxide compact layer (the current increases as the reactive area increases), these pores then are further deepened and adjacent small pores are usually incorporated into the larger pores; III) the current drops again as a regular nanopore or nanotube layer forms. After self-organization, tube growth continues at steady current densities.^[67,69,74,76] For extended anodization periods, tube growth may be determined by diffusional effects and agitation (and gravity effects) and viscosity (influence on the diffusion constant) may become important.^[69]

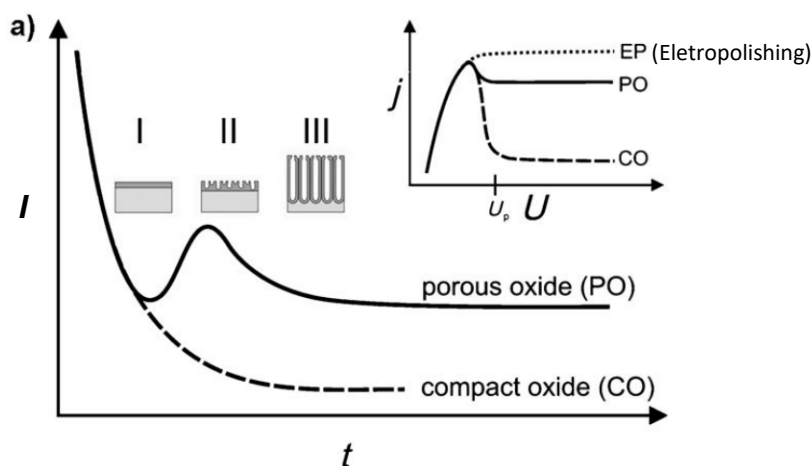


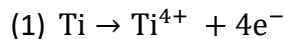
Figure 1-5 – Typical current-time (j - t) characteristics, at constant voltage, of electrochemical anodization of Ti. (—) in the absence of F^- and (---) in the presence of F^- .^[67]

1.3.2.1 Phase I: Initial stage of anodization

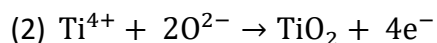
In the first seconds of anodization, a compact film is formed in a similar way to that of the formation of a barrier type (flat) anodic oxide. Briefly, the applied potential establishes an electric field, leading to metal cation formation (Ti^{4+} , equation 1), high-

field migration, through the oxide, of cations toward the metal/film interface and of anions (O^{2-} , OH^- , created by field-aided deprotonation of water, equation (6) through the film/electrolyte interface by a cooperative mechanism.^[68] Thus, the film is formed at both the metal/oxide and the oxide/electrolyte interfaces, according to Equations (1)-(5). Basically, at the metal/oxide interface:

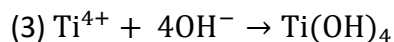
- Anode:



and simultaneously,



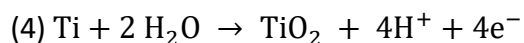
or



The metal (Ti) ion (Ti^{4+}) formed in (1) is consumed for the film development (3) and/or released to the electrolyte.

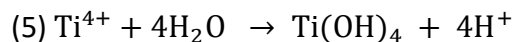
At the oxide/electrolyte interface we have the outward migrating metal ions that react with water:

- Anode:

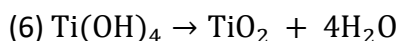


H^+ ions accumulate in the electrolyte.

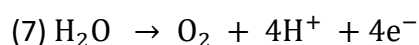
and



Moreover, the hydrated layer releases water forming new oxide:

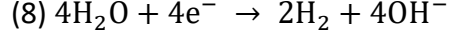


The structure of the anodic oxide consists of a less dense oxide layer grown at the oxide/electrolyte, containing oxyhydroxides (Ti(OH)_4), and a more dense oxide layer, grown at the metal/oxide interface, of stable TiO_2 .^[69,77] As the oxide grows, the metal atoms leave the substrate and move through the stationary oxide lattice, by jumping through interstitial positions, towards the electrolyte, where they react with anions in solution forming new oxide and creating both a vacancy and interstitial position in the existing oxide.^[77,78] Simultaneously, anions move through the oxide towards the metal oxide interface.^[79] In view of the thermodynamic stability of water, the above reactions are normally accompanied by oxygen evolution:



This reaction is typical to occur in the anodization of Ti, due to good electronic conductivity of the formed titania layer.^[68] Simultaneously, the counter reaction, which is hydrogen evolution, takes place at the cathode:

- Cathode:



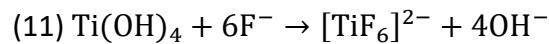
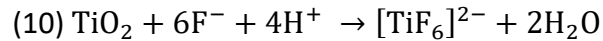
The growth of anodic compact oxide follows Faraday's law and is characterized by a growth constant. In an electric field ($F = U/d$), if under a constant voltage, U drops constantly, lowering the driving force (for solid state ion migration) with the increase in film thickness, d . At some point, the thickness and density of the oxide will be such that the overall electric resistance of the surface will end the oxidation process. This translates in an exponential drop in the anodic current with time, as seen figure 1-3, until the field effect is lost, at which point final thickness is reached and the current is at minimum. The final thickness can be related to the applied voltage through (7):^[68]

$$(9) d = fU$$

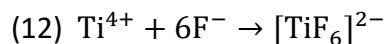
where f defines the formation ratio or growth factor and d is thickness. However, the exact value of the formation ratio (or anodization ratio) depends on the anodization conditions: applied potential, working and counter electrode, electrolyte composition.^[68]

1.3.2.2 Phase II: Chemical dissolution of Ti and TiO₂ by fluoride ions.

If the electrolyte contains fluoride species, the accumulation of H⁺ (due to eq. 3 and 4) can lead to migration of F⁻ to the proximity of the growing oxide layer, to ensure electroneutrality. When the concentration of F⁻ ions reaches a critical level, at local regions, the dissolution of TiO₂ (or Ti(OH)₄) occurs, forming water-soluble fluoro-complexes [TiF₆]²⁻ according to Equations 10-11:^[68]



In addition, F⁻ can also react directly with the arriving Ti⁴⁺ according to equation 12. Moreover, F⁻ has a small ionic radius, being transported through the lattice of the growing TiO₂, by the applied electrical field, at twice the rate of than O²⁻.^[78] Once in the oxide, F⁻ compete for the sites of O²⁻. As a result, a fluoride-rich layer is formed at the metal-oxide interface, (which can be detected by SEM and a thin salt film is visible on the dimples of the titanium metal substrate after lifting off the TiO₂ nanotubes).^[69]



Dissolution of the Ti cations could create negatively charged vacancies at the oxide which would migrate towards the metal/oxide interface due to the potential gradient across the oxide. In turn, this would facilitate the reaction (1) and the Ti^{4+} would easily jump to the available vacancy sites. Thus, the resistance of the oxide film is decreased, and a rise in the current occurs, which characterizes this stage as depicted in Figure 1-5.^[71,74] Moreover, as the complex is water soluble, the effect of local current distribution may lead to localized loss of Ti^{4+} (due to localized accumulation of F^{-}) which may be responsible for the initial formation of nanoscale pores.^[68] As the pore grows, the hydrolysis of Ti (Equations 3-4) occur concurrently with the chemical dissolution by fluorides (Equations 10-11). There is a local increase of H^{+} at the bottom of the forming narrow pores, establishing a pH gradient along the pore. As a result, F^{-} ions tend to migrate to the pore bottom resulting in an even higher dissolution at those areas when compared to the surface of the oxide. Moreover, due to the applied electric field, the Ti-O bond undergoes polarization and weakened which further promotes the dissolution of the metal oxide. Thus, pore growth proceeds through pore deepening in an autocatalytic fashion.^[68,71,76]

The outcome of these reactions strongly depends on the amount of fluoride ions present. Below 0.05 %wt., a stable compact oxide layer is formed. Equal or above to 1 %wt., no oxide formation can be observed, as all the Ti^{4+} immediately reacts with the abundant F^{-} to form soluble $[\text{TiF}_6]^{2-}$ (the reaction may then be controlled by diffusion of hexafluoro complex from the surface, and electropolishing of the sample occurs). For intermediate concentrations, a competition between the oxide formation and Ti^{4+} solvatization can be established. The amount of formed $[\text{TiF}_6]^{2-}$ will depend on the amount of Ti^{4+} transported under the electric field to the surface of the oxide (as long as sufficiently high concentration of F^{-} species is present at the surface) in the anodic reaction. Fluorides have a dual effect, maintaining a thinner bottom oxide layer and provoking immediate complexation (solvatization) of Ti^{4+} species arriving at the oxide-electrolyte interface.^[69]

1.3.2.3 Phase III: Self-organization the porous oxide to the nanotube layer.

Phase III is characterized by a quick drop in current until reaching a steady state condition. During this stage, the formed nanopores undergo a process of self-organization into nanotubular structures. For TiO_2 nanotubes to be formed, it is essential the presence of F^{-} and that steady state conditions between oxide formation (equations

4-6) and dissolution by fluorides (equations 10-12) can be established.^[68,74] These steady state conditions, typically involve a constant rate of oxide formation and dissolution, explaining the constant current that signalizes this stage.

The exact mechanism through which self-organization is achieved, and constant current growth occurs, is still matter of debate. It is believed that initial pore growth occurs through preferential growth of deeper pores (“strong” pores) with regard to less deeper pores (“weak” pores). The deeper the pore, the highest local acidification (equations 3-4) and, as such, electrochemical oxidation thus occurs preferentially at these sites. On the other hand, the weak pore generates a smaller amount of H^+ and its growth becomes slower and slower. Thus, pore growth advances in an autocatalytic fashion. The growth direction is influenced by neighbouring pores and, as such, the growth initially occurs into worm-like structures.^[77,80]

The definition of the tubular morphology and growth of the tubular structure after self-organization, was initially believed to be the product only of a field-assisted dissolution mechanism. Briefly, after strong pore “selection”, the pores continue to growth until reaching self-organization.^[77] Self-organization is, thus, achieved through pore deepening at the bottom, and oxide dissolution at the top. The oxide grows through a balance between, the formation of oxide and oxide dissolution. Synergistically, these two process would lead to self-organization and the establishment of the nanotubular morphology. The rate of these reactions is determined by the strength of the applied field. These reactions would continue up to a point where the dissolution prevailed and the growth stopped.^[76,81] However, a more recent model was proposed by Garcia-Vergara for alumina^[82], and later confirmed by DJ LeClere for Ti^[79] describes a field-assisted flow mechanism, in which growth occurs due to a displacement of the oxide from the bottom layer towards the tube walls, due to compressive stresses resulting of electrostriction. The flow occurs due to the plasticity of the of the barrier layer. This has later been corroborated by the work of Berger *et al*^[83] which demonstrated the accumulation of fluoride-titanate layer at triple-point junction in-between the nanotubular walls. This indicates that the fluoride rich layer that is formed on the bottom of the oxide, described previously flows towards the tube walls.^[69,74] This fluoride-rich layer in between tubes is thought to be the main reason for the transition from pore to tubular shapes, which is thought to occur through splitting by dissolution.^[84]

The expansion factor when a metal is converted into an oxide is given by the ratio of the volume of the oxide to the volume of the metal consumed. This factor is known as the Pilling-Bedworth ratio (PBR). The expected PBR of amorphous TiO_2 is 2.43, but in reality, the tubes grow much larger than what was expected with an expansion factor of

about 3. Indeed, while the film is evolving in phase I, the expansion factor is in agreement with the PBR value. However, pore initiation and field-assisted flow will lead to much higher expansion factors. The expansion factor, together with the electrostriction due to the applied electric field, will generate internal stresses in the oxide. The fluoride-rich layer in between tubes can act as a weak spot for stress, which can contribute to its dissolution.^[69,74,75,84]

1.3.3 Parameters affecting TNTs growth and morphology

1.3.3.1 Electrolyte composition

TNTs were produced in a wide variety of fluoride-containing electrolyte compositions. Both the fluoride source, and the solvent, have an effect on the morphology and overall microstructure of the produced nanotubular layer. In order to optimize the process, and achieve tubular morphologies of interest, optimization of the F⁻ content, variations of the electrolyte pH and the use of different cations have been investigated by using both different F⁻ ions sources and different supporting reagents. In this aspect, today, it is common to distinguish, generally, the different electrolytes into water based (or aqueous) or organic-based electrolytes. The evolution of the method, with regard to electrolyte composition, gave rise to four distinct synthesis generations for the production of TiO₂ nanotubes.^[75]

A first generation corresponds to nanotubes produced under HF-based electrolytes, based on the initial findings by Zwilling.^[70,71] These were aqueous HF electrolytes, characterized by a low pH and a strong dissolution of both the Ti substrate and the top TiO₂ layer (equations). The produced nanotubular layers were up to 0.5 μm in length, with a lower degree of organization and considerable side wall inhomogeneity. The effect of the low pH of the solution seems to be twofold, provoking on one hand a higher dissolution at the tube top (as per equation 8 - see 1.3.2.2) and, on the other, inhibiting the amount of oxygen anions in solution (equation 5, see 1.3.2.1), thus inhibiting the oxidation of Ti.^[74,75,85] According to Macak *et al.* side wall inhomogeneity (or ribs) could be associated with pH bursts at the base of the tubes, as the anodization progressed.^[86]

A second generation was characterized by the development of higher aspect-ratio nanotubes. This was achieved by altering the fluoride source to fluoride salts such as Na₂SO₄/NaF or (NH₄)₂SO₄/NH₄F. The first direct effect of was an increase in pH which allows a higher control over the dissolution rate of TiO₂ (by inducing local acidification at

the pore-bottom while higher pHs are established at the pore mouth reducing dissolution of tube tops - see 1.3.2.2. and 1.3.2.3).^[76] In addition, the fluoride source has distinct chemical behaviours in solution which potentially influences the process. HF is a weak acid with pH-dependent partial dissolution. On the other hand, both NaF and NH₄F have complete dissolution, which results in higher concentrations of free F⁻ and higher current densities. Moreover, Na⁺ is a neutral ion and does not affect the anodization reactions while NH₄⁺ and H⁺ increase the H⁺ concentration in solution.^[86]

A third generation was achieved by replacing water, as a solvent, by organic compounds, such as Ethylene Glycol (EtOH), formamide, N-methylformamide, dimethyl sulfoxide (DMSO), or glycerol. This allowed the production of nanotubular layers characterized, generally, by a well-defined honeycomb-like structure on the top, smooth tubular walls and very long lengths (up to 1000 μm thickness).^[86] The use of organic solvents in the electrolyte has multiple effects. First, the increased viscosity leads to lower ionic conductivity. Moreover, organic electrolytes can react with ions in solution, capturing them and affecting the availability of certain species. For instance, F⁻ ions can be captured by organic compounds, such as ethylene glycol and formamide via hydrogen bonding. For a concentration of NH₄F in the range of 0.1 % wt to 0.5% wt., normally the majority of F⁻ ions in solution will be captured by the organic compounds.^[87] In this type of electrolytes, water is generally the only source of oxygen for the formation of TiO₂.^[75] Thus, water acts as both a supplier of oxygen ions for oxide formation, and solvent for [TiF₆]²⁻, affecting both the growth rate and etching speed (chemical dissolution rate) of the nanotubes.^[67,69] A common practice to ensure oxidation of the oxide layer, in organic electrolytes, is oxide ageing, which is often required to obtain highly defined tubes. Ageing involves repeated anodization of dummy titanium sheets before the sample target is prepared. The effect of ageing is twofold, on one hand it alters the composition of the electrolyte by increasing the [TiF₆]²⁻ content (lower TiO₂ dissolution), and by allowing absorption of moisture from the environment reaching of a steady water content in the electrolyte (for example, ethylene glycol is relatively hygroscopic and can take up considerable amounts of water from the environmental air). Maybe for this reason it is considered that the conductivity of the electrolyte increases linearly with electrolyte ageing.^[69] As a result, until a certain number of repetitions, there is an increase in thickness of the nanotubular layer, the nanotubular morphology is more defined, and is generally obtained higher pore diameter with smaller wall thicknesses (which can be attributed to a more pronounced oxide etching).^[88]

A fourth generation was achieved by replacing fluorides by other halides including bromide, perchlorate and chloride ions. These fluoride-free media allow the

development of long TNTs that can be grown in a very short time (growth rate is >1000 times faster than in fluorine containing electrolyte). However, in some cases such as the bromide-containing electrolytes, the produced TNTs do not present a self-organized structure similar to that observed in fluoride-containing solutions.^[72,75]

In conclusion, TNTs formed in these aqueous electrolytes can be grown only up to a few micrometers, are typically not uniform in shape, present a “very clean” top (any initiation layers and other inhomogeneities are etched off) and contain many ripples on the tube walls. These ripples if connected, make the structure more mechanically stable. Moreover, there is an increase in the inter-tubular space between the tubes. This is due to the faster etching speed (chemical dissolution rate) of titania and of the fluoride rich layer between the tubes, compared to the growth speed of the tubes into underlying substrate, owing to high water content.^[69] In organic electrolytes, where the water content is considerably lower, the chemical dissolution of TiO_2 is mainly dependent upon the time and voltage control. Typically, TNTs formed in this type of electrolyte present longer nanotube length, smooth tube walls, and a reduced inter-tubular space owing to the slower etching rate. High aspect ratios up to 2000-3000 and better organized TNT layers can be obtained.^[68]

1.3.3.1 Applied potential and Current Density

The applied potential difference directly influences the pore diameter, inter pore distance and film thickness of TNTs.^[68] This relationship exists with voltages from 5 to 30 V, in aqueous electrolytes, and 10 to 60 V in organic electrolytes. This effect has been described in several different electrolytes, either aqueous or organic, provided that the concentration of the fluoride species is in the range for nanotube formation. The value of applied potential represents the sum of potential difference at the metal-oxide interface, across the oxide, oxide-electrolyte interface and across the electrolyte. Thus, it will directly affect ion migration and the etching rate, and, in addition, the pH gradient that is established across the tube.^[72,75]

Anion and cation transport rate will generate compressive and tensile stresses on the oxide.^[89] The tensile stresses reduces the force needed for ions/atoms to escape from the oxide layer and the compressive stresses increase the force needed for ions/cations to leave from the oxide layer. According to the direction of the electric field with regard to the pore bottom, the tensile stresses will be predominant on the base of the pore while the side of the pore will suffer from compressive stresses. Thus, the higher the applied potential, the higher the diameter of the generated pore.^[90] Some works state

that, at very high voltages, there is a decrease in nanotube diameter, which seems to be limited by the dissociation of water.^[75]

Moreover, it also affects the expansion factor of nanotubes, depending on the dissolution by the electrolyte (which depends on other parameters). High applied voltages and low water contents normally result in high expansion factors. As such, the thickness of the nanotube layer depends linearly on the anodization voltage. However, due to etching by the electrolyte, at some point an equilibrium state between the growth of the oxide and chemical dissolution exists. As the etching rate is faster in acidic mediums, tube length is limited to 500-600 nm in electrolytes with low pH. In neutral electrolyte systems, layer thickness up to 2-4 μm can be obtained.^[69]

The effect of voltage on tube diameter and inter-tube spacing can be ascribed to the same effect that it has on pore nucleation and pore to tube transition, which results of the field effect and F^- mobility within the electrolyte (thus, faster or slower accumulation). As described before, the selective etching of the fluoride rich layer in between tubes, which may result also from the synergistic role of applied tresses, will eventually shape the tubes.^[84,90]

In principle, tubes can also be grown under galvanostatic conditions. Different current densities directly affect the etching rate and therefore can, theoretically, produce different pore sizes. As current density increases, the electrochemical etching rate, power and electric field intensity also increase. As a result, there is pit widening (before the formation of channels), to form separate pores, or an increase in the pore diameter. However, current density is influenced by electrolyte composition (which changes over time, with ongoing anodization) and the potential difference across the entire system (which, if not constant, can vary with availability of charge carriers or decreased viscosity, later on). Thus, the drawback of this method is that, since the voltage changes with time, control over tube diameter is lost.^[67,68,75]

1.3.3.3 Temperature

The variation of the temperature of anodization will influence electrolyte conductivity. In general, the higher the temperature, the lower the viscosity and therefore the higher the dissolution rate or etching rate of the oxide. This was experimental verified by Seçkin and Ürgen, which have demonstrated that, maintaing similar conditions of electrolyte composition, applied potential difference and time, a low temperature (of 5°C) will lead to longer times to pore nucleation than a higher temperature (25°, room temperature RT) and the thickness of the tubes (the growth rate) is lower, the lower the temperature.^[91] Nasipouri *et al.*, in an anodization process using

an organic based electrolyte at 80 V obtained hexagonal nanotubes at 0°C, and circular-shaped nanotubes at 30°C.^[92] Lai *et al.*, performed anodization on pure Ti for temperatures ranging from 10 to 80°C, using always the same composition in the electrolyte solution (neutral inorganic electrolyte), voltage and time. The results show that the variation in TNT morphology regarding diameter, wall thickness and length could be divided into two sections or range. Section 1 ranged from 10 to 27 °C and showed a clear increase in pore diameter and length, and a decrease in the wall thickness. These results are in accordance accelerated chemical etching due to the increment of the viscosity. However, above 27, (section 2 from 27 to 80°C) there was a slight decrease in length, a more pronounced decrease in diameter and also an evident increase in the wall thickness. This is due to a change in the overall composition of the electrolyte, with an excess of diffusing Ti^{4+} ions and O^{2-} ions that led to a faster anodic oxide formation than chemical etching.^[93] Thus, the temperature influences the overall geometry, including the nanotube diameter, length and wall thickness of the nanotubes.^[68,94] However, the effect of the temperature will be dependent on the electrolyte composition. Other studies report unstable bundles of TNTs with no regular structure on temperatures above 40°C, by using organic electrolytes.^[87,93]

1.3.3.4 Counter Electrode

The overpotential of the counter electrode (CE) affects the dissolution kinetics of the Ti anode and, thus, the activity of species in the electrolyte and the morphology of the developed nanotubes.^[68] In terms of stability in aqueous electrolytes, the arrangement of the cathode materials is in the following order, according to Allam *et al.*^[95]:

$$\text{Pt} = \text{Pd} > \text{C} > \text{Ta} > \text{Al} > \text{Sn} > \text{Cu} > \text{Co} > \text{Fe} > \text{Ni} > \text{W}$$

This arrangement of cathode materials is based on differences in morphology, current density and stability (by determined mass loss) for the same electrolyte. However, the performance of the material is dependent on the composition of the electrolyte, which directly affects the overpotential of the cathode.^[95] Sreekantan *et al.*, developed TNT using Fe, C, Pt, Al and stainless steel, in an organic electrolyte of different composition. The results show that carbon was the material best placed to replace Pt in the group, and Al with a behaviour between Pt and stainless steel.^[96] However, debris formation resulting of cathode material can occur, and longer anodization times may be necessary to achieve similar morphologies. The higher the amount of dissolved Ti in the electrolyte, the higher the conductivity, which helps preventing debris formation.^[68]

1.3.3.5 Electrode Distance

The distance between working electrode (WE) and CE influences electrolyte conductivity (the lower the distance, the higher the conductivity). Thus, the narrower the inter-electrode spacing, the higher the rate in the electrode reactions, which promotes oxide growth and chemical dissolution. As such, a decrease of the anode-cathode distance leads to larger pore diameters, wall thickness and inter-tubular spacing.^[68,89] The number of nanotubes obtained, however, increases with an increase in the distance between the electrodes. Moreover, this can also lead to a significant decrease in pore size and inter-tubular space.^[68] This could be probably due to a significant IR drop in along the current path in the electrolyte, which reduces the field strength.^[97] This effect, however, will be dependent on the applied voltage: the higher the voltage, the more sensitive is TNT formation to changes in the electrode distance. Moreover, some works do not report any changes in inter-tubular spacing with variation in the inter-electrode distance., which point to a possible influence on the electrolyte composition.^[98]

1.3.3.6 Time

The anodization time has a great effect on the morphology of the nanotube layer. The increase in time has been described to lead to enlargement of tube diameter, enlargement of inter tube spacing, a decrease of tube wall thickness and an increase in tube length.^[99,100] This is due to the etching action of the electrolyte. In general, the longer the time, the longer the steady state is maintained between metal oxidation/chemical dissolution, which explains the morphology variations reported by different authors. It is also important to note that for short anodization times no nanotubes are formed. For instance, in aqueous electrolytes, for an anodization time of 5 min, only a nanoporous layer can be formed, and a minimum of 15 minutes is necessary for nanotube formation. Thus, the increase in anodization time leads to an improved homogeneity and degree of self-organization, i.e., more defined and well-organized tubular structure are obtained. Thus, time is linked to nanotube development.^[68,69]

As such, identification of optimal anodizing time for a given set of conditions (electrolyte, applied potential, fluoride concentration, etc.) is required to obtain optimal morphology for an intended application.^[68,97] In aqueous media, nanotubes grow only a few micrometres which is achieved between 30 to 2 h of anodization. In contrast, the growth process in organic electrolytes is much slower and dissolution phenomena are not as significant, so the anodization time can be extended from several hours up to a day and is generally possible to obtain well-organized NTs with length over 10 s of μm .

However, extended anodization times, leads to extended etching at the top of the tubes, which can result in the formation of inhomogeneous, spike-like structures structure on the tube tops. These are usually known as nanograss which become too thin to support their own weight and collapse. Thus, there is an interval of time to which well-defined nanostructures and a maximum length of the NTs, can be obtained.^[69,97]

1.3.3.7 Ti alloy composition and structure

As described previously in section 1.1.1, there are currently 39 different standards that comprise a wide variety of Ti alloys, with different compositions and structure, comprising grains of different sizes, with distinct chemical composition and/or crystalline phases or crystalline orientations. A such, and in accordance with what was described in the previous points, it can be expected that both the composition, crystalline phase and phase orientation can somehow influence the growth TNTs layers. In aqueous electrolytes, it has been shown by some authors that some grain orientations in Cp-Ti can retard the growth of nanotubes. However, in the works of Sopha *et al.* grain orientation, when nanotubes were grown in an ethylene glycol electrolyte, had no effect whatsoever either on nanotube morphology or growth kinetics.^[97] Nevertheless, Krbal *et al.* have shown that, in spite of that, they can have an influence in specific tube properties such as the photo-electrochemical response.^[101] Similarly, other works explored the effect of chemical composition on the growth and morphology of nanotubes layers. In general, if the alloy composition is uniform across the different grains, with singular crystalline phase, then the grown nanotubular layer is uniform morphologically. This is normally the case observed in Cp-Ti as well as Ti-Mo, Ti-Zr or Ni-Ti alloy. Nevertheless, the chemical composition plays a role in the growth rates of the tubes, which can lead to different diameters, wall-thicknesses and lengths of different alloys anodized with the same electrolyte composition and at similar applied potential differences and times.^[102]

However, if the alloy present distinct grains such as $\alpha+\beta$, microstructure, a dual-phase can be observed, presenting either nanotubes with different features as it was observed in tubes grown in the binary TiNb alloy, or the occurrence of pores in the anodic oxide, whose size and distribution were closely related with the biphasic microstructure of the alloy. Such situations were first described by Zwilling *et al.*^[70] for Ti6Al4V alloy, in water based electrolyte, and later by several authors in different works who report that in the α -phase region the anodic oxide presents self-organized nanotube arrays, while the β -phase region presents either irregular nanoporous structure or underwent complete dissolution. In particular Macak *et al.*^[103], by performing potentiostatic anodization at the same conditions on Ti6Al4V and Ti6Al7Nb, reported nanotubes grown

on the β -phase only on the Nb-rich β grains and not on the V-rich β grains, even though the production of nanotubes on Ti-V alloys has been thoroughly described in other works.^[104,105] The use of organic electrolytes for the anodization of Ti6Al4V was reported in few works and most of them were related to ethylene glycol based electrolytes.^[102] Among them, the recent work of Jordanovová *et al.* clearly showed the differences on the morphology of the anodic oxides grown over α and β phases.^[106]

1.3.4 Properties of TiO₂ nanotubes produced through anodization

For the scope of this project, only the properties pertaining to osteointegration, and bioactivity will be analysed. Optical and electronic conductivity properties are outside the scope of this work.

1.3.4.1 Morphology

The TiO₂ oxide produced through electrochemical anodization of Ti alloys in fluoride containing electrolytes can have different morphologies, from nanopores (which can be, or not, hexagonally shaped) to well-defined nanotubes, more or less uniform in size, to nanograss structures (which result of excessive dissolution by the electrolyte and consequent thinning of the tube walls), which collapse and bundle over the tube tops, forming spikes or clusters. All these different morphologies can be obtained by adjusting parameters of the anodization process as described in section 1.3.3, and can be attributed to different high-field effect growth factor for the oxide.^[68,69] However, both Roy *et al.* and Seçkin and Ürgen, propose that, while at first sight, these morphologies appear to be significantly different, they should be considered just phases of the process of self-organization and growth of TiO₂ nanotubes.^[67,91] Under constant voltage, the growth of TNTs can be followed by the current-transient (Fig. 1-5) curve and divided into three different phases. Phase I (see section 1.3.2.1) is characterized by the formation of a barrier layer, phase II (see section 1.3.2.2.) is characterized by pore initiation in the barrier layer and phase III (see section 1.3.2.3) is characterized by nanotubular growth from the base pores. The film thickness and self-organization will increase with time, and nanograss can be formed upon extended anodization periods (see section 1.3.3.6).^[67]

Seçkin and Ürgen recently proposed a new kinetic model of growth of TiO₂ nanotubes, which offers a new perspective with regard to morphological development. According to this work, TNTs growth can be divided into three stages. Stage 1 is characterized by initial barrier oxide formation, pore initiation and nanotube growth (comprising all three phases of the current-transient model). Thus, during this stage we

have initial a compact barrier layer that, first, becomes porous, and whose porosity increases with time, until tubular development begins (as described in section 1.3.2.2). It is important to note that, during this phase, TNTs occur below a compact porous layer on the top, and thus, from a top-view, it could be described as a compact porous oxide.^[91] This phenomenon has been described in organic electrolytes (but not in aqueous) and has been associated with the low water content and low dissolution in these oxides.^[67,75] Chemical dissolution is detrimental for the final morphology of the produced nanotubular layer. At one hand, field-assisted dissolution at the tube base induces tube growth and defines the diameter, on the other hand, dissolution of the oxide at tube top limits the thickness and growth. The presence of the initial barrier layer, on the top of the forming tubes, can be seen as a protection against dissolution which allows for higher thicknesses (as described in section 1.3.3.1). Nevertheless, increased anodization time will lead to complete dissolution of this layer. This marks Stage 2, which is defined as the period of time during which open-top ordered nanotubes are visible. During this, the fluoride rich layer between tubes is dissolved and well-defined ordered nanotubes are visible. Stage 3 quickly follows stage 2 and is defined as a period for chemical dissolution of the tube tops. As the chemical dissolution proceeds, the weakened parts of the tubes begin to be unable to carry their own weight and collapse onto each other resulting in the inhomogeneous, spike-like structures structure (nanograss). The accumulation of thinned tube residues increases with time, with the nanograss layer becoming denser. Moreover, the tubes begin to become shorter in length.^[91]

Other morphologies such as tube stacks, bamboo-like, nanolace or branched tubes can be obtained under controlled electrochemical conditions, but are not of interest in the scope of this project for which only well-defined nanotubes are of interest.^[67] These are characterized by their length, pore diameter, wall thickness, wall roughness, and inter-tube spacing, and as described in section 1.3.3, they be defined by adjusting parameters of the anodization process.^[75] In general TNTs grown in F⁻ electrolytes, present a V-shaped side-wall, which is due to the etching exerted by the electrolyte. The inner part of the tubes is less compact and contains impurities from the electrolyte (see 1.3.4.2), while the outer part is more compact and, typically, made of dense TiO₂. A striking aspect of the morphology of the tubes, is that smooth tube walls are obtained for low water content of the electrolyte, whereas higher water contents can lead to wall ripples. Moreover, aqueous electrolyte usually result in tubes with increased inter-tubular space and small lengths (up to a few microns). Organic electrolytes, on the other hand, tubes usually have high aspect ratio, smooth walls and a higher degree of organization.^[67,75,86]

1.3.4.2 Composition

The composition of as-anodized TiO_2 has been thoroughly studied by energy dispersive X-ray spectroscopy (EDXS) and X-ray photoelectron spectroscopy (XPS).^[68] Normally, due to thin nature of most produced nanotubular layers, EDXS can also report results regarding the composition of the underlying substrate and, thus, is not as accurate as XPS. Usually, the produced nanotubular layer mainly consist of TiO_2 .^[101,102] However, depending on the alloy composition, oxides of alloying elements may be present.^[70] In this case, more than one metal ions species migrates towards the oxide electrolyte interface, albeit at different speed and the cation that migrates faster is usually is the main constituent of the produced oxide.^[68] However, depending also on the stability of the formed oxide they can be completely dissolved in the electrolyte, or not.^[72,103]

Moreover, ionic species from the electrolyte can be incorporated in the oxide film of the nanotubes. The nature of these species is highly dependent on the composition of the used electrolyte. The most common example are fluoride ions, by the mechanisms described previously (see sections 1.3.2 and 1.3.3), being normally detected on the tube tops and across the entirety of the tubular length, with its concentration being usually higher at the pore bottom than the pore tip.^[68,69,83,86] Similarly, other supporting reagents can also be incorporated. For instance, in ammonium pentaborate electrolyte, boron species are found distributed ca. 10% of the oxide accumulating close to the oxide surface region. However, in disodium molybdate electrolyte, the incorporation of foreign species does not occur. The incorporation of species from the electrolyte could be attributed to the ionic migration. It is also possible that small anionic species from supporting reagents are incorporated in the oxide in a similar fashion to oxygen anions and fluorides. Their maximum depth depends on inward migration rate. On the other hand, outward migrating metal cations can react with specific anions of the electrolyte, at the oxide-electrolyte interface, which, with oxide growth, get incorporated in the tube, possible buried under newly formed oxide. In many cases the inward migration of electrolyte ion species is much slower (are immobile or migrate outwards) than oxygen ions and therefore some species can only be distributed just in a part of the oxide total thickness.^[68]

Moreover, in the case of organic electrolytes, the inner tube layer shows an extremely high uptake of carbon from the electrolyte, presenting an inner carbon-rich contamination layer in organic electrolytes. This can be explained by a voltage-induce Schottky breakdown mechanism is operative for high-voltage anodization, leading to a

decomposition of the organic electrolyte. In aqueous electrolytes, the inner tube layer is typically more hydroxide-rich than the outer layer.^[69] Carbon species are usually considered immobile under the applied electric field, thus their incorporation usually occurs through the outward migrating metal cations. It is possible that this is a result of voltage-induced decomposition of the organic solvent, which has been observed for ethylene glycol.^[68]

1.3.4.3 Phase structure

TiO₂ exists naturally or in an amorphous state or mainly in three crystalline phases: anatase, rutile and brookite. Rutile is the most thermodynamically stable bulk phase. However, at a nanoscale, surface energy and stress have a significant effect on phase stability. The surface energy depends on the number of uncoordinated Ti cation sites. Fourfold-coordinated centres have larger surface energy than those with fivefold coordination, and the surface energy increases with the number of uncoordinated positions. As a consequence, at a nanoscale (<20 nm), anatase is considered to be the most stable (although some disagreement exists in literature).^[69] The structure of the oxide films on TNTs obtained through electrochemical anodization is strongly dependent on the specific electrochemical parameters described in section 1.3.3. Generally, for anodizations conducted at room temperature, in fluoride containing electrolytes, it has typically been reported to be amorphous at low anodization voltages and crystalline for very high anodization voltages.^[68] However, the composition of the electrolyte can influence the obtained crystalline structure. The presence of ionic species such as Cl⁻ or F⁻ in the crystal lattice can also influence the stability of certain polymorphs. Rutile is more stable in the presence of chloride ions, whereas in fluoride-free electrolytes anatase can be more easily obtained.^[69]

To change the crystalline structure of the produced nanotubes, from amorphous to a crystalline phase several works have demonstrated that a high-temperature annealing treatment (or thermal treatment) is an effective solution. This can be achieved in atmospheres with or without oxygen. Until a temperature of 280°C the anatase phase starts to appear and the phase becomes predominant at 350°C (long term annealing) or 450°C (short term annealing). However, short term annealing at 450°C can result in defects on the tube walls when compared with long term annealing at 350°C. Fractions of rutile phase appear above 500°C, and become predominant above 900°C. Moreover, besides the annealing temperature, treatment duration, ramping speed (typically, 1°C/s) and whether metal substrate is present can influence the phase transition and final structure obtained. The thermal treatment in oxygen containing atmospheres leads to

the formation of thin rutile layers at the metal/oxide interface even at temperature low as 350 °C.^[68]

It is important to note however, that annealing can affect the structure of the as-anodized TNTs. The growth of crystallites in the tube walls can lead to a slight decrease in the diameter and length of the tubes and an increase in the wall thickness, thus also affecting the inter-tubular space. Moreover, the nanostructured TiO₂ is thermodynamically metastable and is prone to solid state sintering at higher temperatures. This can lead to grain growth, densification, and an increase in the tube wall thickness. Since sintering is an activated process involving mass transfer process, a higher annealing temperature and/or prolonged annealing process favour more sintering, which can lead to complete destruction of the TNT structures. Generally, the higher the temperature and/or the time, the lower the nanotube resistance. By consequence, also the ramping speed of temperature can have a significant effect on the growth and transition of the crystal phase of TNTs. Moreover, annealing at higher temperatures leads to the formation of barrier layer between the tubes and the underlying Ti substrate.^[68]

Generally, the geometrical shape of the nanotubes can be maintained up to 650°C. At temperatures above that, the structural decay of the nanostructures can be observed. Some studies report that up to 500°C, in air, there is no change on the general morphology of the nanotubes. Above 600°C, some reports state that the annealing performed in air resulted in the collapse of nanotube bundles, while others state that only a decrease in lateral spacing was observed. This could be explained by differences in either annealing time, temperature ramp or even on the parameters of the anodization process.^[65] In organic electrolytes, with high amount of carbon in the inner tube wall, a double-walled nanotube structure can be formed.^[68]

Lastly, the thermal treatment, due to recrystallization process, can affect the chemical composition of the as anodized nanotubular layers. The as formed nanotubes typically contain a significant amount of fluoride and carbon species incorporated into TNTs, which are typically released, at least partially.^[69]

1.3.4.4 Wettability

The wettability or hydrophobicity of a surface can be affected by many factors including roughness and chemical composition. It is well established that native, as-formed TiO₂ is partially hydroxylated and therefore, has a polar nature, which leads to relatively small advancing contact angles, thus being hydrophobic. However, the as-anodized TNT's possess a hydrophilic nature, which is attributed to the capillary effect of the nanotubes. Simply, the water droplet is sucked quickly into the pores of the tubes

causing a dramatic reduction of the contact angle when compared with non-anodized Ti. A comparison of the wettability of nanotubes with different diameters (30, 50 ,70, and 100 nm) showed a reduction of the contact angle with the increase in diameter.^[69]

The crystalline phase of the TNTs can also influence their wettability. Both amorphous and annealed TNTs exhibit an hydrophilic nature. The hydrophilic behaviour of amorphous TNT can be attributed to the density of hydroxyl groups on their surface and the high polarity of the Ti-O-Ti bond. The surface hydroxyl can easily combine with the water molecule, thus, formed hydrogen bond resulting in good wettability. Up to a annealing temperature of 450°C, the TNT surface is super hydrophilic, when the annealing temperature was further increased, the hydrophilic nature started to decrease, due to the lack of the hydroxyl group on the surface of TNT after annealing above 450°C.^[68]

1.4 Bibliography

1. Hallab NJ, Jacobs JJ. Orthopedic Applications. In: Ratner BD, Hoffman AS, Schoen FJ, et al. (eds.). *Biomaterials Science: An Introduction to Materials*. 3rd ed. Chicago: Elsevier, 2013, 841–82.
2. Global Orthopaedic Implants Market outlook. *Expert Mark Res* 2021;1.
3. Briggs AM, Woolf AD, Dreinhofer K et al. Reducing the global burden of musculoskeletal conditions. *Bull World Heal Organ* 2018;**1**:366–8.
4. Branemark PI, Breine U, JOHANSSON B et al. Regeneration of Bone Marrow: a clinical and experimental study following removal of bone marrow by cutterage. *Acta Anat* 1964;**59**:1–46.
5. Chen Q, Thouas GA. Metallic implant biomaterials. *Mater Sci Eng R Reports* 2015;**87**:1–57.
6. Venable CS, Stuck WG, Beach A. The effects of bone of the presence of metals; based upon electrolysis. *Ann Surg* 1937;**105**:917–38.
7. Navarro M, Michiardi A, Castaño O et al. Biomaterials in orthopaedics. *J R Soc Interface* 2008;**5**:1137–58.
8. Geetha M, Singh AK, Asokamani R et al. Ti based biomaterials, the ultimate choice for orthopaedic implants-A review. *Prog Mater Sci* 2009;**54**:397–425.
9. Peters M, Hemptenmacher J, Kumpfert J et al. Structure and Properties of Titanium and Titanium alloys. In: Leyens C, Peters M (eds.). *Titanium and Titanium Alloys*. 1st ed. Weinheim: Wiley-VCH Verlag, 2003, 1–35.
10. Balamurugan A, Rajeswari S, Balossier G et al. Corrosion aspects of metallic implants - An overview. *Mater Corros* 2008;**59**:855–69.
11. Breme J, Eisenhart E, Biehl V. Titanium and its Alloys for Medical Applications. In: Leyens C, Peters M (eds.). *Titanium and Titanium Alloys*. 1st ed. Weinheim: Wiley-VCH Verlag, 2003, 423–49.
12. Huiskes R, Weinans H, Rietbergen B. The Relationship Between Stress Shielding and Bone Resorption Around Total Hip Stems and the Effects of Flexible Materials. *Clin Orthop Relat Res* 1991;**274**:124–34.
13. Sáenz De Viteri V, Fuentes E. Titanium and Titanium Alloys as Biomaterials. In: Jurgen Gegner (ed.). *Tribology - Fundamentals and Avancements*. 1st ed. Rijeka: InTech Open, 2013, 155–81.
14. Manivasagam G, Dhinasekaran D, Rajamanickam A. Biomedical Implants: Corrosion and its Prevention-A Review. *Recent Patents Corros Sci* 2010;**2**:40–54.
15. Leyens C, Peters M. Non-Aerospace Applications of Titanium and Titanium Alloys. In: Leyens C, Peters M (eds.). *Titanium and Titanium Alloys*. 1st ed. Koln: Wiley-VCH, 2003, 393–509.
16. Gilbert JL, Kubacki GW. Oxidative Stress, Inflammation, and the Corrosion of Metallic Biomaterials: Corrosion Causes Biology and Biology Causes Corrosion. In: Arndt D, Dziubla T (eds.). 1st ed. Oxford: Elsevier Academic Press.
17. Gotman I. Characteristics of metals used in implants. *J Endourol* 1997;**11**:383–9.
18. Nag S, Banerjee R. Fundamentals of Medical Implant Materials. *ASM Handb* 2012;**23**:6–17.
19. Niinomi M, Nakai M, Hieda J. Development of new metallic alloys for biomedical applications.

Acta Biomater 2012;**8**:3888–903.

20. Amarnath G, Muddugangadhar B, Tripathi S *et al.* Biomaterials for Dental Implants: An Overview. *Int J Oral Implantol Clin Res* 2011;**2**:13–24.

21. Bauer S, Schmuki P, von der Mark K *et al.* Engineering biocompatible implant surfaces: Part I: Materials and surfaces. *Prog Mater Sci* 2013;**58**:261–326.

22. Mavrogenis AF, Dimitriou R, Parvizi J *et al.* Biology of implant osseointegration. *J Musculoskelet Neuronal Interact* 2009;**9**:61–71.

23. Vroman L. Effect of adsorbed proteins on the wettability of hydrophilic and hydrophobic solids. *Nature* 1962;**196**:476–7.

24. Horbett TA. The Role of Adsorbed Proteins in Tissue Response to Biomaterials. In: Ratner BD, Hoffman AS, Schoen FJ, *et al.* (eds.). *Biomaterials Science: An Introduction to Materials*. 2nd ed. Oxford: Elsevier Academic Press, 2004, 237–46.

25. Mariani E, Lisignoli G, Borzì RM *et al.* Biomaterials: Foreign bodies or tuners for the immune response? *Int J Mol Sci* 2019;**20**, DOI: 10.3390/ijms20030636.

26. Silva-Bermudez P, Rodil SE. An overview of protein adsorption on metal oxide coatings for biomedical implants. *Surf Coatings Technol* 2013;**233**:147–58.

27. Anderson JM, Cook G, Costerton B *et al.* Host Reactions to Biomaterials and Their Evaluation. In: Ratner BD, Hoffman AS, Schoen FJ, *et al.* (eds.). *Biomaterials Science: An Introduction to Materials*. 2nd ed. Oxford: Elsevier Academic Press, 2004, 293–345.

28. Zhou G, Groth T. Host Responses to Biomaterials and Anti-Inflammatory Design—a Brief Review. *Macromol Biosci* 2018;**18**:1–15.

29. Amengual-Peñafiel L, Brañes-Aroca M, Marchesani-Carrasco F *et al.* Coupling between Osseointegration and Mechanotransduction to Maintain Foreign Body Equilibrium in the Long-Term: A Comprehensive Overview. *J Clin Med* 2019;**8**:139.

30. Sadowska JM, Ginebra MP. Inflammation and biomaterials: Role of the immune response in bone regeneration by inorganic scaffolds. *J Mater Chem B* 2020;**8**:9404–27.

31. Anderson JM. Biological Responses to Biomaterials. *Annu Rev Mater Res* 2001;**31**:81–110.

32. Ramazanoglu M, Oshida Y. Osseointegration and Bioscience of Implant Surfaces-Current Concepts at Bone-Implant Interface. In: Turkyilmaz I (ed.). *Implant Dentistry - A Rapidly Evolving Practice*. 1st ed. Rije: InTech, 2011, 57–82.

33. Anselme K. Osteoblast adhesion on biomaterials. *Biomaterials* 2000;**21**:667–81.

34. Trindade R, Albrektsson T, Tengvall P *et al.* Foreign Body Reaction to Biomaterials: On Mechanisms for Buildup and Breakdown of Osseointegration. *Clin Implant Dent Relat Res* 2016;**18**:192–203.

35. Trindade R, Albrektsson T, Galli S *et al.* Osseointegration and foreign body reaction: Titanium implants activate the immune system and suppress bone resorption during the first 4 weeks after implantation. *Clin Implant Dent Relat Res* 2018;**20**:82–91.

36. Pirisi L, Pennestrì F, Viganò M *et al.* Prevalence and burden of orthopaedic implantable-device infections in Italy: A hospital-based national study. *BMC Infect Dis* 2020;**20**:1–11.

37. Kapadia BH, Berg RA, Daley JA *et al.* Periprosthetic joint infection. *Lancet* 2016;**387**:386–94.

38. Kapadia BH, Mcelroy MJ, Issa K *et al.* The Economic Impact of Periprosthetic Infections Following Total Knee Arthroplasty at a Specialized Tertiary-Care Center. *J Arthroplasty* 2014;**29**:929–32.
39. Moraes MN, Silveira WC da, Teixeira LEM *et al.* Mechanisms of bacterial adhesion to biomaterials. *Rev Médica Minas Gerais* 2013;**23**:99–104.
40. Arciola CR, Campoccia D, Montanaro L. Implant infections: Adhesion, biofilm formation and immune evasion. *Nat Rev Microbiol* 2018;**16**:397–409.
41. Donlan RM, Costerton JW. Biofilms: Survival mechanisms of clinically relevant microorganisms. *Clin Microbiol Rev* 2002;**15**:167–93.
42. Trampuz A, Zimmerli W. Prosthetic joint infections: Update in diagnosis and treatment. *Swiss Med Wkly* 2005;**135**:243–51.
43. Gristina AG. Biomaterial-Centered Infection: Microbial Adhesion Versus Tissue Integration. *J Geophys Res* 1981;**7**:34.
44. Civantos A, Martínez-Campos E, Ramos V *et al.* Titanium Coatings and Surface Modifications: Toward Clinically Useful Bioactive Implants. *ACS Biomater Sci Eng* 2017;**3**:1245–61.
45. Romanò CL, Scarponi S, Gallazzi E *et al.* Antibacterial coating of implants in orthopaedics and trauma: A classification proposal in an evolving panorama. *J Orthop Surg Res* 2015;**10**:1–11.
46. Cloutier M, Mantovani D, Rosei F. Antibacterial Coatings: Challenges, Perspectives, and Opportunities. *Trends Biotechnol* 2015;**33**:637–52.
47. Milošev I. Surface Treatments of Titanium with Antibacterial Agents for Implant Applications. 2016:1–87.
48. Zhao L, Chu PK, Zhang Y *et al.* Antibacterial coatings on titanium implants. *J Biomed Mater Res - Part B Appl Biomater* 2009;**91**:470–80.
49. Ferraris S, Spriano S. Antibacterial titanium surfaces for medical implants. *Mater Sci Eng C* 2016;**61**:965–78.
50. Hake ME, Young H, Hak DJ *et al.* Local antibiotic therapy strategies in orthopaedic trauma: Practical tips and tricks and review of the literature. *Injury* 2015;**46**:1447–56.
51. Zasloff M. Antimicrobial peptides of multicellular organisms. *Nature* 2002;**415**:389–95.
52. Alves D, Olívia Pereira M. Mini-review: Antimicrobial peptides and enzymes as promising candidates to functionalize biomaterial surfaces. *Biofouling* 2014;**30**:483–99.
53. Holdbrook DA, Singh S, Choong YK *et al.* Influence of pH on the activity of thrombin-derived antimicrobial peptides. *Biochim Biophys Acta - Biomembr* 2018;**1860**:2374–84.
54. Lowe NM, Fraser WD, Jackson MJ. Is there a potential therapeutic value of copper and zinc for osteoporosis? *Proc Nutr Soc* 2002;**61**:181–5.
55. Lansdown ABG. A pharmacological and toxicological profile of silver as an antimicrobial agent in medical devices. *Adv Pharmacol Sci* 2010;**2010**, DOI: 10.1155/2010/910686.
56. Lansdown ABG. Silver in Health Care: Antimicrobial Effects and Safety in Use. *Curr Probl Dermatol Basel, Karger* 2006;**33**:17–34.
57. Vijayaraghavan R. Zinc oxide based Inorganic Antimicrobial agents. *Int J Sci Res* 2012;**01**:35–

46.

58. Gao C, Li C, Wang C *et al.* Advances in the induction of osteogenesis by zinc surface modification based on titanium alloy substrates for medical implants. *J Alloys Compd* 2017;**726**:1072–84.

59. Lemire JA, Harrison JJ, Turner RJ. Antimicrobial activity of metals: mechanisms, molecular targets and applications. *Nat Rev J Microbiol* 2013;**11**, DOI: 10.1038/nrmicro3028.

60. Brammer KS, Frandsen CJ, Jin S. TiO₂ nanotubes for bone regeneration. *Trends Biotechnol* 2012;**30**:315–22.

61. Tan AW, Pingguan-Murphy B, Ahmad R *et al.* Review of titania nanotubes: Fabrication and cellular response. *Ceram Int* 2012;**38**:4421–35.

62. Jäger M, Jennissen HP, Dittrich F *et al.* Antimicrobial and osseointegration properties of nanostructured titanium orthopaedic implants. *Materials (Basel)* 2017;**10**:1–28.

63. Ehrlich PJ, Lanyon LE. Mechanical strain and bone cell function: A review. *Osteoporos Int* 2002;**13**:688–700.

64. Peng Z, Ni J, Zheng K *et al.* Dual effects and mechanism of TiO₂ nanotube arrays in reducing bacterial colonization and enhancing C3H10T1/2 cell adhesion. *Int J Nanomedicine* 2013;**8**:3093–105.

65. Kunrath MF, Hubler R, Shinkai RSA *et al.* Application of TiO₂ Nanotubes as a Drug Delivery System for Biomedical Implants: A Critical Overview. *ChemistrySelect* 2018;**3**:11180–9.

66. Awad NK, Edwards SL, Morsi YS. A review of TiO₂ NTs on Ti metal: Electrochemical synthesis, functionalization and potential use as bone implants. *Mater Sci Eng C* 2017;**76**:1401–12.

67. Roy P, Berger S, Schmuki P. TiO₂ nanotubes: Synthesis and applications. *Angew Chemie - Int Ed* 2011;**50**:2904–39.

68. Indira K, Mudali UK, Nishimura T *et al.* A Review on TiO₂ Nanotubes: Influence of Anodization Parameters, Formation Mechanism, Properties, Corrosion Behavior, and Biomedical Applications. *J Bio- Tribo-Corrosion* 2015;**1**:1–22.

69. Kowalski D, Kim D, Schmuki P. TiO₂ nanotubes, nanochannels and mesosponge: Self-organized formation and applications. *Nano Today* 2013;**8**:235–64.

70. Zwilling V, Aucouturier M, Darque-Ceretti E. Anodic oxidation of titanium and TA6V alloy in chromic media. An electrochemical approach. *Electrochim Acta* 1999;**45**:921–9.

71. Zwilling V, Darque-Ceretti E, Boutry-Forwille A *et al.* Structure and growth of anodic oxide films on titanium and TA6V alloy. *Surf Interface Anal* 1999;**27**:629–37.

72. Grimes CA, Mor GK. Fabrication of TiO₂ nanotube arrays by electrochemical anodization: four synthesis generations. *TiO₂ Nanotube Arrays*. 1st ed. Pennsylvania: Springer International Publishing, 2009, 1–59.

73. Regonini D, Satka A, Jaroenworarluck A *et al.* Factors influencing surface morphology of anodized TiO₂ nanotubes. *Electrochim Acta* 2012;**74**:244–53.

74. Macák JM, Tsuchiya H, Schmuki P. High-aspect-ratio TiO₂ nanotubes by anodization of titanium. *Angew Chemie - Int Ed* 2005;**44**:2100–2.

75. Regonini D, Bowen CR, Jaroenworarluck A *et al.* A review of growth mechanism, structure and

- crystallinity of anodized TiO₂ nanotubes. *Mater Sci Eng R Reports* 2013;**74**:377–406.
76. Taveira L V., Macák JM, Tsuchiya H *et al.* Initiation and Growth of Self-Organized TiO₂ Nanotubes Anodically Formed in NH₄F/(NH₄)₂SO₄ Electrolytes. *J Electrochem Soc* 2005;**152**:B405.
77. Amsel G, Samuel D. The mechanism of anodic oxidation. *J Phys Chem Solids* 1962;**23**:1707–18.
78. Khalil N, Leach JSL. The anodic oxidation of valve metals-I. Determination of ionic transport numbers by α -spectrometry. *Electrochim Acta* 1986;**31**:1279–85.
79. LeClere DJ, Velota A, Skeldon P *et al.* Tracer Investigation of Pore Formation in Anodic Titania. *J Electrochem Soc* 2008;**155**:C487.
80. Yasuda K, Macak JM, Berger S *et al.* Mechanistic Aspects of the Self-Organization Process for Oxide Nanotube Formation on Valve Metals. *J Electrochem Soc* 2007;**154**:C472.
81. Beranek R, Hildebrand H, Schmuki P. Self-Organized Porous Titanium Oxide Prepared in H₂SO₄/HF Electrolytes. *Electrochem Solid-State Lett* 2003;**6**:B12.
82. Garcia-Vergara SJ, Habazaki H, Skeldon P *et al.* Formation of porous anodic alumina at high current efficiency. *Nanotechnology* 2007;**18**:1–8.
83. Berger S, Albu SP, Schmidt-Stein F *et al.* The origin for tubular growth of TiO₂ nanotubes: A fluoride rich layer between tube-walls. *Surf Sci* 2011;**605**:L57–60.
84. Berger S, Tsuchiya H, Schmuki P. Transition from Nanopores to Nanotubes: Self-ordered Anodic Oxide Structures on Titanium-Aluminides. *J Biomed Mater Res, Part A* 1997;**144**:47.
85. Robinson Aguirre O, Félix Echeverría E. Effects of fluoride source on the characteristics of titanium dioxide nanotubes. *Appl Surf Sci* 2018;**445**:308–19.
86. Macak JM, Tsuchiya H, Taveira L *et al.* Smooth anodic TiO₂ nanotubes. *Angew Chemie - Int Ed* 2005;**44**:7463–5.
87. Guo Z, Li X, Zhang X *et al.* Controlled morphology modulation of anodic TiO₂ nanotubes via changing the composition of organic electrolytes. *Phys Chem Chem Phys* 2014;**16**:11502–8.
88. Lee K, Kim J, Kim H *et al.* Effect of electrolyte conductivity on the formation of a nanotubular TiO₂ photoanode for a dye-sensitized solar cell. *J Korean Phys Soc* 2009;**54**:1027–31.
89. Yoriya S. Effect of inter-electrode spacing on electrolyte properties and morphologies of anodic TiO₂ nanotube array films. *Int J Electrochem Sci* 2012;**7**:9454–64.
90. Zhang W, Liu Y, Guo F *et al.* Kinetic analysis of the anodic growth of TiO₂ nanotubes: Effects of voltage and temperature. *J Mater Chem C* 2019;**7**:14098–108.
91. Seçkin E, Ürgen M. A kinetic model for determining morphology transitions and growth kinetics of titania nanotubes during anodization of titanium in ethylene glycol based electrolytes. *Surf Coatings Technol* 2021;**409**:126840.
92. Nasirpour F, Yousefi I, Moslehifard E *et al.* Tuning surface morphology and crystallinity of anodic TiO₂ nanotubes and their response to biomimetic bone growth for implant applications. *Surf Coatings Technol* 2017;**315**:163–71.
93. Lai CW, Sreekantan S. Photoelectrochemical Performance of Smooth TiO₂ Nanotube Arrays: Effect of Anodization Temperature and Cleaning Methods. *Int J Photoenergy* 2012;**2012**:1–11.

94. Indira K, Ningshen S, Mudali UK *et al.* Effect of anodization temperature on the surface morphology of anodized titanium. *Thin Film Nanomater* 2011;63–6.
95. Allam NK, Grimes CA. Effect of cathode material on the morphology and photoelectrochemical properties of vertically oriented TiO₂ nanotube arrays. *Sol Energy Mater Sol Cells* 2008;**92**:1468–75.
96. Sreekantan S, Khairul A, Saharudin Z *et al.* Formation of TiO₂ nanotubes via anodization and potential applications for photocatalysts, biomedical materials, and photoelectrochemical cell. *IOP Conf. Ser.:Materials Science and Engineering*. Vol 21. 2011, 1–18.
97. Sopha H, Tesar K, Knotek P *et al.* TiO₂ nanotubes grown on Ti substrates with different microstructure. *Mater Res Bull* 2018;**103**:197–204.
98. Fan R, Wan J. Electrode distance regulates the anodic growth of titanium dioxide (TiO₂) nanotubes. *Nanotechnology* 2017;**28**:1–5.
99. Regonini D, Clemens FJ. Anodized TiO₂ nanotubes: Effect of anodizing time on film length, morphology and photoelectrochemical properties. *Mater Lett* 2015;**142**:97–101.
100. Ozkan S, Nguyen NT, Mazare A *et al.* Fast growth of TiO₂ nanotube arrays with controlled tube spacing based on a self-ordering process at two different scales. *Electrochem commun* 2017;**77**:98–102.
101. Krbal M, Sopha H, Pohl D *et al.* Self-organized TiO₂ nanotubes grown on Ti substrates with different crystallographic preferential orientations: Local structure of TiO₂ nanotubes vs. photoelectrochemical response. *Electrochim Acta* 2018;**264**:393–9.
102. İzmir M, Ercan B. Anodization of titanium alloys for orthopedic applications. *Front Chem Sci Eng* 2019;**13**:28–45.
103. Macak JM, Tsuchiya H, Taveira L *et al.* Self-organized nanotubular oxide layers on Ti-6Al-7Nb and Ti-6Al-4V formed by anodization in NH₄F solutions. *J Biomed Mater Res - Part A* 2005;**75**:928–33.
104. Filova E, Fojt J, Kryslova M *et al.* The diameter of nanotubes formed on Ti-6Al-4V alloy controls the adhesion and differentiation of Saos-2 cells. *Int J Nanomedicine* 2015;**10**:7145–63.
105. Li Y, Ding D, Ning C *et al.* Thermal stability and in vitro bioactivity of Ti-Al-V-O nanostructures fabricated on Ti6Al4V alloy. *Nanotechnology* 2009;**20**, DOI: 10.1088/0957-4484/20/6/065708.
106. Jordanovová V, Losertová M, Štencek M *et al.* Microstructure and properties of nanostructured coating on Ti6Al4V. *Materials (Basel)* 2020;**13**:1–11.

2 RESEARCH LAYOUT AND EXPERIMENTAL PROTOCOL

2.1 Research layout

The purpose of this research project is the development and characterization of a multifunctional surface modification system to be applied in medical grade Ti alloys, namely Cp-Ti (ASTM grade 2) and Ti6Al4V (ASTM grade 5), used for orthopaedic implants. A general scheme representing all the steps and main research activities is pictured in Figure 2-1. The main aim is to decrease the infection risk without hindering the native biocompatibility of the material or the corrosion resistance of the Ti alloys. To this aim TiO₂ nanotubes have been produced through electrochemical anodization on the Ti alloys surfaces and later functionalized with inorganic antimicrobial agents, namely, silver (Ag), zinc (Zn) and copper (Cu), which were deposited using electrochemical methods. Thus, the research activity was divided into three distinct parts. A first part (see chapter 4) focused on the production and characterization of TiO₂ nanotubes through electrochemical anodization, process definition and optimization in order to achieve a specific target morphology. A second part (see chapter 5) focused on the study of the effect of post-anodization heat-treatments on the crystallinity of the produced oxide, and the corrosion resistance. The third part (see chapter 6) focused on antimicrobial functionalization of the nanotubular layers through electroless deposition of silver or electrodeposition of either copper and zinc into the nanotubular layers, followed by biocompatibility tests.

2.2 Surface preparation

Due to the different hardness and ductility of the metal substrates, the surface preparation process was optimized individually for each. Polishing was conducted on an automated polisher Meetkon, Forcipol 300 1V. The samples were fixated in an epoxy resin support in order to be placed in the automatic polisher. In general, the process consisted of several grinding steps using different grades of SiC grinding papers and water, followed by a polishing step in cloth using a silica suspension (OP-S NonDry silica suspension 0.25, STRUERS with 25% H₂O₂). To optimize the process, the following parameters have been taken into consideration: SiC papers grades, time and applied force

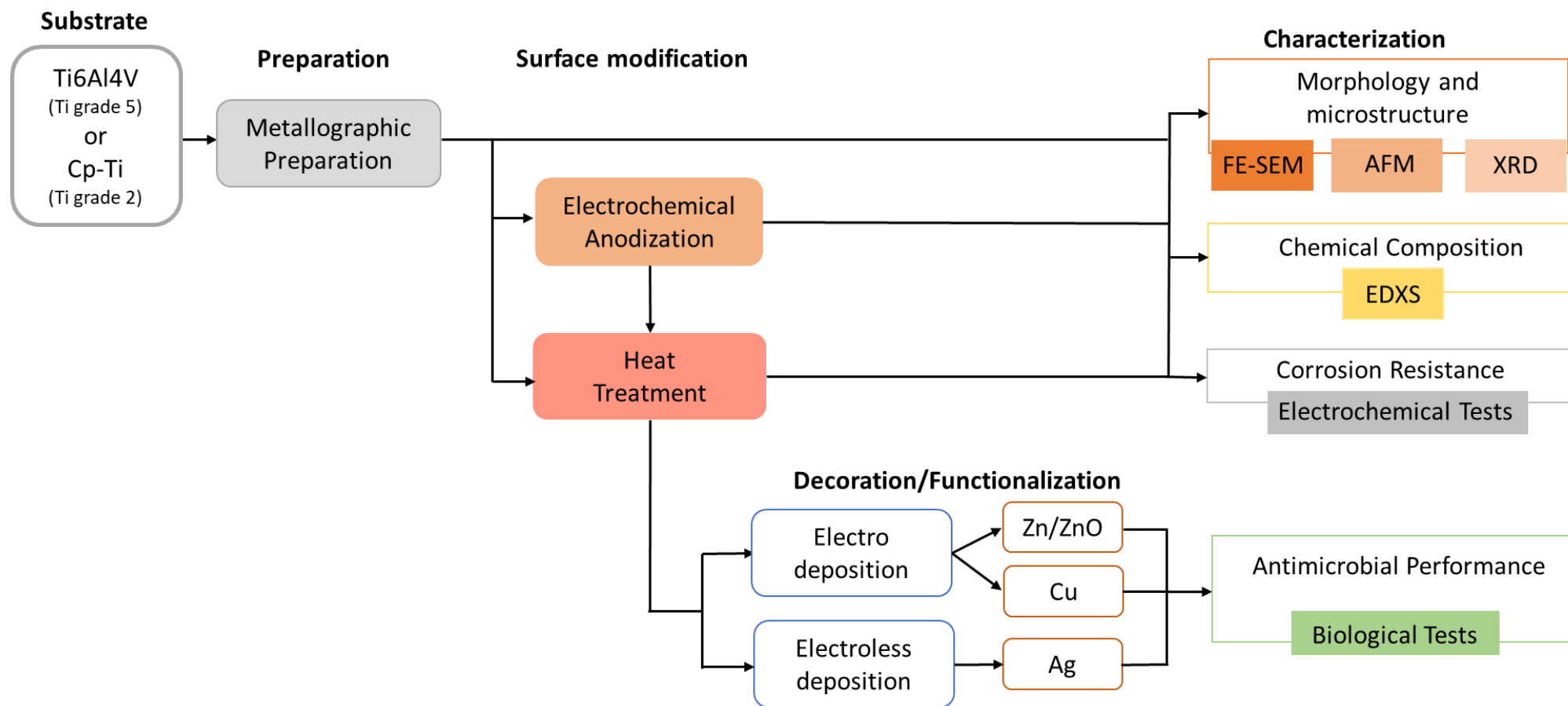


Figure 2-1 – General scheme of the research phases and tests conducted for the development of TiO₂ nanotube antibacterial coating.

for each step, plate and head speed for each step. In table 1 are reported the optimized polishing parameters for each substrate. After polishing, the samples taken out of their support and cleaned using water and soap and then ultrasonically cleaned for 5 min in ethanol, acetone and DI water, sequentially, to remove all residuals from the polishing procedure. FESEM was used to check the polishing quality (JEOL model JSM-7610Fplus).

Table 2-1: Optimized procedure parameters for grinding and polishing of Ti grade 2 and Ti grade 5 substrates.

Ti gr. 2				
Mean	Head speed (rpm)	Plate speed (rpm)	Applied individual force (N)	Time (min)
Paper 500grit	100	300	10	1
Paper 1200grit	100	300	10	1
Cloth + SiO ₂ colloidal suspension (75%) + H ₂ O ₂ -30%wt (25%)	75	150	12	45
Ti gr. 5				
Paper 800grit	100	300	20	5
Paper 1200grit	100	300	20	5
Paper 200grit	100	300	20	5
Paper 400grit	100	300	20	5
Cloth + SiO ₂ colloidal suspension(75%) + H ₂ O ₂ -30%wt (25%)	75	150	15	20

2.3 Microstructural characterization of the Ti alloys

The microstructural characterization of the base alloys has been performed by FESEM observation of polished samples, both prior and after metallographic etching. Kroll's etchant (2%v/v HNO₃ (68%), 1%v/v HF (48%)) was used to evidence their microstructure. The optimized etching time was of 30s for Ti grade 2 and 15s for Ti grade 5. The chemical composition, and their phases, of the alloys was determined through EDXS analysis (Oxford X-MAX20 energy dispersive X-ray spectrometer). Identification of crystalline phases was achieved through XRD analysis. The X-ray diffraction (XRD) patterns were collected through a Philips PW3040/60 X'pert PRO diffractometer (equipped with an X'celerator detector) operated at 40 kV and 40 mA, using Ni-filtered Cu K α radiation in

the 2θ range of 10° - 120° with a step size of 0.02° and a counting time of 40 s per step. For the identification of the Bragg's peaks in the obtained diffractograms, the available data software database was used. In the following tables (Table 2-2 and 2-3) are reported the more common diffraction angles (2θ) and the relative intensity (the percentage with respect to the peak of maximum intensity). In this case for the substrate, are reported the listed (2θ , maximum intensity) of several databases for the two main phases of Ti, the hexagonal closed packed α -phase and the body centered cubic β -phase.

Table 2-2: Characteristic diffraction angles (2θ) and the relative intensity (%) for common Bragg's peaks of α -phase of Ti alloys.

Ti α -phase			
Internal Database		External Database	
2θ [$^\circ$]	I [%]	2θ [$^\circ$]	I [%]
35.10	25.00	35.13	25.37
38.42	30.00	38.42	25.66
40.17	100.00	40.20	100.00
53.01	13.00	53.03	12.99
62.95	11.00	63.02	13.78
70.66	11.00	70.69	13.51
74.16	1.00	74.24	1.89
76.22	9.00	76.28	13.73
77.37	6.00	77.44	9.78
82.29	1.00	82.30	1.78
86.76	1.00	86.85	2.28

Table 2-3: Characteristic diffraction angles (2θ) and the relative intensity (%) for common Bragg's peaks of β -phase of Ti alloys.

Ti β -phase			
Internal Database		External Database	
2θ [$^\circ$]	I [%]	2θ [$^\circ$]	I [%]
38.48	100.00	38.50	100.00
55.54	12.00	55.59	14.33
69.61	17.00	69.65	24.87
82.45	4.00	82.52	6.93

2.4 Electrochemical anodization

Anodic oxidation of polished samples was carried out in a two-electrode setup using a DC power supply. A platinum plate was used as cathode and the Ti disks were used as anode. Both cathode and anode had an exposed circular area with a diameter of 2 cm and were kept at a distance of 2 cm from each other. The electrolyte used was an ethylene glycol non-aqueous solution containing 0.5 wt.% NH_4F and 2.5 vol% DI H_2O (represented by the abbreviation EtOH+ NH_4F), which was kept at room temperature. For optimization of the anodization process three parameters have been taken into consideration: the applied potential difference, the anodization time and electrolyte ageing. The combination of parameters tested for the two types of alloys is reported in table 2-4. After anodization, the samples were rinsed with DI H_2O , ultrasonically clean in acetone for 5 min and air dried.

Table 2-4: Anodization process parameters tested for the two alloys.

		Time (h)					
		0.5	1	2	3	6	9
Applied potential difference (V)	20	●	●●	●	●	●	●
	40	●	●●	●	●	●	●
	60	●	●●	●	●	●	●
	80	●	●●	●	●	●	●
	100	●	●	●			
● - Ti grade 5 ● – Ti grade 2							

In order to understand the influence of microstructure on the anodization of Ti grade 5, additional very short anodizations were conducted for 25, 40, 120, 300 and 900 seconds.

A custom-made anodization cell was designed to provide a sufficient electrolyte quantity for the anodization process, while also ensuring both a specific distance between the anode and the cathode and a defined exposed surface area, of both cathode and anode, to the electrolyte. It was constructed using polycarbonate plates bound together by a bicomponent epoxy resin. These materials were chosen due to their resistance to degradation by F^- ions. The cell design is reported in Figure 2-2. A CSI 12001X power supply was used (maximum voltage: 120 V; I_{max} 1 A), in order to provide current and a potential difference between cathode and anode.

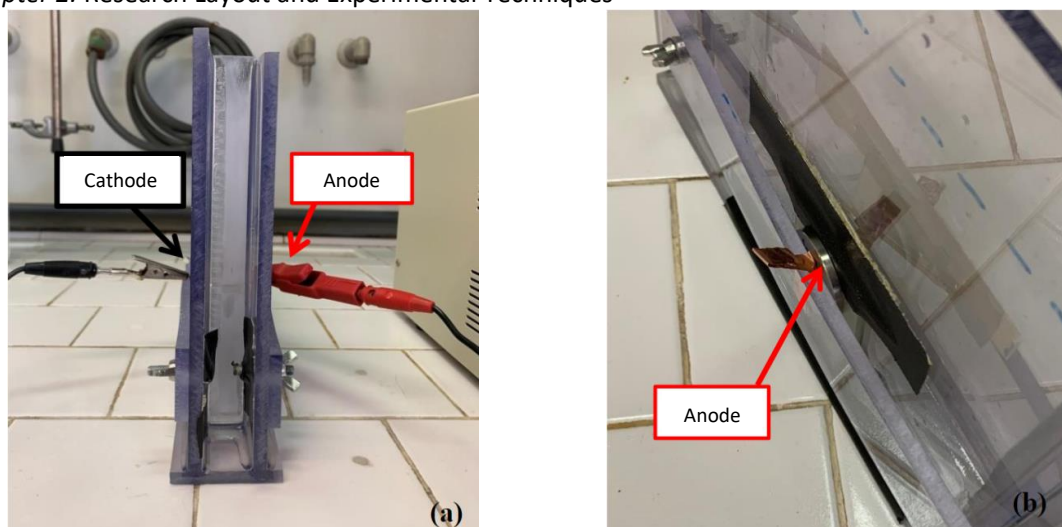


Figure 2-2: Anodization cell with indication of anode and cathode (a), detail of the mounting system of the anode (b).

2.5 Surface analysis and morphology characterization of the produced TNTs

The morphology of the samples was characterized through FESEM, and the chemical composition through EDXS. FESEM micrographs were captured in the middle region of the anodized area using a secondary electrons in-lens detector. In order to characterize the nanotube layer in cross-section, the anodized samples were cut, hot-embedded in epoxy-resin and polished to a mirror-like surface. AFM topographic and Volta potential maps have been obtained using a Digital Instruments Nanoscope IIIa Multimode with a n-type doped silicon pyramid single-crystal tip coated with PtIr5 (SCM-Pit probe). The surface maps were captured in a dual-scan mode. In the first scan, topography data was obtained in tapping mode, and in the second scan, the surface potential was determined by lifting the tip 100 nm. The measurements were performed in air atmosphere, at room temperature and an approximate relative humidity of 28%, at a scan frequency rate of 0.2 Hz, pixel resolution of 512×512 and zero-bias voltage. XRD measurements have been performed on selected anodized specimens of both alloys, both prior and after heat treatments using the same protocol described in section 2.1.2. In tables 2-5 and 2-6, are reported the more common diffraction angles (2θ) and the relative intensity (the percentage with respect to the peak of maximum intensity) for the crystalline phases of anatase and rutile, respectively, for TiO_2 .

Table 2-5: Characteristic diffraction angles (2θ) and the relative intensity (%) for common Bragg's peaks of anatase phase of TiO_2 .

Anatase			
Internal Database		External Database	
2θ [°]	I [%]	2θ [°]	I [%]
25.34	100.00	25.33	100.00
36.98	2.10	36.98	6.32
37.81	5.90	37.82	20.47
38.61	11.00	38.6	7.17
48.10	19.30	48.08	28.85
53.92	10.30	53.93	18.58
55.14	14.10	55.12	18.21
62.18	1.10	62.17	3.07
62.75	3.9	62.75	14.36
68.81	8.40	68.82	6.39
70.39	4.00	70.36	7.10
75.17	5.20	75.12	11.03
76.15	1.90	76.12	2.96
82.78	1.50	82.76	5.64
83.28	1.80	83.25	2.12

Table 2-6: Characteristic diffraction angles (2θ) and the relative intensity (%) for common Bragg's peaks of rutile phase of TiO_2 .

Rutile			
Internal Database		External Database	
2θ [°]	I [%]	2θ [°]	I [%]
27.44	100.00	27.46	100.00
36.08	42.00	36.11	45.47
39.20	6.50	39.22	6.70
41.24	16.10	41.27	19.05
44.05	5.80	44.08	6.81
54.33	43.80	54.37	57.49
56.64	12.60	56.68	17.25
62.75	5.70	62.81	8.23
64.06	5.80	64.11	8.24
69.01	13.70	69.07	20.87
69.80	6.70	69.87	10.17
72.43	0.70	72.49	1.20
76.54	1.40	76.61	2.14
79.83	0.70	79.91	1.28
82.35	2.60	82.32	4.34
84.27	1.70	84.33	3.08
87.97	0.60	87.57	1.14
89.55	3.80	89.64	7.59

2.6 Evaluation of corrosion resistance

The corrosion resistance of selected anodized and anodized and heat-treated specimens has been evaluated using potentiodynamic polarization (PDP) measurements performed at room temperature. The electrolyte used was phosphate buffered saline solution (PBS), prepared from analytic reagents (all reagents were purchased from Sigma-Aldrich) and DI water, in accordance with the ASTM standard F2129/1219 standard: NaCl (8 g.l^{-1}), KCl (0.2 g.l^{-1}), Na_2HPO_4 (1.15 g.l^{-1}) and KH_2PO_4 (0.2 g.l^{-1}). NaCl from Merck, and all other reagents from Sigma-Aldrich. The pH of the solution was maintained at 7.4 ± 1 . The apparatus for electrochemical measurements consisted of a conventional three-electrode cell, with Ag/AgCl/ $\text{KCl}_{3\text{M}}$ (+222 mV vs standard hydrogen electrode - SHE) as the reference electrode and a Pt wire as the counter electrode, with a computer controlled potentiostat (AUTOLAB PGSTAT 30) with research corrosion software (Nova, from Metrohm Autolab). All electrochemical measurements were performed after 1 h immersion in the electrolyte, in order to stabilize the open-circuit potential (OCP) and reach the steady state condition. The PDP measurements were carried out with a scan rate of 0.2 mVs^{-1} from cathodic to anodic potentials, and a scan range from -0.2 V vs OCP until reaching 0.001 A/cm^2 .

2.7 Antimicrobial decoration/functionalization

Ag, Cu and Zn were evaluated as antimicrobial agents to be deposited on the surface of TNTs heat treated in air at 500°C for 3h. After deposition, the morphology of deposited Ag, Zn and Cu has been evaluated through FESEM and the chemical composition through EDXS. The EDXS analyses have been performed on the top surface of the decorated nanotubes in a $10 \times 10 \mu\text{m}$ area. EDXS has been used only for comparison as the analyses performed under these conditions cannot give quantitative results.

2.7.1 Electrodeposition of Zn and Cu.

The decoration of TNTs with Zn/ZnO or Cu nanoparticles (ZnNPs or CuNPs) was achieved through an electrochemical deposition process. A three-electrode system was used with an Ag/AgCl as reference electrode and Pt wire as counter electrode. A 3.2 mM $\text{Zn}(\text{NO}_3)_2$ solution was used for the deposition of Zn and cyclic voltammetry was used to identify the deposition potential. To optimize the process different deposition times (1, 3, 10 and 15 min) and different temperatures (room temperature or 70°C) have been tested. The effect of ultrasounds during the deposition was also evaluated.

A 3.2mM CuSO₄ aqueous solution, acidified at pH 2 with H₂SO₄ was used for the deposition of Cu. Also, in this case cyclic voltammetry was used to identify the deposition potential. Different attempts have been made -0.6 V, -0.8 V and -1 V vs. Ag/AgCl at room temperature. For further optimization, the process was carried also at different times (5 s, 12 s, 180 s and 360 s), under sonication or not.

TiO₂ nanotubes decorated with Zn or Cu are represented as TNTs-Zn or TNTs-Cu, respectively.

2.7.2 Electroless deposition of Ag

Silver decoration was achieved using an electroless plating process based on the work of S-D Kim *et al.*^[1], in which a silver amine complex was reduced by glucose. The silver amine complex solution was prepared by adding silver nitrate (to a final concentration of 2.25 wt.%, Sigma-Aldrich) to 60 ml DI water and potassium hydroxide (to a final concentration of 0.53 wt.% KOH, TitolChimica) until a fine brown precipitate of Ag₂O is formed. To this solution different amounts of ammonium hydroxide (NH₄OH, Sigma Aldrich) were added, under stirring, to form silver amine complex ([Ag(NH₃)₂]⁺). For process optimization, this solution was also filtrated in some tests, prior the deposition. A reducing solution was prepared adding glucose to 20 ml of DI water to a final concentration of 1 wt.%. The heat-treated sample were mounted in poly(methyl methacrylate) supports, and immersed in silver amine complex solution and incubated, for various amount of times (10, 15 and 20 min), and under different conditions of stirring (magnetic stirring or ultrasounds), for process optimization. Immediately after, the samples were transferred to the reducing solution, hand agitated until the dark-brown heat treated TNT samples turned black (which signals the reduction of silver complex on the surface). In order to optimize the process, reductions were performed both at room temperature or at 8° C. The samples were then collected, rinsed with DI water, and ultrasonically cleaned in DI water. TiO₂ nanotubes decorated with Ag and henceforth represented as TNTs-Ag.

2.8 Antimicrobial tests

Prior to the tests, the samples were first defatted and cleaned in acetone (10 min, twice), washed 3 times with type 1 water, and dried with an argon stream. Then, the samples were sterilized in an ethanol (70%) bath (15 min, twice), rinsed 3 times with sterile type 1 water and dried with an argon stream in a sterile environment. They were

transferred into a 24-well plate (Sarstedt, Ltd. Newton, MA, USA) and stored in a desiccator for further tests.

2.8.1 Bacterial strain and growth media

Reference strain from the American Type Culture Collection *S. epidermidis* (ATCC 35984), was maintained in stock at -80°C. Before the experiments, bacterial cells were grown overnight on tryptic soy agar (TSA) at 37°C. Afterwards, the bacteria were scraped out from the agar medium into a liquid medium (Mueller Hinton Broth) and grown, overnight, at 37°C. The resulting suspension was then diluted into a proper density in either sterile PBS (ASTM F2129/1219 standard) for Cu and Zn in section 2.8.1 or Müller Hinton Broth for Ag in section 2.8.2, right before the experiments.

2.8.2 Antimicrobial activity evaluation of TNTs-Zn and TNTs-Cu

Antimicrobial activity was evaluated by adding 500 µl of bacterial suspension (2×10^5 CFU/mL) in PBS, to each sample. After 2h incubation, at 37°C under agitation at 150 rpm, the content of the wells, containing bacteria in suspension, was collected (supernatant) and serial dilutions of 1:10 (up to 10^{-3}) were made and plated in TSA plates for determination of antimicrobial activity. The samples in the well were washed three times with sterile PBS, transferred to 5 mL STARSTEDT tubes containing 500 µl of 0.5% Tween 80 in PBS and placed on ice. Then, in sequence, the samples were submitted to ultrasounds at 160 W for 15 min, vortexed for 5 min, and submitted again to ultrasounds at 160 W for 15 min, to remove the adhered bacteria from the samples. Between each step, the tubes were placed on ice. The 500 µl of 0.5% Tween 80 in PBS was then collected, and serially diluted (1:10, up to 10^{-3}) and plated in TSA plates, in order to quantify adherent bacteria. All TSA plates were incubated overnight at 37°C. Finally, the number of viable bacterial colonies were counted to appraise antimicrobial performance based on equation 1:

$$(1) R(\%) = \frac{B}{A} \times 100\%$$

where R indicates the relative antibacterial viability, A is the average number of viable bacterial colonies from the control sample (as-polished Ti6Al4V) and B is the average number of viable colonies for a specific functionalized sample.

2.8.3 Antimicrobial activity evaluation for TNTs-Ag

Antimicrobial activity of TNTs-Ag was assessed through the same procedure described in section 2.7.2. However, a bacterial suspension with an adjusted concentration of 2×10^5 CFU/ml, in Müller Hinton Broth (instead of sterile PBS) was used. Müller Hinton Broth was chosen instead of PBS since it has been described to increase bacterial cell viability when tested against antimicrobial agents^[2], and silver is widely known for its excellent antimicrobial properties which exceed those of Zn and Cu.^[3] Thus, for the purpose of this project, this assay allowed to better understand the antimicrobial potential of silver.

2.9 Bicompatibility assays

Commercially available MG63 human osteoblast-like cells were cultured in dulbecco's modified eagle medium (Gibco) supplemented with 10% (v/v) heat inactivated FBS (Euroclone, Italy), 2mM L-glutamine (Sigma-Aldrich, USA), 100 units/mL penicillin(Sigma-Aldrich, USA) and 100 µg/mL of streptomycin (Sigma-Aldrich, USA), at 37°C in a humidified atmosphere of 5% CO₂ and 95% air. The growth media was changed every 2 days. The cells were washed with PBS and isolated from the culture flask through trypsinization (0.25% trypsin-EDTA), suspended in fresh culture media, and used to assess the bone cell viability on bare Ti6Al4V, TNTs produced on Ti grade 5, as well as Ag-decorated TNTs. Prior to these assays, the samples were defatted and sterilized as described in section 2.7. In order to assess the cytotoxicity of the samples, the cells were seeded at a density of 4×10^5 cells/well, and incubated for 6h, at 37°C in a humidified atmosphere of 5% CO₂ and 95% air. Negative controls were assigned to cells cultured in fresh media without samples. Then the culture media were collected, and 300 µl of sterile PBS containing 15% of lysis solution was added to each well to promote cell lysis. Cytotoxicity was assessed by measuring the amount of lactate dehydrogenase release by the cells according to manufacturer's instructions (CyQuant™ LDH Cytotoxicity Assay, Invitrogen).

2.10 Bibliography

1. Kim SD, Choe WG, Jeong JR. Environmentally friendly electroless plating for Ag/TiO₂-coated core-shell magnetic particles using ultrasonic treatment. *Ultrason Sonochem* 2013;**20**:1456–62.
2. De Leersnyder I, De Gelder L, Van Driessche I *et al.* Influence of growth media components on the antibacterial effect of silver ions on *Bacillus subtilis* in a liquid growth medium. *Sci Rep* 2018;**8**, DOI: 10.1038/s41598-018-27540-9.
3. Lemire JA, Harrison JJ, Turner RJ. Antimicrobial activity of metals: mechanisms, molecular targets and applications. *Nat Rev | Microbiol* 2013;**11**, DOI: 10.1038/nrmicro3028.

3 MICROSTRUCTURAL CHARACTERIZATION OF THE TI ALLOYS

This first part of the research work was focused on the microstructural characterization of the metal substrates. Two commercially available medical grade Ti alloys, namely, Ti grade 2 ASTM F67 alloy (Titanium International Group, SRL, Bologna, Italy) and Ti grade 5 ASTM F1472 alloy (ATI Europe Distribution – Allegheny Technologies GmbH, Remscheid, Germany) were used. The Ti grade 2 alloy had a chemical composition (wt. %) of 0.052 Fe, 0.145 O, 0.005 C, 0.003 N, 0.0009 H and Ti (balance). The Ti grade 5 alloy had a chemical composition (wt.%) of 6.25 Al, 0.065 C, 0.23 Fe, 0.003 H, 0.01 N, 0.185 O, 4.45 V, 0.001 Y and Ti (balance).

3.1 Microstructure of Ti grade 2

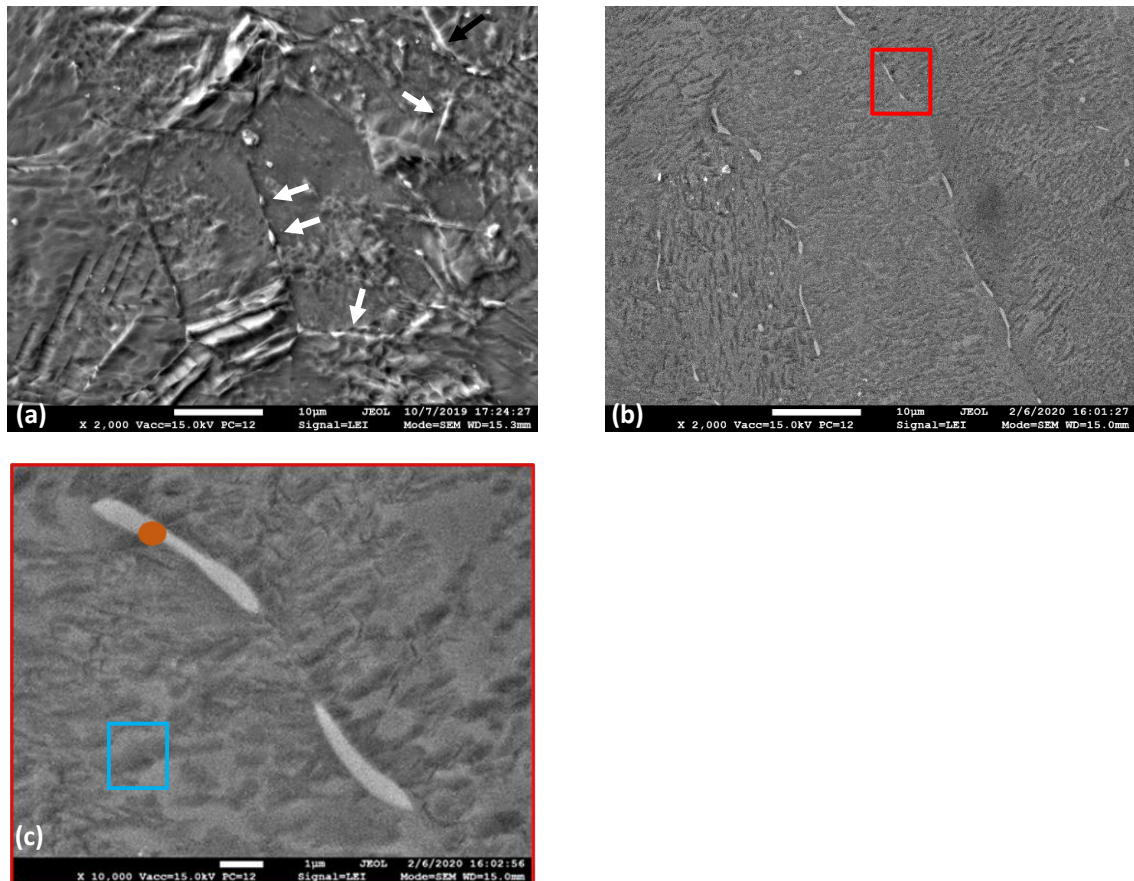


Figure 3-1: FESEM micrographs depicting a top view of bare Ti grade 2 samples. a) secondary electrons micrograph of the etched sample, b) backscattered electrons micrograph of a polished sample, c) detail of figure b (red frame), with a blue frame and orange dot indicating areas analyzed through EDXS (Table 3-1).

Figure 3-1a shows a FESEM micrograph of the Ti grade 2 alloy after metallographic etching in Kroll's solution (see section 2.1.2). It is possible to observe that the alloy consists of elongated grains whose dimensions vary from 15 to 50 μm . Some intermetallic particles aligned along the grain boundaries are also observed (white arrows Fig. 3-1a). FESEM micrographs in backscattered mode of non-etched samples better show these particles consisting of heavier elements (Fig. 3-1b and c). The EDXS analysis performed on the bigger grains and on the intermetallic particle of Fig. 3-1 c are reported on table 3-1. The EDXS analysis revealed the presence of higher concentrations of Fe and small amounts of Cr and Ni on these intermetallic particles. In Figure 3-2, the XRD diffractogram of the Ti grade 2 alloy is reported. All peaks identified are attributed to the closed-packed hexagonal α -phase. The amount of β -phase grains is too low to be detected by the XRD technique.

Table 3-1 – Results of EDXS analysis in the areas highlighted in Fig. 3-1 c).

Element		Blue	Orange
Ti	Wt.%	96.07	86.1
O	Wt.%	3.93	4.57
Cr	Wt.%		0.71
Fe	Wt.%		7.92
Ni	Wt.%		0.7
Total	Wt.%	100.0	100.0

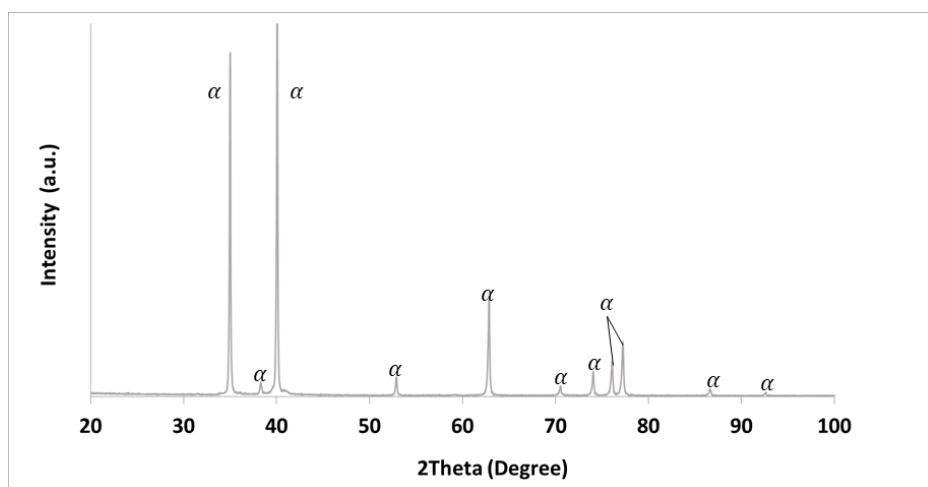


Figure 3-2: XRD spectrum of Ti grade 2.

3.2 Microstructure of Ti grade 5

Figure 3-3 shows FESEM micrographs of the Ti6Al4V samples polished in backscattered mode (Fig. 3-3 a) and after metallographic etching in Kroll's solution for 15s (Fig. 3-3 b). The Ti6Al4V samples presented a polycrystalline structure with grains of different sizes. EDXS analysis on the different areas (Table 3-2) identified, as the α -phase, the darker areas of Fig. 3-2 a (richer in Al), while the elongated brighter grains, which presented a relatively higher concentration of V, were identified as β -phase grains. Following the metallographic etching, the two phases could be more clearly distinguished (Fig. 3-3 b) as the higher amount of V in the β -phase decreased the reactivity of the alloy to the etchant.

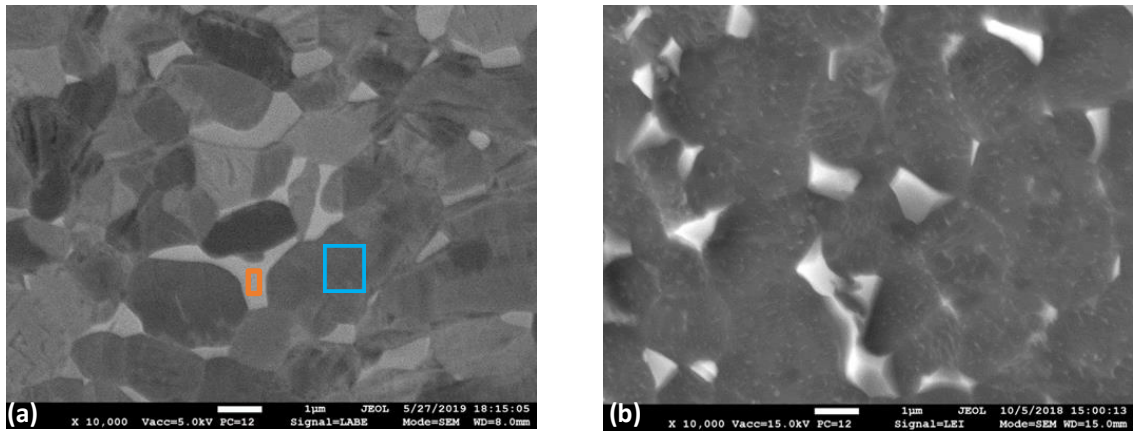


Figure 3-3: FESEM micrographs of the bare Ti6Al4V sample: a) BSE micrograph, b) SE micrograph after metallographic etching (Kroll's solution 15s). The blue and yellow shapes on represent the zones analyzed through EDXS, listed in table 4-2.

Table 3-2 – Average composition of the α and β phase of the Ti6Al4V alloy.

Element		alloy	Yellow	Blue
Ti	Wt.%	89.7	90.7	81.8
Al	Wt.%	6.4	6.5	4.8
V	Wt.%	3.9	2.6	13.4
Total	Wt.%	100.0	100.0	100.0

In Figure 3-4 are reported the AFM topographic and SKPFM Volta potential maps of a polished Ti6Al4V samples together with the line profiles. β -phase grains (see white arrows in Fig. 3-4 a) appeared slightly higher at the topographic map ($\approx 3\text{nm}$), possible due to the difference in hardness having an effect on the polishing procedure. The

different chemical composition between α -phase and β -phase was reflected in a difference of approximately 30 mV in the Volta potential (Fig. 3-4 b and c), with the β -phase exhibiting the higher values, in accordance with what was previously reported by other authors.^[1,2] Indeed, V had a higher working force (WFE), 4.3 eV, in comparison to Al, which had a WFE of 4.26 eV in the polycrystalline condition.^[3] The β -phase, which had a higher V content, had a higher relative surface potential and acted as a nobler phase than the α -phase which had a greater Al content.

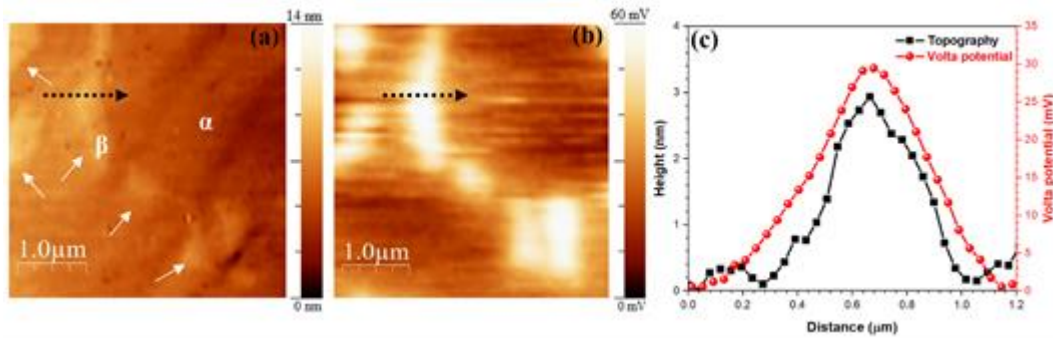


Figure 3-4: a) AFM topography and b) SKPFM Volta potential maps of polished Ti6Al4V alloy. c) line profiles along the black dashed arrow of a) and b).

Figure 3-5 shows the XRD patterns of Ti grade 5 alloy. The peaks corresponding to the hexagonal closed-packed α -phase and the body centered cubic β -phase have been identified.

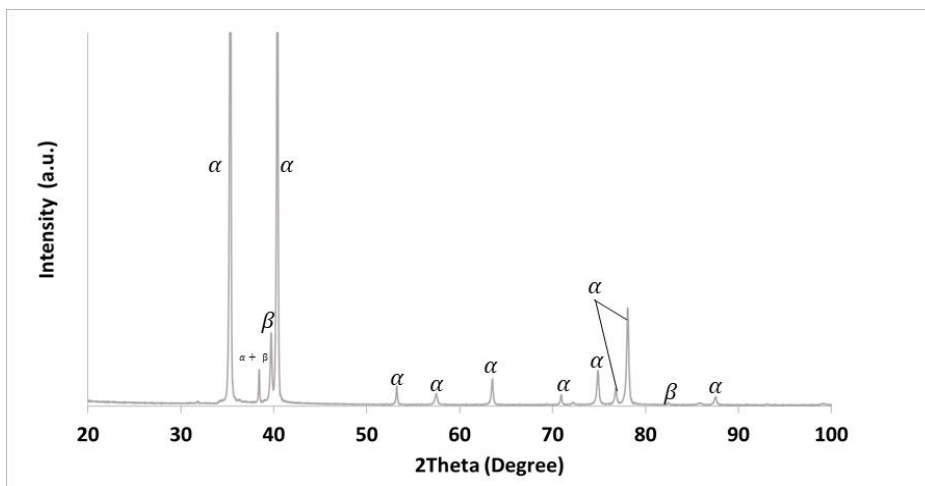


Figure 3-5: XRD spectrum of Ti grade 5.

3.3 Partial Conclusions

Ti grade 2 and Ti grade 5 alloys have been microstructurally characterized. Ti grade 2 is mainly composed by Ti with low amounts of Fe, Cr and Ni. It consists of a single α -phase hexagonal closed packed structures, as evidenced by the XRD analysis. The metallographic analysis revealed that it is composed by large elongated α -phase grains and small β -phase grains rich in Fe, which are located along the boundaries of the α -phase grains. On the other hand, the Ti grade 5 alloy presents a polycrystalline biphasic structure with grains of different sizes. It consists of an Al-rich hexagonal closed packed α -phase matrix which embeds smaller, V-rich body-centered cubic β -phase grains. The different chemical composition of the two phases is reflected on the Volta potential with the β -phase grains presenting an approximately 30 mV higher potential.

3.4 Bibliography

1. Robinson Aguirre O, Félix Echeverría E. Effects of fluoride source on the characteristics of titanium dioxide nanotubes. *Appl Surf Sci* 2018;**445**:308–19.
2. Rahimi E, Offoiach R, Baert K *et al.* Role of phosphate, calcium species and hydrogen peroxide on albumin protein adsorption on surface oxide of Ti6Al4V alloy. *Materialia* 2021;**15**, DOI: 10.1016/j.mtla.2020.100988.
3. Michaelson HB. The work function of the elements and its periodicity. *J Appl Phys* 1977;**48**:4729–33.

4 ELECTROCHEMICAL ANODIZATION OF TI ALLOYS

This chapter presents the results obtained for the production of TiO₂ nanotubes (TNTs) through electrochemical anodization on both Cp-Ti and Ti6Al4V alloy. The purpose was to achieve well-defined, vertically oriented TiO₂ nanotubular structures with a specific diameter range (70-100 nm). For this purpose, this work comprised the following activities:

- Testing of the influence of specific parameters on the growth and development of nanotubular structures, namely, the applied potential difference, time and electrolyte ageing.
- Detailed study of the growth process of TiO₂ nanotubes over Ti grade 5 alloy, by performing anodization for very short times.

The produced samples were analyzed through FESEM, EDXS and AFM/SKPFM.

4.1 Electrochemical anodization of Ti grade 2

4.1.1 Influence of electrolyte aging on TiO₂ nanotubes morphology

Prior to the study of the influence of applied voltage and time on the morphology of TNTs, the influence of the electrolyte ageing was studied to establish a usage time window, in which the results could be considered reproducible. In Figure 4-1 are listed FESEM micrographs of Ti grade 2 samples anodized, at the same applied potential differences (40 V) and time (4 h), for an electrolyte with increasing usage. The specimens anodized using a fresh electrolyte, present a great amount of nanograss on their surfaces. The amount of these structures is reduced by increasing the age of the electrolyte, being replaced at a certain point, by well-defined nanotubes with open tops and, if the aging is too extensive, by a compact, porous layer. Through these tests, this work established that, for the production of well-defined vertically oriented TNTs on Ti grade 2, the electrolyte should be aged at least 10 h before first use and should not be used more than 150 h of total time of anodization. It was under these conditions that all samples analysed in the following sections were produced.

The effect of electrolyte ageing on the formation of TiO₂ nanotubes has been extensively studied. In general, various works agree that the increasing usage of the electrolyte results in a lower overall conductivity, reduced concentrations of F⁻ in solution, accumulation of [TiF₆]²⁻ as well as a reduced concentration of NH₄⁺ ions due to

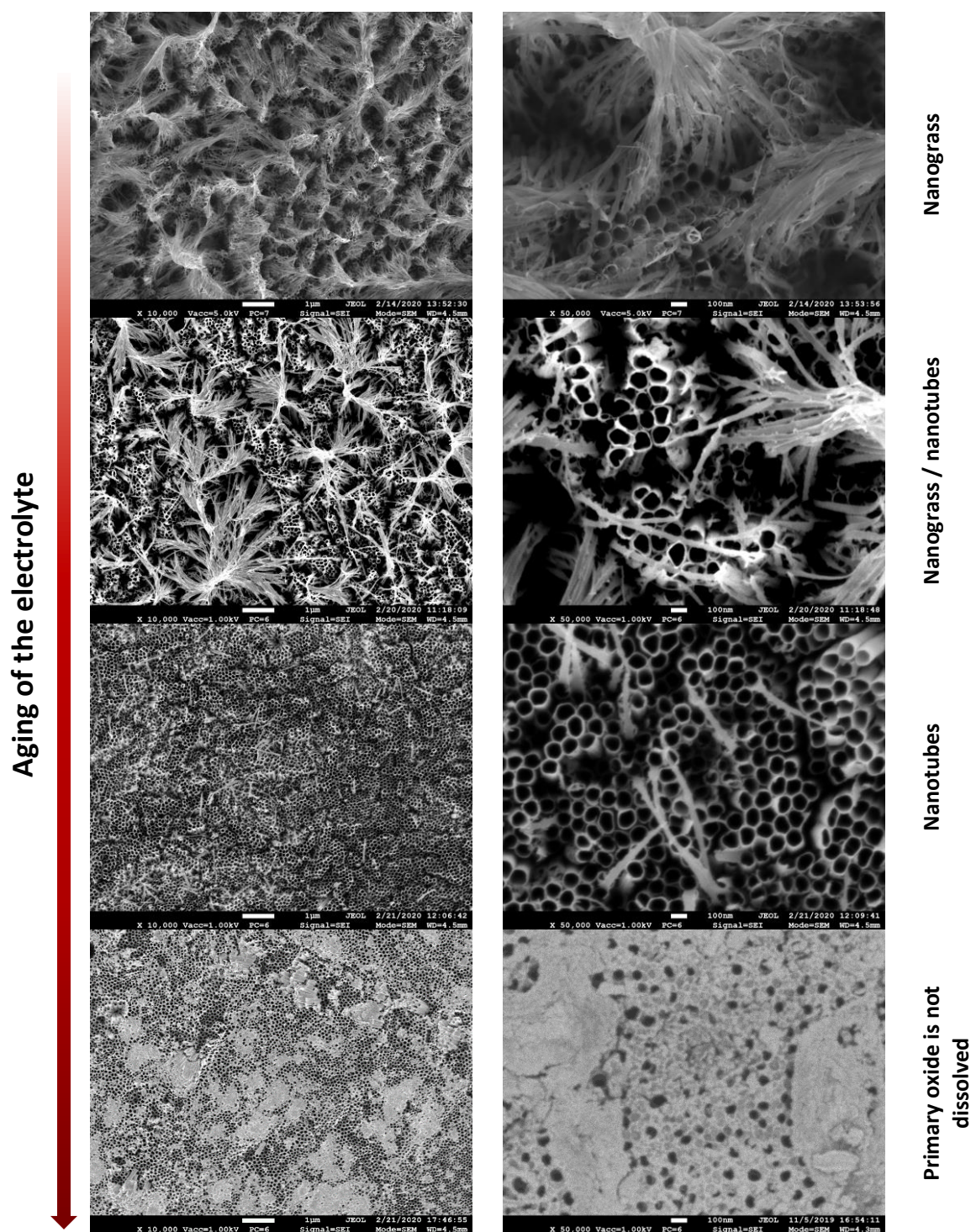


Figure 4-1: Morphology of the Ti grade 2 anodic oxide layer with regard to the time of use of the electrolyte.

formation of $(\text{NH}_4)_2\text{TiF}_6$ salt or volatile NH_3 .^[1–3] For this reason, some authors also report an increase in the pH of an $\text{EtOH} + \text{NH}_4\text{F}$ electrolyte, from a weak acid to an alkaline solution, due to formation of ammonia and electrolysis of water.^[1,2] However, not all

authors agree on these effects. Lee *et al.* [4], reported an increase in conductivity with electrolyte usage, but used an EtOH+HF electrolyte instead of NH₄F, which could explain the distinct reported results. An acidic pH mainly induces the formation of TiF₆²⁻ which is highly soluble in water, while a more alkaline pH could induce the formation of less soluble oxofluorides, that remain in the TiO₂ film. Suhadolnik *et al.* [1] detected lower amount of fluorides in the nanotubes produced after prior usage of the electrolyte, which seem to corroborate this theory. Another point of divergence is the variation in the water content. Suhadolnik reports an increase in the water content, while Gulati *et al.* [3] reported a decrease. This could be a result of the different conditions at which the anodization processes were performed. If the process is carried in air atmosphere, water concentration increases until saturation. If it is conducted in a controlled environment, without air humidity, such as a glove box, it decreases. [3] EtOH is a hygroscopic substance and as such it absorbs moisture from the air, until saturation. The results presented in this work support these findings. The transition, with increase electrolyte age, from a nanograin microstructure, which, according to Seçkin and Ürgen [5], is formed after extended dissolution of TiO₂ nanotubes, to first, nanotubes and then porous compact oxide, reveals a slower evolution of morphology due to a decrease in the oxide dissolution effect by the electrolyte. Thus, TNTs formation occurs at a slower growth rate. Moreover, Guo *et al.* [2], also report on the increasing inter-tubular distance with the age of the electrolyte, but that could not be confirmed in this work. In general, these results show that an aged electrolyte, with 10 to 150 h of prior utilization, resulted in higher tube morphology definition, at specific voltages. The same study was also performed on Ti grade 5 and anodization times between 1 h and 20 h should result in well-defined morphologies.

4.1.2 Morphology of TNTs grown on Ti grade 2

Figure 4-2 shows FESEM micrographs depicting a top view of Ti grade 2 samples, anodized for different applied potential and times, at low magnifications. From the low magnification micrographs, it is possible to see that a porous compact oxide, which covers the entirety of the analyzed area, was obtained for all samples anodized at 1h as well as the specimen anodized at 20 V for 3 h. On the other hand, the samples anodized at 40 and 60 V, for 3 h present different zones, some parts are still covered with the porous compact oxide, while on others open-mouth TNTs can be observed. A similar morphology was observed also on the samples anodized at 20 V for 3 h and 6 h.

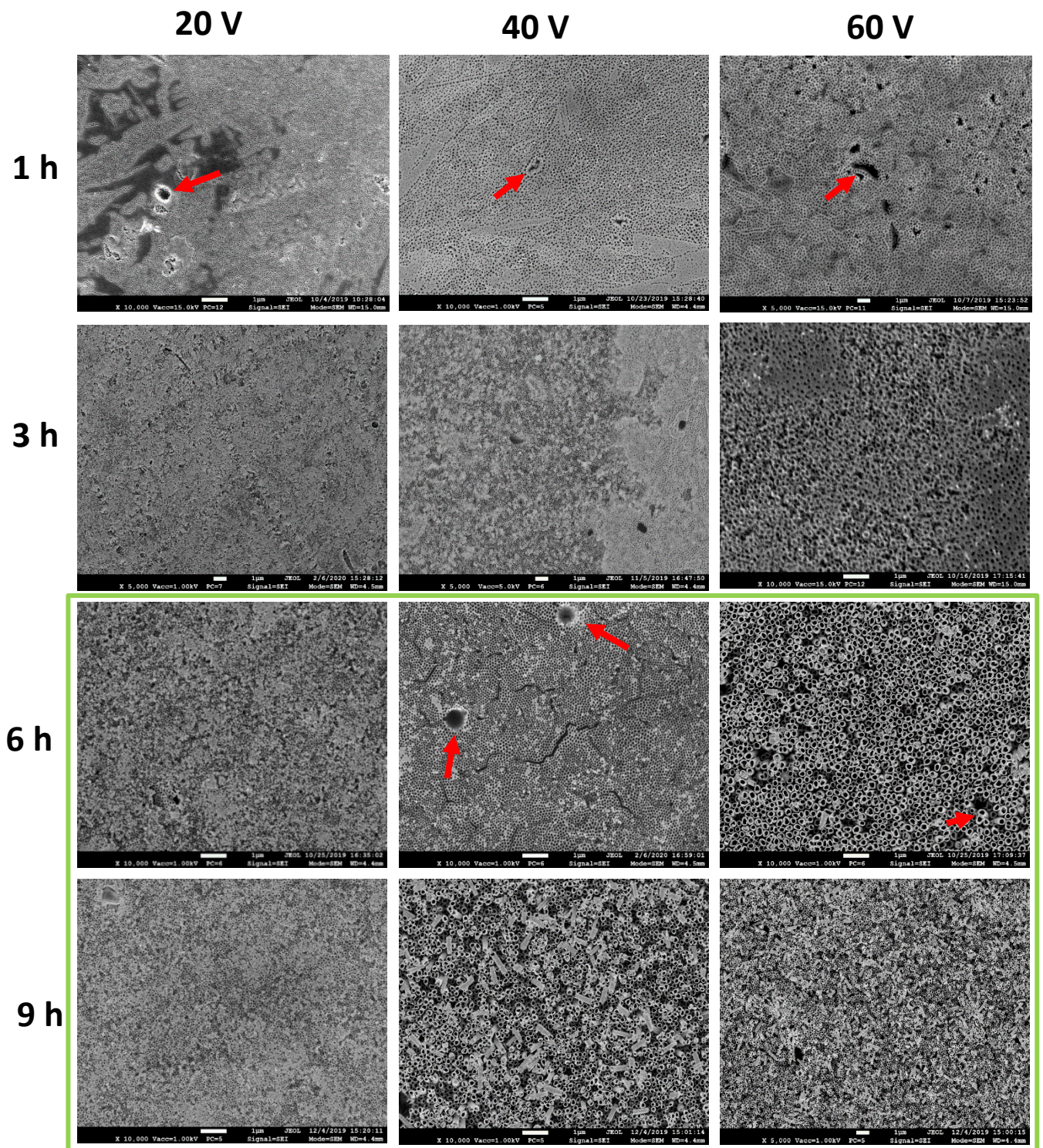


Figure 4-2: FESEM micrographs depicting a top view of the anodic oxide layer produced through electrochemical anodization in a Ti grade 2 substrate, at different applied potential and times. The green frame highlights the conditions with open-top nanotubes.

For all other conditions, namely, samples anodized for 40 V and 60 V for 6 and 9 h and at 20 V 9 h, defined nanotubes were obtained. However, the nanotubes produced at 40 and 60 V for 9 h, result partially fragmented. This could be due to the high length of the TNTs produced after 9 h of anodization, which can cause their fragmentation during the cleaning post-anodization procedures.

A further increase of the applied potential to 80 V led to the formation of a particular morphology (Fig. 4-3). Although the top surface is still covered by the compact porous layer (Fig. 4-3 a), in some areas this is delaminated revealing a nanograss structure under it (Fig. 4-3 b and c). To our knowledge the occurrence of nanograss below the compact oxide layer as not been reported previously. Furthermore, it is not in accordance with the model proposed by Seckin and Ürgen^[6], which considers that the formation of nanograss occurs due to continuous dissolution of tube walls after disappearance of the superficial compact oxide, a common view shared by other authors. In this case, it is reasonable to consider that the anodization time was not long enough to completely dissolve the compact porous layer, but the high applied voltage led to a fast growing of the TNTs underneath and an extensive thinning of their walls, which collapse forming nanograss. Thus, the compact porous oxide layer delaminates due to the loss of mechanical support.

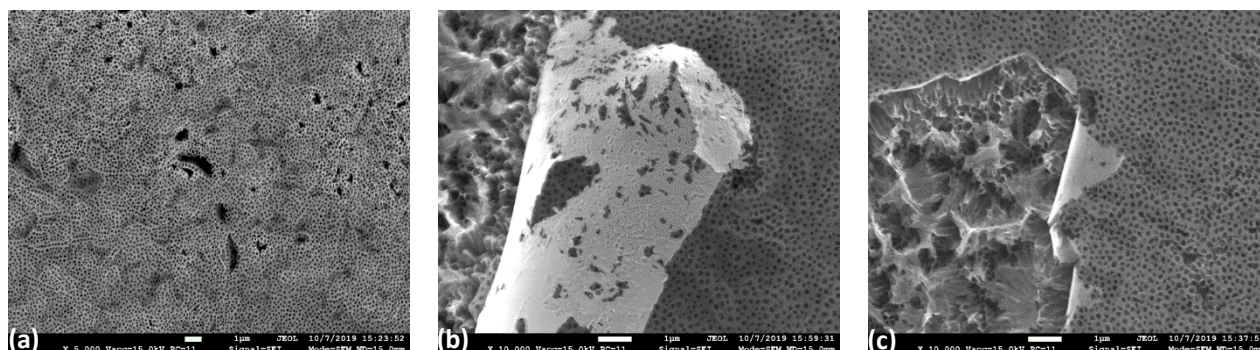


Figure 4-3: FESEM micrographs depicting a top view of the oxide layer produced on Ti grade 2 through electrochemical anodization at 80 V for 1 h: a) view of the porous compact oxide, b) and c) detail of the detachment of the porous compact oxide, revealing the underneath nanograss structure.

Moreover, some holes are noticed on the surface of all anodized samples, where the anodic oxide seem not to grow (red arrow, Fig. 4-2). Micrographs reporting in detail this phenomenon both on the top surface and in cross section are reported in Figure 4-4. The shape, size and distribution of these defects closely resembles those of the β -phase grains. EDXS analyses performed over these defects revealed the presence of Fe, confirming that they are formed over the β -phase grains.

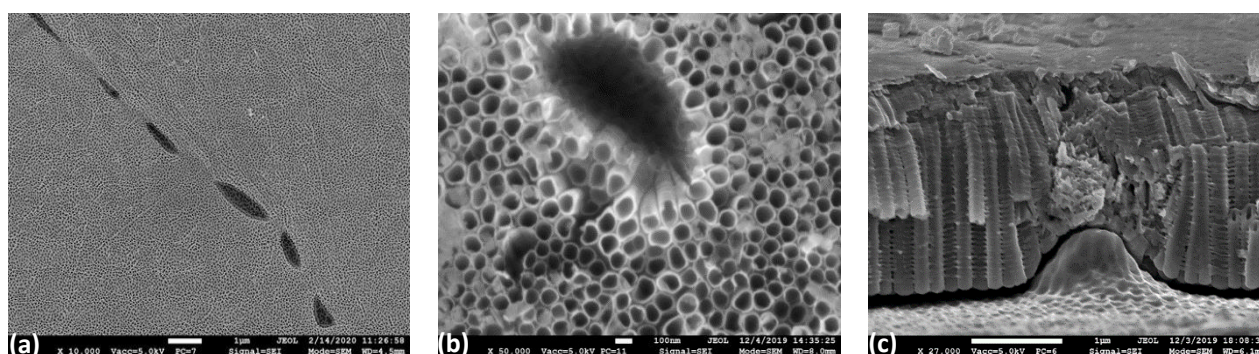


Figure 4-4: FESEM micrographs of the anodic oxide defects a) top surface morphology at low magnification, b) detail of a defect in top morphology and c) cross-section view.

The micrographs in cross section (Fig. 4-4 c) reveal that the β -phase presents a higher height, when compared to the α -phase, which points to its bigger resistance to dissolution in the electrolyte. Moreover, well-defined nanotubes are produced over the equiaxed α phase grains, while a sponge like, porous oxide seems to be produced over the β phase grains. As such, the composition of the substrate seems to influence the morphology of the produced oxide.

Higher magnification micrographs of the nanotubes top surface are reported in figure 4-5. The higher magnification micrographs allow to clearly distinguish the morphological differences of the produced nanotubes under different applied potential differences and anodization times. According to the model of morphological transition development of the anodic oxide, proposed by Seckin and Urgan^[5], the obtained results seem to show both stage 1 and stage 2 of nanotubular development, as well as the transition between the two stages. The effect of the time can be easily perceived in the increased dissolution of the barrier oxide layer. By increasing the time from 1 h to 9 h, at all applied potential differences, there is a transition from a compact barrier oxide (stage 1), first to tubes covered with remnants of that porous layer (various degrees of transition from stage 1 to stage 2) and then to well-defined, open nanotubes (stage 2). A similar effect, however in a smaller degree, is observed with the increase in potential from 20 to 60 V, especially for anodization times superior to 1 h. Moreover, the increase in the applied potential difference, at any given time, as well as the increase in time, for any given applied potential, leads to a marked increase in nanotube diameter. Thus, these results show that both time and the applied voltage result in an increased dissolution of the anodic oxide, albeit through different mechanisms. The applied potential difference directly determines the strength of the electric field and, thus, determines the ion migration rate and dissolution rate. On the other hand, the longer the time, the longer the dissolution.

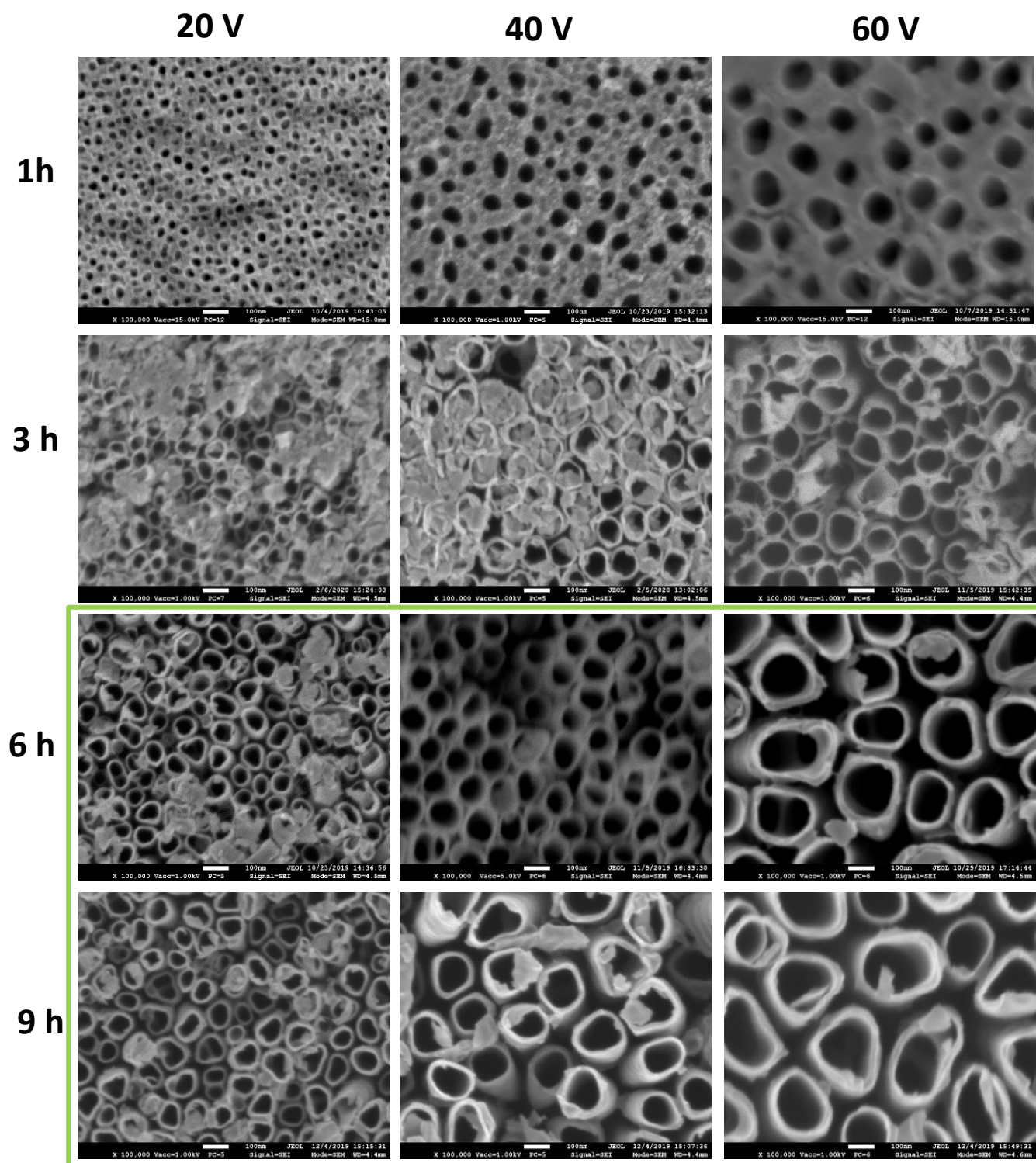


Figure 4-5: FESEM micrographs depicting a top view of the anodic oxide layer produced through electrochemical anodization in a Ti grade 2 substrate, at different applied potential and times, at higher magnification. The green frame highlights the conditions with open-tubular nanotubes.

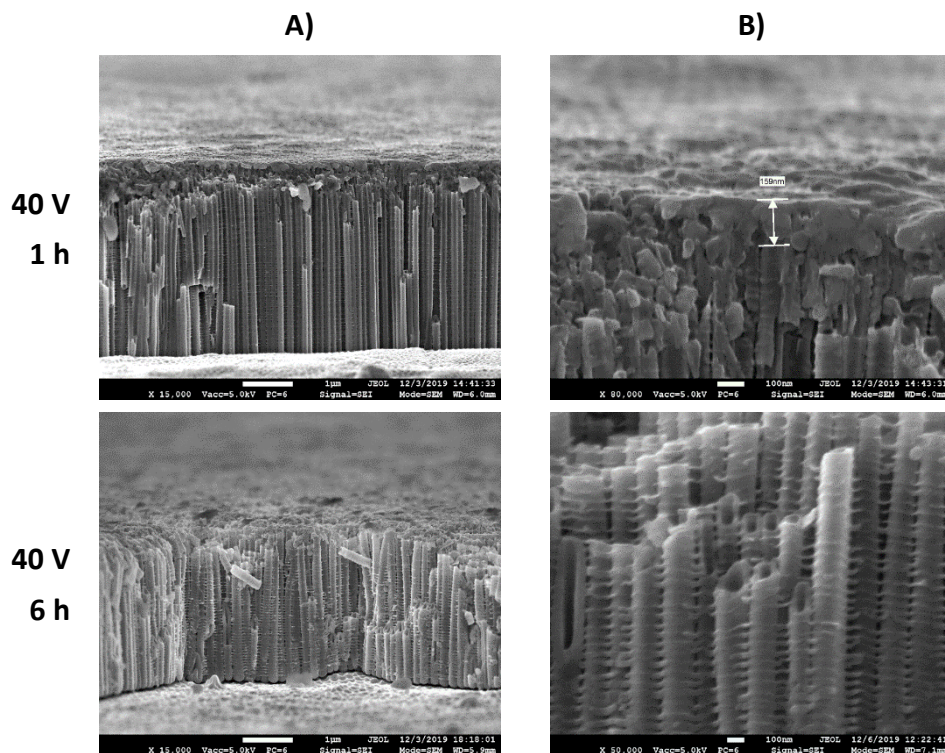


Figure 4-6: FESEM micrographs depicting the oxide layer produced on Ti gr.2 through electrochemical anodization at 40 V for various anodization times, in cross section. a) general view and b) detailed view of tube wall morphology.

Figure 4-6 shows FESEM micrographs that depict a cross section of nanotubes produced at 40 V for 1 h and 6 h. For all samples, tubular structures present side wall inhomogeneity with ripples along the tube wall (Fig. 4-6 a and b). In Figure 4-6 b), the tube tops are shown from a side view. For the 1 h sample, the primary oxide is visible covering the tube tops, with a thickness of 159 nm. However, no similar layer is observed for the samples produced at 6 h, which presents completely open tube tops (see Fig. 4-5). These results further confirm the dissolution effect of anodization time. The “ribbed” morphology of the tubular walls, which were observed in all these samples, is common in aqueous electrolytes, due to temporary local acidification at the pore tips that leads to an temporarily increased dissolution rate resulting in variation in the wall thickness.^[7,8] In organic electrolytes, however, the low water content usually prevents their formation but only if it remains below a specific threshold, which, according to Raja et al.^[9] is 0.5% wt.^[8] Thus, these results suggest that the water content in the aged electrolyte used in this work is above that threshold for Ti grade 2. The occurrence of ripples along the tube walls, in organic electrolytes, was attributed to the etching action of water over the TiF_4 rich-layer in between tubular walls, which enables transient formation of a TiO_2 film around the external part of the wall, during tube growth.^[10,11]

The average inner diameter of the tubes/pores are plotted in Figure 4-7. Overall, as it was already noticed in figure 4-2 and 4-5, these results show that there is an almost linear increase of the diameter with both the increase in the applied potential difference and the anodization time. For an applied potential difference of 20 V, the diameter was approximately 55 nm after 3 h, 60 nm after 6 h and 67 nm after 9 h. Similarly, at 40 V the diameter was of about 95 nm after 3 h, 108 nm after 6 h and 127 nm after 9 h; while at 60 V, the diameter of about 125 nm after 3 h, 158 nm after 6 h and 197 nm after 9 h. These values show that the variation of the inner diameter of the tubes is more pronounced with the variation of the applied potential difference than of time. Moreover, the effect of the increase of anodization time seems to be more pronounced at higher applied potentials.

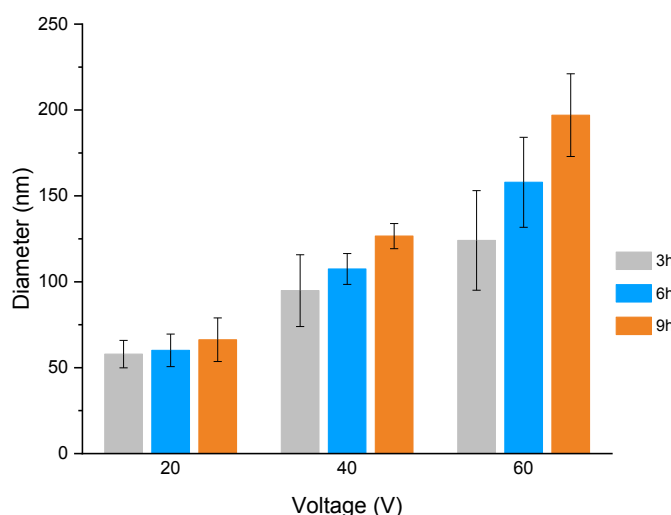


Figure4-7: Average inner diameter of TiO₂ nanotubes produced over Ti grade 2 as a function of the applied potential, for anodization times of 3 h, 6 h, and 9 h.

Pore diameter is closely related with pore nucleation during the initial stages of nanotube development. The applied potential difference will determine the strength of the applied electric field and, as such, the ion migration rate and the dissolution rate, for a specific electrolyte. As such, the effect of the applied potential difference over the tube diameter is well-known and similar results have been extensively reported by several authors for the anodization of Ti grade 2 in different electrolyte compositions, both aqueous or organic based.^[12–15] The effect of increasing time, on the other hand, is usually associated with the increasing length of the tubular structures as well as their morphological development, from pores to tubes, and to nanograss due to over dissolution. Regarding its influence over tube diameter, the effect is less investigated, with

some works presenting contradictory results. For instance, Chernozhen *et al.* ^[16] reports an increase in diameter when the anodization was extended from 30 min to 240 min (4 h). Brevian *et al.* ^[17], on the other hand, reported a decrease in the diameter, when increasing the anodization time from 60 to 240 min. The main difference between both works was the composition of the electrolyte.

4.2 Electrochemical Anodization of Ti grade 5

4.2.1 Morphology of TNTs grown on Ti grade 5

Figure 4-8, shows FESEM micrographs depicting a top view of Ti grade 5 samples anodized at different applied potentials and times. From the low magnification micrographs, it is clear that the anodic oxide is not uniform over the whole surface and presents large cavities whose shape, size and distribution closely resemble those of the β -phase grains (see section 3, Fig. 3-2). To further confirm this, EDXS analysis have been performed both inside and outside these cavities in a representative sample (anodized at 60 V 120 min), and the results reported in table 4-1 (the values listed are the mean values of 15 independent measurements), confirming a higher amount of V in the measurements inside the cavities, and higher amount of Al on the upper surface. Due to the difference in height between the two distinct zones, these results should be considered qualitative.

Focusing on the morphology of the oxide grown over the α -phase (α -oxide), the produced oxide is porous for all conditions but presents different morphologies for different voltages and times. These differences in morphology are a result of the increased dissolution effect of both time and voltage and represent different stages on the morphology evolution of the nanotubular layers.^[5] A porous compact oxide (stage 1) was obtained for the samples anodized at 40 V for 30 min (a compact, non-porous oxide was obtained for the sample anodized at 20 V for 30 min, which is not pictured). On the other hand, the samples anodized at 20 V for 60 and 120 min, 40 V for 60 min and 60 V for 30 min present only remnants of this porous oxide and it is possible to observe the presence of well-defined nanotubular structures on the areas where it is dissolved (transition from stage 1 to stage 2). Well-defined nanotubular layers (stage 2), with open tops, were obtained for the samples anodized at 40 V for 120 min, 60 V for 60 and 120 min, 80 V and 100 V for 30 and 60 min, while nanograss (stage 3) was obtained for 80 V and 100 V, after 120 min of anodization.

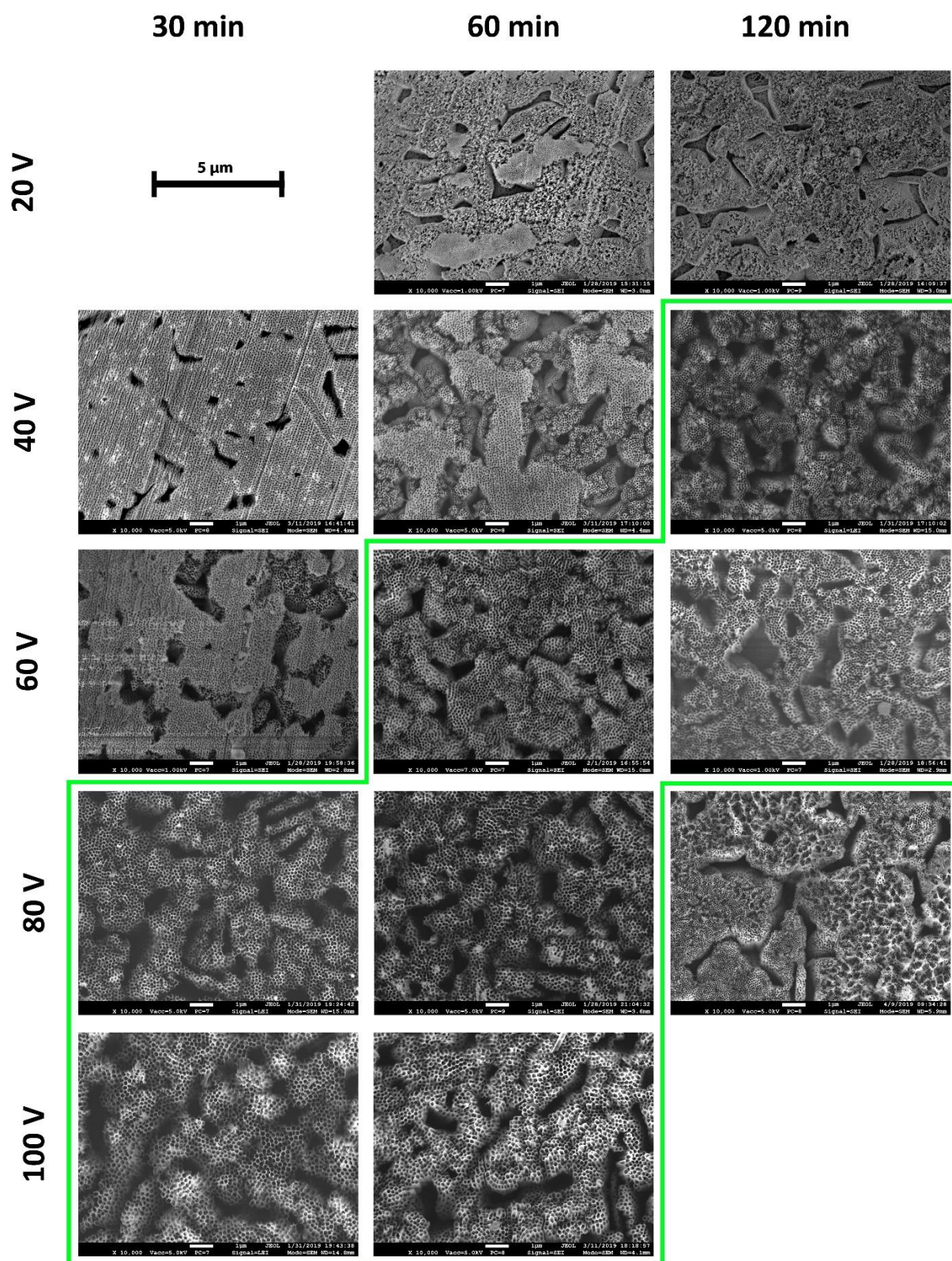


Figure 4-8: FESEM micrographs depicting a top view of the anodic oxide layer produced through electrochemical anodization in a Ti grade 5 substrate, at different applied potential and times. The green frame highlights the conditions with open-top nanotubes.

Thus, as observed previously for Ti grade 2 in section 4.1.2, by both increasing the applied potential and time, there is an increased dissolution effect of the electrolyte over the produced oxide, which translates first, in the transition from a non-porous to a porous compact oxide, then to well-defined nanotubular structures and then, to nanograss structures.

Table 4-1 EDXS analyses results in %wt. performed on different sites on the surface of anodized specimens at 60 V for 120 min

Element	Upper Surface	Cavity
O	44.6±3.2	6.8±5.1
Ti	49.3±2.9	85.1±3.8
Al	3.7±0.2	2.1±0.9
V	2.5±0.2	6.0±2.8

Nevertheless, the behaviour of the two alloys is quite different. In Ti grade 5, nanotubular structures are obtained for a minimum time of 30 min at both 80 V and 100 V and up to 120 min at both 40 and 60 V. Moreover, it was possible to obtain defined nanotubes for anodization periods of 1 h. In contrast, longer anodization periods above 3 h were necessary to obtain defined nanotubular structures for 20, 40 and 60 V for Ti grade 2, while a mixture of both nanograss and porous compact layers were obtained after an anodization of 80 V 1 h on grade 2. Clearly, both the chemical nature and microstructure of the alloys influence the dissolution effect of the electrolyte used in this work, resulting in a very distinct morphological transition with the increase of the applied potential difference and time. In figures 4-9 and 4-10, FESEM micrographs at high magnifications of the anodic oxides over α and β phases, respectively, are reported for specimens anodized for 60 min at different applied potentials. It was possible to observe that the produced oxide had a dual morphology. The nanotubes grown over the α -phase presented a well-defined honeycomb-like tubular structure with thin walls and with inner diameters, which increased by increasing the applied voltage (Fig. 4-9). At high applied potentials (80V and 100 V), the tops of the TNTs walls appeared partially fractured due to the extensive thinning. The oxide grown over the β -phase at 20 V did not present an organized tubular structure (Fig. 4-10 a). Poorly organized TNTs were observed at 40 V (Fig. 4-10 b), and a further increase of the potential increased the TNTs' organization degree (Fig. 4-10 c-e). The nanotubes obtained over the β -phase presented generally much thicker walls and smaller inner diameters with respect to those produced under the same conditions over the α -phase.

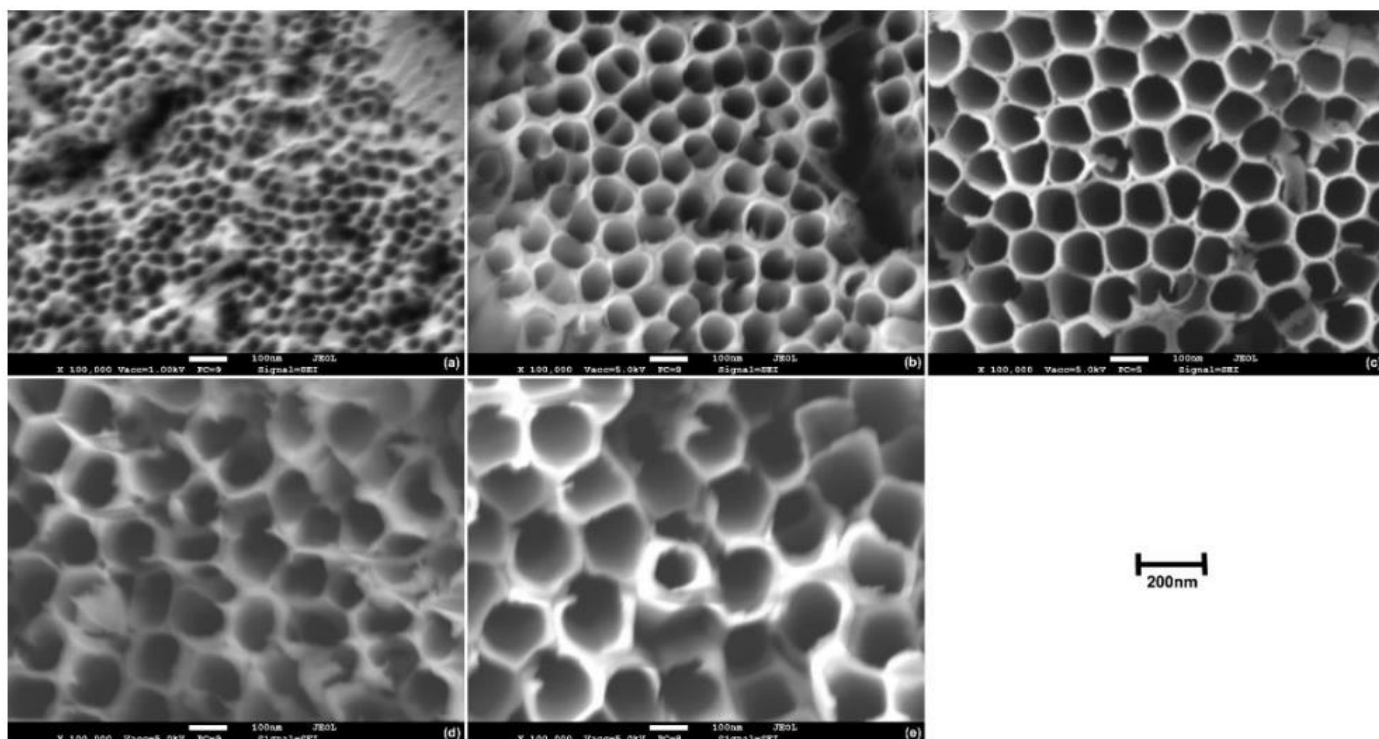


Figure 4-9: High magnification FESEM micrographs depicting a top-view of the anodic oxide layer produced over the α -phase through electrochemical anodization for 60 min at (a) 20 V, (b) 40 V, (c) 60 V, (d) 80 V, and (e) 100 V.

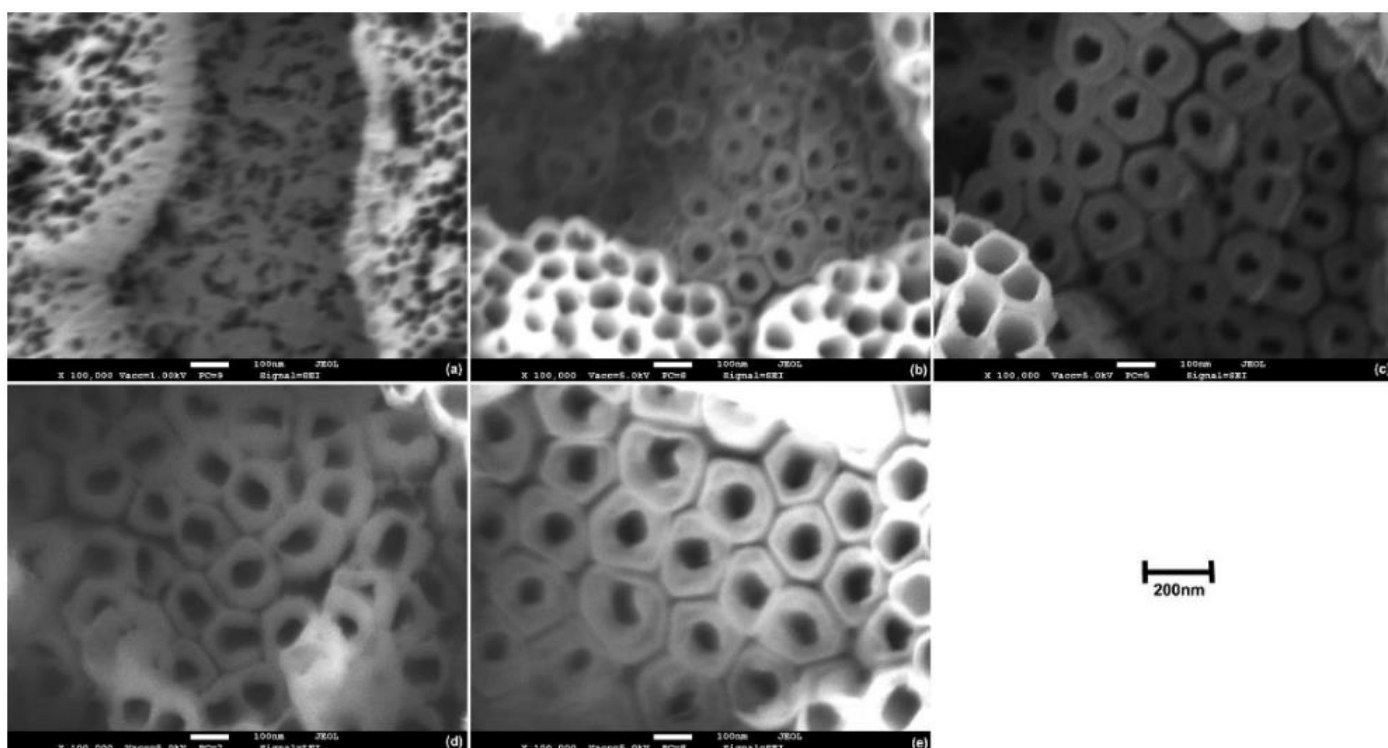


Figure 4-10: High magnification FESEM micrographs depicting a top-view of the anodic oxide layer produced over the β -phase through electrochemical anodization for 60 min at (a) 20 V, (b) 40 V, (c) 60 V, (d) 80 V, and (e) 100 V.

This dual morphology was previously reported by several authors, which confirm that over the α -phase a well-defined nanotubular structure is generally grown, while over the β -phase, pits are observed with an oxide not so developed, that may or may not present a nanotubular structure, depending on the anodization process conditions.^[12,18–21] The early works of Zwilling *et al.* attributed this phenomenon to the higher electrochemical stability of the V rich grains, which resulted in a lower growth rate of the anodic oxide.^[22,23] This was later corroborated by other authors.^[24,25] On the other hand, Jordanovova *et al.*^[21] reported that the growth rate over the β -phase was faster due to the quicker diffusivity into the body-centered cubic structure, but the controversial process of TiO_2 dissolution during the TNTs growth proceeded preferentially over the β -phase. Nevertheless, there are also works that do not report a dual-morphology on anodized Ti6Al4V alloy, which could be related to the different compositions of the electrolytes used in the anodization process.^[26,27]

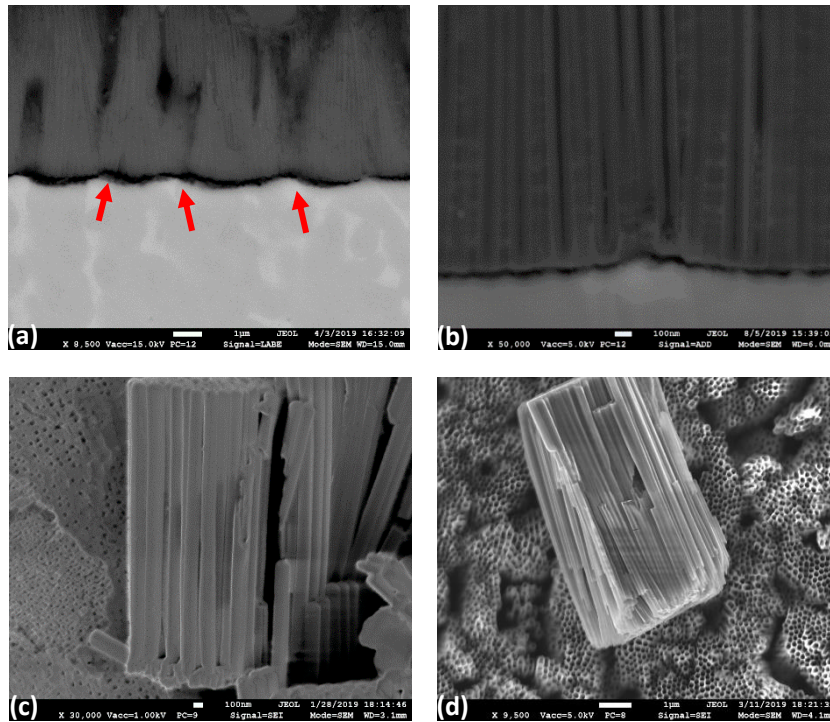


Figure 4-11: (a) and (b) FESEM micrographs of samples anodized at 60 V for 60 min, depicting a cross-section of the tubes grown over the α and β phases (indicated by the red arrows); (c) and (d) FESEM micrographs of samples anodized at (c) 60 V 60 min, (d) 100 V 60 min.

Figure 4-11 shows FESEM micrographs depicting the anodic oxide layer for the sample anodized at 60 V for 60 min, in cross section. The β -phase grains (red arrows) appear higher than the α -phase grains, which indicates the lower dissolution rate of the V-rich phase (Fig. 4-11 a). These results seem to confirm the assumption made in the works

of Zwilling *et al.* in 1999, and defended by other authors, which attributed the lower length and lower diameter of the β -phase pores to the higher electrochemical stability of the β -phase grains.^[22–26] Moreover, the nanotubes grown over the β -phase are much shorter, and almost invisible whereas over the α -phase present well defined and smooth tube walls. This is highlighted in Fig. 4-11 c and d, that shows FESEM micrographs that detail the side wall morphology of the nanotubes produced over the α -phase at 60 V and 100 V, for 60 min, from detached fragments of the anodic oxide.

Considering the results previously reported for Ti grade 2 anodized at 40 V, the difference in morphology of tube walls on Ti grade 5 could be related with the different growth kinetics of the nanotubes. To better understand how the morphology changes with the variation of the applied potential difference and time, the inner diameters were measured for all tested samples on which surface areas with completely open nanotubes were encountered, even at low extension. The results are reported in Figure 4-13. Regarding the nanotubular layer grown over the α -phase (Fig. 4-12 a), the diameter increased in an almost linear way with the increase of the applied voltage. For an anodization time of 30 min, the inner diameter measured was about 55 nm for 60V, reaching 160 nm for 100 V. Similarly, for 60 min of anodization time, the inner diameter measured was of about 75 nm for 40 V, reaching 165 nm for 100 V. For 120 min, the same trend was observed. The increase of anodization time under a constant applied potential difference also led to an increase of the nanotube diameter, even at a lower extension. The inner diameter of the nanotubes grown over the β -phase (Fig. 14-2 b) was much lower compared to that observed on α -phase nanotubes until 60 V. By further increasing the applied voltage, no significant increase of the diameter was observed. The effect of time, keeping constant the voltage, was marked at low potential differences (40 V and 60 V); instead, it was almost irrelevant at higher voltages (80 V and 100 V), showing a quasi-steady state of the variation of the diameter.

Pore diameter, inter tube spacing and self-ordering are strongly related to pore nucleation during the initial phase of the growth process. The applied potential difference directly determines the strength of the electrical field and, hence, the ion migration rate and the dissolution rate. As such, they largely influence pore nucleation during the initial phase of the growth process, which in turn determines pore diameter, inter tube spacing, and self-ordering of the tubular structures. Thus, the direct relationship between the inner diameter and the voltage is expected and was extensively reported for TNTs grown on different Ti substrates.^[14,15,27–29] Moreover, is in line to what is previously reported for Ti grade 2 (see section 4.1.2).

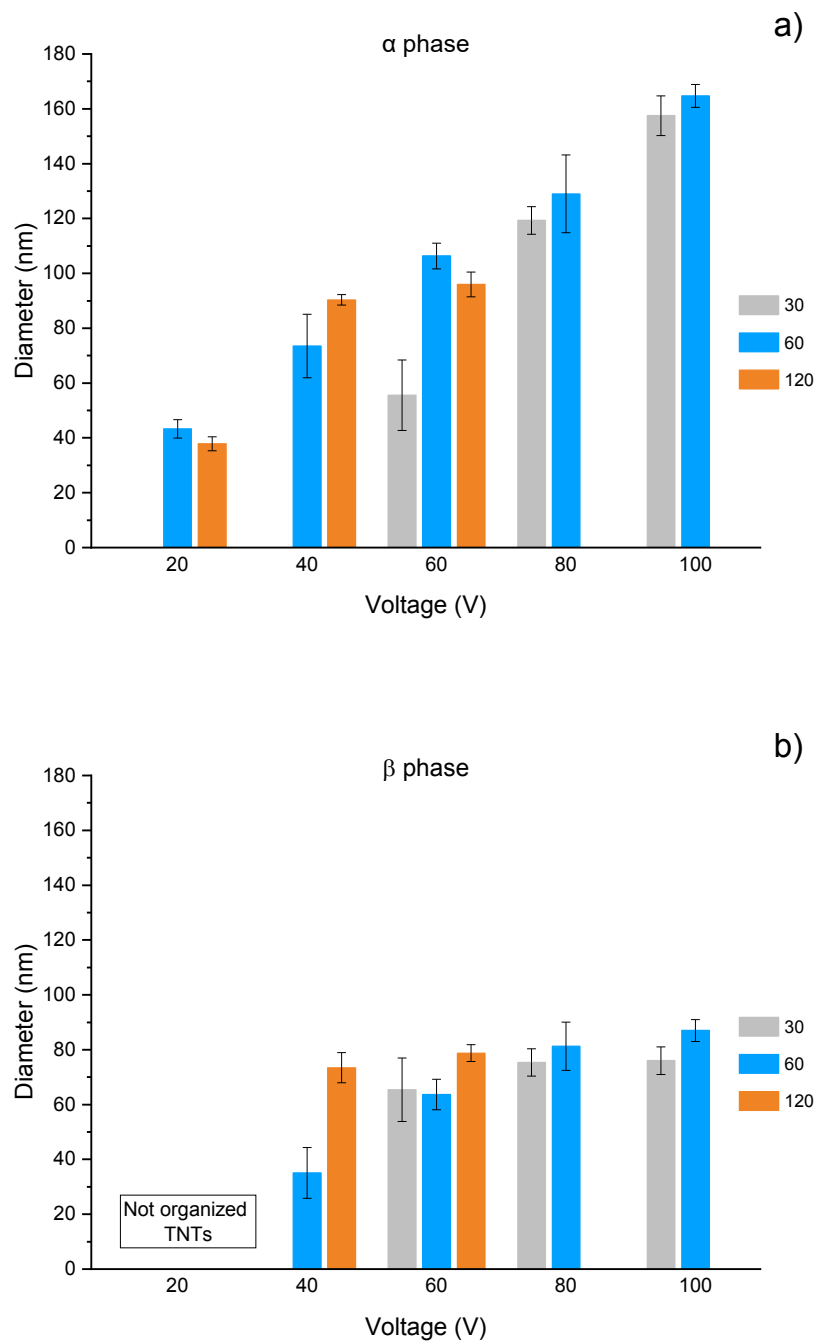


Figure 4-13: Average inner diameter of nanotubes as a function of applied potential and anodization time for the conditions where open-nanotubes have been observed. A) α – phase nanotubes and b) β -phase nanotubes.

On the other hand, increased anodization time leads to a longer dissolution. It was demonstrated that not all pores formed during the nucleation generated an individual tube. Some pores stop to grow at some point during the process and are incorporated into larger growing pores, thus increasing the final diameter. While an intense dissolution may lead to an increase of pore diameter in the early stages of tubular development, once stage 2 of tubular development is reached (according to Seçkin and Ürgen^[5]), over-dissolution of the tube tops occurs, which could explain the inversion of the effect of time at 120 min of anodization for the samples produced at 60 V on the tubes grown on the α -phase. Thus, there is a limit on the effect of time, depending on the nature of the electrolyte. In aqueous electrolytes, the maximum thickness is normally achieved within a few minutes, but additional times (to a total between 30 min and 2 h) is required to allow the anodic oxide to rearrange itself and increase the degree of self-ordering. In organic electrolytes, the process is much slower and the dissolution phenomena are not as significant, and hence the effect of increasing time on the diameter is less evident.^[11]

4.2.2 Growth process of TNTs on Ti grade 5

In order to understand the influence of the microstructure on the growth and development of nanotubes over Ti grade 5, the samples were anodized at 60 V for different times including very short ones and observed by FESEM and AFM. AFM topographic maps of the anodized specimens are reported in Figure 4-14 and FESEM micrographs of the same samples are reported on Figure 4-15. The AFM topography maps reveal that after only 25s of anodization (Fig. 4-14 a) the β -phase grains appear higher than the α -phase grain and the grain boundaries are more marked compared to the as-polished Ti6Al4V alloy surface (Fig. 3-4 a and b, see section 3.2). This is an indication that an oxide has already been formed over the surface and that it is thicker over the β -phase grains. The FESEM micrographs after the same anodization time confirms the presence of a compact oxide over both phases (Fig. 4-15 a). By increasing the anodization time to 40s, the height difference between α - and β -phase grains increases (Fig. 4-14 b), indicating a faster growth rate of the oxide over the β -phase during the early β -phase anodization stages.

The FESEM micrograph (Fig. 4-15 b) confirms the AFM results and reveals the initiation of the pores formation over the β -phase compact oxide. The α -phase oxide remains compact. After 120 s, the α -phase oxide starts to grow more and the β -phase oxide formation slows down so that the difference in height becomes lower, with the β -phase grains still having the higher height (Fig. 4-13 c). The FESEM observations show that pores start to appear also on the oxide surface over the α -phase, while the ones over the β -phase

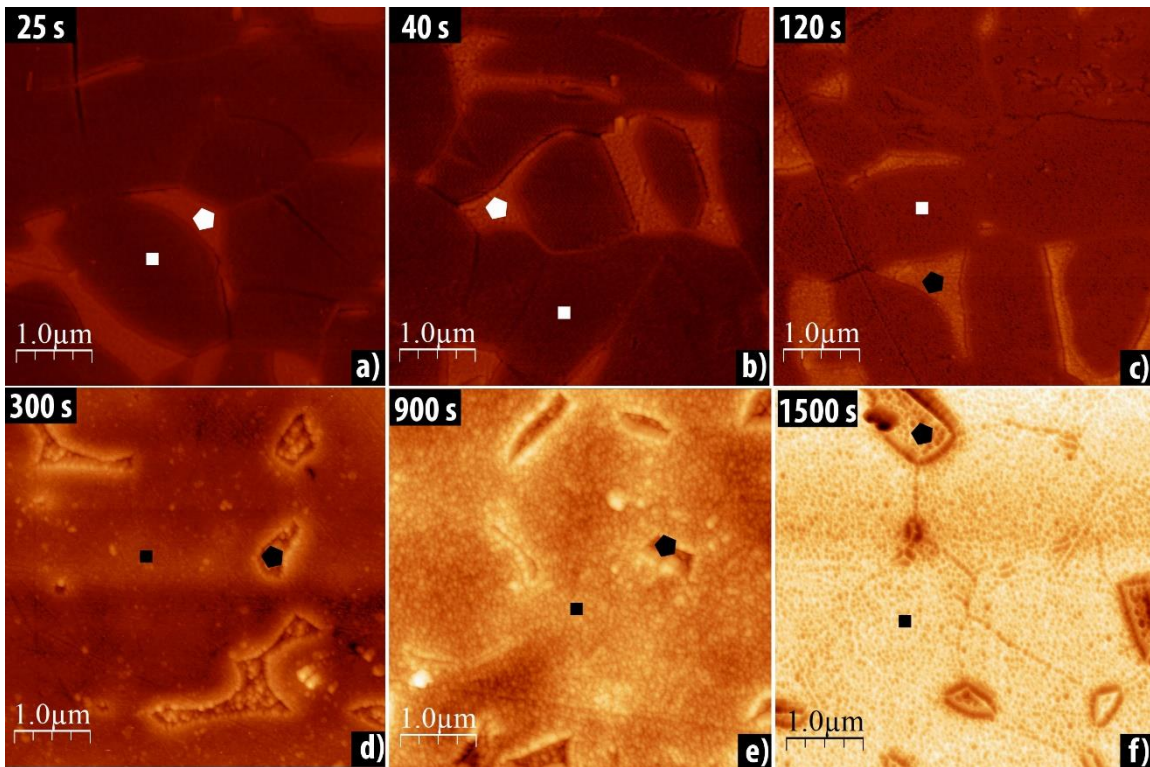


Figure 4-14 AFM topography maps for specimens anodized at 60 V at (a) 25 s, (b) 40 s, (c) 120 s, (d) 300 s, (e) 900 s and (f) 1500 s. ■: represents the α -phase; ◆: represents the β -phase.

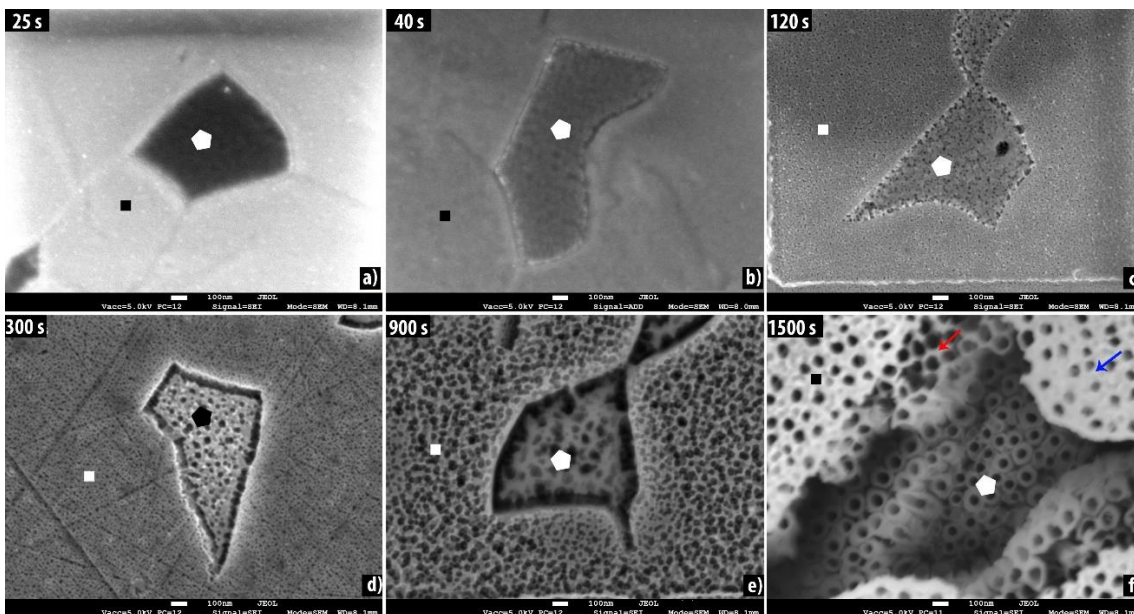


Figure 4-15 FESEM micrographs of samples anodized at 60 V at (a) 25 s, (b) 40 s, (c) 120 s, (d) 300 s, (e) 900 s and (f) 1500 s. ■: represents the α -phase; ◆: represents the β -phase.

become larger (Fig. 4-15 c). After 300 s the height difference is inverted; the anodic oxide over the β -phase grains appears lower than that over the α -phase (Fig. 4-14 d) indicating that the nanotubes are growing faster under the compact oxide layer on the α -phase than on the β -phase. The FESEM micrograph (Fig. 4-14 d) shows an increase on the pores diameter on the compact oxide layer over both phases with the ones on the β -phase being still larger. The same trend is maintained also after 900 s with the anodic oxide growing faster over the α -phase increasing the difference in height (Fig. 4-14 e). The dissolution process of the initially formed compact oxide continues over both phases as demonstrated by the increase of the pores size (Fig. 4-15 e). After 1500 s the nanotubes over the β -phase appear completely open and much shorter than those over the α -phase (Fig. 4-14 f). On the α -phase some areas with completely open nanotubes are visible (red arrow in Fig. 4-15 f), while on others the initially formed compact oxide is still covering the nanotubes upper part (blue arrow 4-15 f).

Considering the growth stages defined by the current transient model^[30], it is clear from the AFM and FESEM results that growth proceeds with different speeds on the two phases of the alloy. The initial compact oxide (stage I) grows faster over the β -phase, even if it presents a higher Volta potential which means that it should be electrochemically more stable. This could be attributed to the chemical composition of the formed oxides over the two phases. According to previous studies^[24], the higher content of Al in the α -phase in electrolytes containing high concentrations of F^- ions can lead to a re-passivation due to the formation of $4AlOF \cdot TiOF_2 \cdot H_2O$ or AlF_3 , which is poorly soluble. On the other hand, the presence of a high amount of V in the β -phase leads to the formation of a V-rich oxide which grows faster and presents pores even after 40s of anodization due to the higher solubility of V-oxides, resulting in a unstable passivity and thus earlier breakdown (stage II).^[19,31,32]

The trend is inverted once the first pores are formed over the compact oxide of the α -phase. Highly ordered nanotubes grow over both phases, protected by the porous compact layers. The growth rate is faster over the α -phase than over the β -phase as demonstrated by both AFM and FESEM results. The dissolution process on the bottom of the tubes due to the actions of F^- ions is faster over the α -phase, while the initially formed compact oxide dissolves slower protecting the integrity of the growing nanotubes the initially formed compact oxide of the β -phase dissolves faster but the integrity of the nanotubes is maintained contrarily to what is reported by other authors during the anodization of Ti6Al4V in aqueous electrolytes.^[23,24] The use of ethylene glycol electrolyte with a low amount of H_2O , slows down the dissolution of the water soluble V-rich oxides

and the β -phase. The final result is the formation of highly ordered nanotubes over both phases, with different lengths, internal diameters and wall-thicknesses.

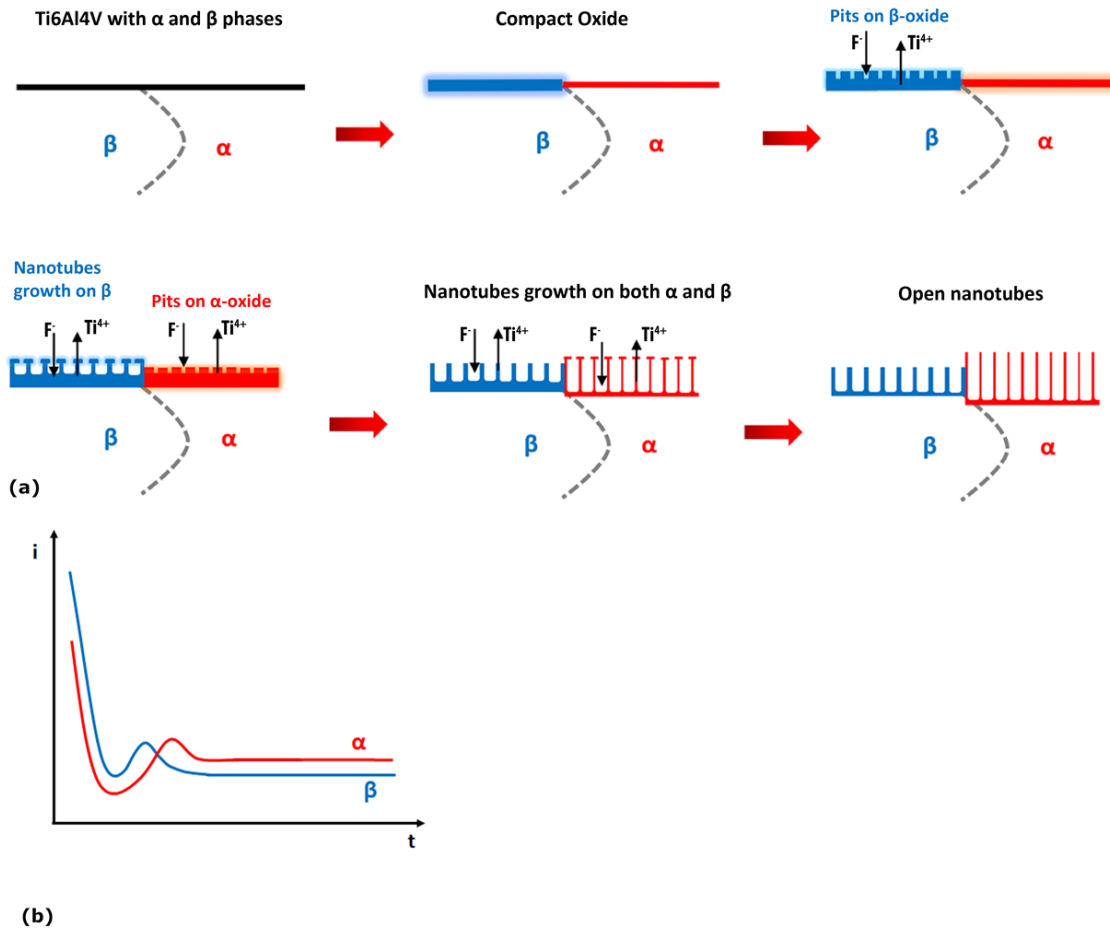


Figure 4-16 (a) Schematic representation of the different steps of growth of the anodic oxide layer in Ti6Al4V alloy (b) Suggestion of the individual current-time plot for each individual phase adapted from.^[30]

A proposed scheme for the growth steps is illustrated in figure 4-16, together with a theoretical current-time transient considering the individual behavior of each phase. Briefly, under an overall constant applied potential, the current density over the β -phase is initially higher than over the α -phase leading to the formation of a thicker barrier oxide, followed by a steady decrease in current density on both phases (stage I). At a certain point (before the first 40 s of anodization), there is a current peak corresponding to the pore nucleation on the β -phase oxide (stage II). The α -phase oxide follows shortly after (before the first 120 s) and then both reach a steady current (stage III) with a higher current density related to the nanotubes growing over the α -phase.

4.3 Partial conclusions

In this part of the work, the morphology of TiO₂ nanotubes produced over Ti grade 2 (99.8% pure) and Ti grade 5 (Ti6Al4V), through electrochemical anodization was thoroughly described. Moreover, the effect of electrolyte aging, applied potential difference and time was investigated. In general, the chemical composition of the base alloy has a major influence over the morphology of the produced TNT layers. An initial aging of the electrolyte was necessary in order to achieve well-defined nanotubular structures and reproducible results on both alloys. Overall, the growth of the nanotubes and their evolution occurs at a slower rate on Ti grade 2 than on Ti grade 5. This is particularly evident considering not only the optimum “ageing” period of the electrolyte (10-150 h for Ti grade 2, 1-20 h for Ti grade 5), but also the transition from a porous compact oxide to a nanotubular morphology (a minimum of 3 h for grade 2, while 1 h was enough for grade 5). Clearly, the composition of the alloy phases directly determines the electrochemical dissolution effect on both alloys which in turn leads to different growth kinetics.

The dual phase microstructure of the Ti6Al4V alloy leads to the formation of a non-uniform anodic oxide for all tested samples. Open mouth nanotubes are present over both phases but their morphology strongly differs. Under optimized conditions the nanotubes grown over the α -phase present a well-defined honeycomb-like nanotubular structure, with thin walls, while the ones grown over the β -phase are much shorter, with thicker walls and smaller inner diameter. On the other hand, the single phase of Ti grade 2 results in a mostly uniform nanotubular layer. Nevertheless, the growth behavior of both alloys, although presenting a similar transition to what was described by Urgen^[5], is quite different in the sense that tube development occurs more rapidly for Ti grade 5 (minimum time of 1 h for at least 60 V or 2 h for 40 V) than in grade 2 (minimum time of 4 h for the same voltages). Clearly both the chemical composition, as well as, the microstructure (specially the specific arrangement of the phases), have an effect on both the dissolution of the substrate and of the oxide by F⁻ ions. This is particularly evident when studying the effect of both applied potential difference and time over the obtained tube diameter. For Ti grade 2, the inner diameter increases linearly with both the increase in applied potential and time (although less evident). For Ti grade 5, a similar behavior can be described for the α -oxide, but for the β -phase nanotubes the effect of both time and voltage is less marked.

The study of the early stages of the anodization process revealed that the initial compact oxide grows faster over the β -phase as higher Al content of the α -phase causes

its re-passivation. The higher solubility of the V-rich oxide leads also to an earlier pore formation over the β -phase. The trend is inverted once the pores are formed over the compact oxide of the α -phase. The growth rate of the α -phase TNTs is higher than that of the β -phase ones, leading to the formation of longer, well defined nanotubes with thinner walls.

For the specific applications considered in this work, where a 70-100 nm inner diameter could favor the osseointegration, the optimized conditions of electrochemical anodization are an applied potential difference of 40 V for 6 h for Ti grade 2, and 60 V for 1 h for Ti grade 5.

4.4 Bibliography

1. Suhadolnik L, Marinko Ž, Ponikvar-Svet M *et al.* Influence of Anodization-Electrolyte Aging on the Photocatalytic Activity of TiO₂ Nanotube Arrays. *J Phys Chem C* 2020;**124**:4073–80.
2. Guo T, Oztug NAK, Han P *et al.* Old is gold: Electrolyte aging influences the topography, chemistry, and bioactivity of anodized TiO₂ nanopores. *ACS Appl Mater Interfaces* 2021;**13**:7897–912.
3. Gulati K, Santos A, Findlay D *et al.* Optimizing anodization conditions for the growth of titania nanotubes on curved surfaces. *J Phys Chem C* 2015;**119**:16033–45.
4. Lee K, Kim J, Kim H *et al.* Effect of electrolyte conductivity on the formation of a nanotubular TiO₂ photoanode for a dye-sensitized solar cell. *J Korean Phys Soc* 2009;**54**:1027–31.
5. Seçkin E, Ürgen M. A kinetic model for determining morphology transitions and growth kinetics of titania nanotubes during anodization of titanium in ethylene glycol based electrolytes. *Surf Coatings Technol* 2021;**409**:126840.
6. Taveira L V., Macák JM, Tsuchiya H *et al.* Initiation and Growth of Self-Organized TiO₂ Nanotubes Anodically Formed in NH₄F/(NH₄)₂SO₄ Electrolytes. *J Electrochem Soc* 2005;**152**:B405.
7. Macak JM, Tsuchiya H, Taveira L *et al.* Smooth anodic TiO₂ nanotubes. *Angew Chemie - Int Ed* 2005;**44**:7463–5.
8. Regonini D, Bowen CR, Jaroenworaluck A *et al.* A review of growth mechanism, structure and crystallinity of anodized TiO₂ nanotubes. *Mater Sci Eng R Reports* 2013;**74**:377–406.
9. Raja KS, Gandhi T, Misra M. Effect of water content of ethylene glycol as electrolyte for synthesis of ordered titania nanotubes. *Electrochem commun* 2007;**9**:1069–76.
10. Valota A, LeClere DJ, Skeldon P *et al.* Influence of water content on nanotubular anodic titania formed in fluoride/glycerol electrolytes. *Electrochim Acta* 2009;**54**:4321–7.
11. Regonini D, Satka A, Jaroenworaluck A *et al.* Factors influencing surface morphology of anodized TiO₂ nanotubes. *Electrochim Acta* 2012;**74**:244–53.
12. Sreekantan S, Khairul A, Saharudin Z *et al.* Formation of TiO₂ nanotubes via anodization and potential applications for photocatalysts, biomedical materials, and photoelectrochemical cell. *IOP*

Conf. Ser.:Materials Science and Engineering. Vol 21. 2011, 1–18.

13. Ozkan S, Mazare A, Schmuki P. Critical parameters and factors in the formation of spaced TiO₂ nanotubes by self-organizing anodization. *Electrochim Acta* 2018;**268**:435–47.
14. Butail G, Ganesan PG, Teki R *et al.* Branched titania nanotubes through anodization voltage control. *Thin Solid Films* 2011;**520**:235–8.
15. Macak JM, Hildebrand H, Marten-Jahns U *et al.* Mechanistic aspects and growth of large diameter self-organized TiO₂ nanotubes. *J Electroanal Chem* 2008;**621**:254–66.
16. Chernozem R V., Surmeneva MA, Surmenev RA. Influence of Anodization Time and Voltage on the Parameters of TiO₂ Nanotubes. *IOP Conf Ser Mater Sci Eng* 2016;**116**, DOI: 10.1088/1757-899X/116/1/012025.
17. Bervian A, Coser E, Khan S *et al.* Evolution of TiO₂ nanotubular morphology obtained in ethylene glycol/glycerol mixture and its photoelectrochemical performance. *Mater Res* 2017;**20**:962–72.
18. Shankar K, Mor GK, Fitzgerald A *et al.* Cation effect on the electrochemical formation of very high aspect ratio TiO₂ nanotube arrays in formamide-water mixtures. *J Phys Chem C* 2007;**111**:21–6.
19. Matykina E, Conde A, De Damborenea J *et al.* Growth of TiO₂-based nanotubes on Ti-6Al-4V alloy. *Electrochim Acta* 2011;**56**:9209–18.
20. Saharudin KA, Sreekantan S, Aziz SNQAA *et al.* Surface modification and bioactivity of anodic Ti6Al4V alloy. *J Nanosci Nanotechnol* 2013;**13**:1696–705.
21. Jordanovová V, Losertová M, Štencek M *et al.* Microstructure and properties of nanostructured coating on Ti6Al4V. *Materials (Basel)* 2020;**13**:1–11.
22. Zwilling V, Aucouturier M, Darque-Ceretti E. Anodic oxidation of titanium and TA6V alloy in chromic media. An electrochemical approach. *Electrochim Acta* 1999;**45**:921–9.
23. Zwilling V, Darque-Ceretti E, Boutry-Forwille A *et al.* Structure and growth of anodic oxide films on titanium and TA6V alloy. *Surf Interface Anal* 1999;**27**:629–37.
24. Zhang H, Man C, Wang L *et al.* Different corrosion behaviors between α and β phases of Ti6Al4V in fluoride-containing solutions: Influence of alloying element Al. *Corros Sci* 2020;**169**, DOI: 10.1016/j.corsci.2020.108605.
25. Marino CEB, Biaggio SR, Rocha-Filho RC *et al.* Voltammetric stability of anodic films on the Ti6Al4V alloy in chloride medium. *Electrochim Acta* 2006;**51**:6580–3.
26. Sarraf M, Zalnezhad E, Bushroa AR *et al.* Effect of microstructural evolution on wettability and tribological behavior of TiO₂ nanotubular arrays coated on Ti–6Al–4V. *Ceram Int* 2015;**41**:7952–62.
27. Beltrán-Partida E, Moreno-Ulloa A, Valdez-Salas B *et al.* Improved osteoblast and chondrocyte adhesion and viability by surface-modified Ti6Al4V alloy with anodized TiO₂ nanotubes using a super-oxidative solution. *Materials (Basel)* 2015;**8**:867–83.
28. Berger S, Tsuchiya H, Schmuki P. Transition from Nanopores to Nanotubes: Self-ordered Anodic Oxide Structures on Titanium-Aluminides. *J Biomed Mater Res, Part A* 1997;**144**:47.
29. Tsuchiya H, Berger S, Macak JM *et al.* Self-organized porous and tubular oxide layers on TiAl alloys. *Electrochem Solid-State Lett* 2007;**9**:2397–402.

30. Roy P, Berger S, Schmuki P. TiO₂ nanotubes: Synthesis and applications. *Angew Chemie - Int Ed* 2011;**50**:2904–39.
31. Nevárez-Martínez MC, Mazierski P, Kobylański MP *et al.* Growth, structure, and photocatalytic properties of hierarchical V₂O₅-TiO₂ nanotube arrays obtained from the one-step anodic oxidation of Ti-V alloys. *Molecules* 2017;**22**, DOI: 10.3390/molecules22040580.
32. Macak JM, Tsuchiya H, Taveira L *et al.* Self-organized nanotubular oxide layers on Ti-6Al-7Nb and Ti-6Al-4V formed by anodization in NH₄F solutions. *J Biomed Mater Res - Part A* 2005;**75**:928–33.

5 HEAT TREATMENT AND CORROSION RESISTANCE.

TiO₂ can occur in the amorphous or crystalline state, possessing three polymorphs: anatase, rutile and brookite. Rutile is generally the most thermodynamically stable bulk phase, while anatase and brookite are metastable phases.^[1] However, at nanoscale, surface energy and stresses have a significant effect on phase stability and anatase is considered to be the most stable. An anatase phase has been shown to improve the mechanical stability of TiO₂ nanotubes. Moreover, crystalline TNTs present a higher potential for spontaneous nucleation of hydroxyapatite on their surface, improving biocompatibility. From literature, it is known that the TNTs produced through electrochemical anodization are usually amorphous, unless conditions of very high voltage or time are applied. However, a common strategy to tailor the structure of TiO₂ into desired crystalline phase (or phases) for specific applications, is to perform post-anodizing heat-treatments (or annealing) processes.^[2–5]

This chapter is focused on two distinct purposes: a) the effect of heat treatments to the structure of the produced anodic oxide, which was evaluated by XRD and FESEM analysis on samples heat treated at 500°C either in air atmosphere or vacuum conditions; b) the effect of electrochemical anodization and post-anodizing heat-treatments on the corrosion resistance of both alloys evaluated by electrochemical measurements. This work comprises the following activities:

- Heat-treatment (H.T.) of polished (non-anodized) and anodized Ti grade 2 and grade 5 samples at 500°C for 3 hours in either air atmosphere or vacuum;
- Potentiodynamic polarization measurements in Phosphate Buffered Saline (PBS) solution.
-

5.1 Effect of anodization and heat-treatment on Ti grade 2 TNTs structure

5.1.1 Effect of heat treatment on bare samples

Figure 5-1 compares the surface morphology between as-polished Ti grade 2 non-heat treated and annealed at 500°C for 3h either in air atmosphere or under vacuum conditions. The photographs show that samples annealed in vacuum present a similar

aspect to the non-heat-treated ones, while annealing in air atmosphere gives the as-polished Ti grade 2 a light blue colour.

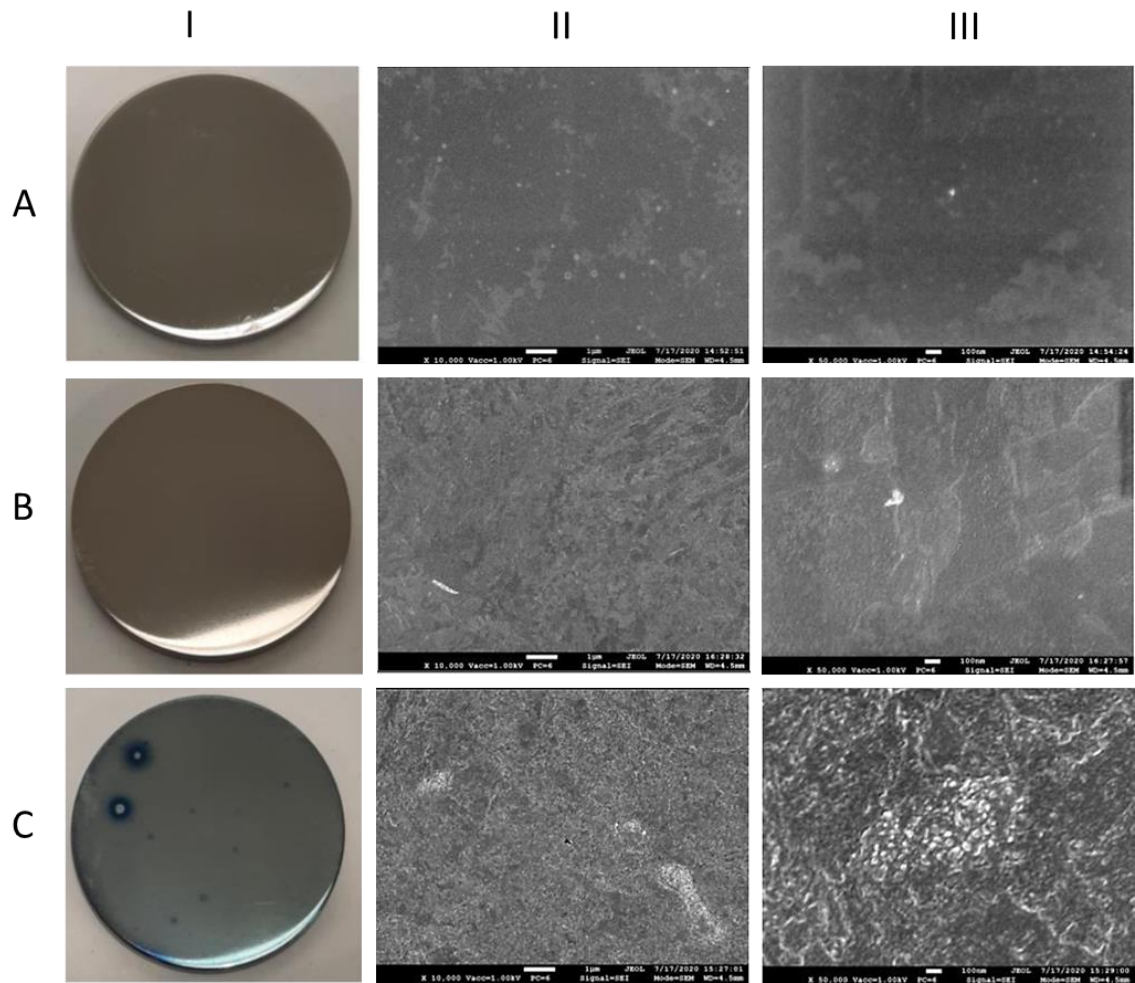


Figure 5-1: A top-view of as-polished Ti grade 2 (A), polished and annealed at 500°C for 3 h under vacuum conditions (B) or in air atmosphere (A). I-photographs; II - FESEM micrograph with a magnification of 10,000 ×; III - FESEM micrograph with a magnification of 50,000 ×.

From the FESEM micrographs, there are only minimal differences between the surface morphology of the as-polished samples non-heat treated, and the ones annealed under vacuum conditions. However, for the samples heat treated in air atmosphere, there is the formation of a thermal oxide over the whole surface, due to the presence of oxygen. In the high magnification micrograph (Fig. 5-1 CIII) the growth of small grains, with dimensions in the order of tens of nanometers, can be noticed on the surface of the samples.

Cross-section FESEM micrographs of this sample are reported in Figure 5-2. The produced thermal oxide is quite compact, uniform and well adhered to the substrate having a thickness between 100 to 150 nm. Considering the previous results, the as-

polished samples and the samples prepared under vacuum conditions were not analysed since they did not present any signs of significant superficial oxidation.

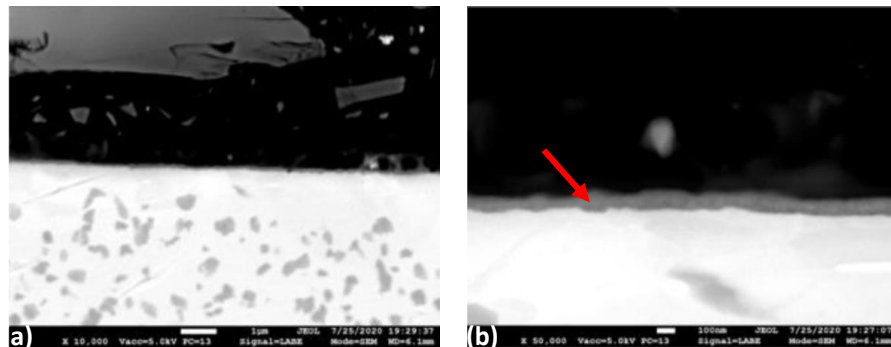


Figure 5-2: FESEM micrographs at low (a) and high (b) magnification, depicting a cross section view of a polished Ti grade 2 annealed at 500°C for 3 h in air atmosphere. The red arrow indicates the thermal oxide layer.

Figure 5-3 presents X-ray diffractograms of the as-anodized Ti grade 2 sample and the samples heat-treated at 500°C, either in vacuum or in air atmosphere. The patterns of the as-polished sample and the sample heat treated under vacuum conditions, are similar with the Bragg peaks corresponding to α phase of the Ti grade 2 substrate, thus confirming that the heat-treatment performed under vacuum conditions does not provoke substantial modifications in the alloy microstructure. The diffractogram of the sample heat treated in

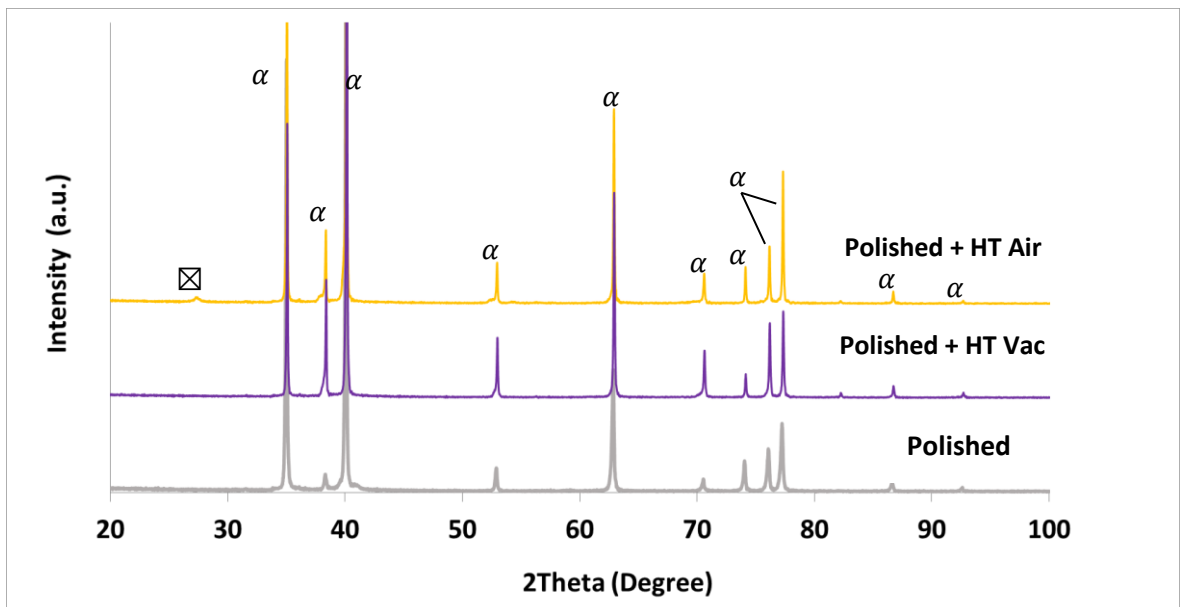


Figure 5-3: X-ray diffractograms of as-polished Ti grade 2 samples before (Polished) and after H.T at 500°C in either air atmosphere (Polished + HT Air) or under vacuum conditions (Polished+ HT Vac). α : peaks corresponding to Ti α -phase, \boxtimes : peaks corresponding to rutile TiO_2 .

air atmosphere presents an additional peak at 2θ diffraction angle of 27° , which was identified as main peak of rutile TiO_2 oxide. Its low intensity can be attributed to the low thickness of the thermal oxide (100 – 150 nm).

The previous results can be explained by the difference in the used annealing environments. Annealing in vacuum is known to lead to the reduction (i.e., creation of oxygen vacancies) on the existing, naturally formed, thin TiO_2 layer on the surface of the sample, a phenomenon that has been explored for various applications, including increasing hydroxyl concentration on TiO_2 surface which can favour cellular adhesion.^[6] On the other hand, annealing in air atmosphere is equivalent to performing a thermal oxidation, a well-known technique for the production of a crystalline thermal oxide film on the surface of Ti alloys, for temperatures above 200°C . Usually in this process, the applied temperature, cooling time and rate will influence the formation of mechanically stable, thick and well-adhered TiO_2 film.^[7] As seen in Figure 5-2, the employed thermal treatment in this work allowed for the production of a stable and well-adherent thermal oxide, on the surface of Cp-Ti, with a rutile crystalline phase. Due to the presence of a much thicker thermal oxide on the samples annealed on air, it is not possible to conclude about the influence of each atmosphere on the crystallization of the naturally occurring TiO_2 film present on the surface of the alloy.

5.1.2 Effect of heat treatment on anodized samples

Figure 5-4 presents photographs and FESEM micrographs of Ti grade 2 samples anodized at 40 V and 6 h, prior and after heat treatment at 500°C for 3 h in either air atmosphere or under vacuum conditions. From the photographs is possible to perceive differences in color on the anodic oxide. The as-anodized surface has a light brown color (Fig. 5-4 AI) which switches to dark brown or to black after annealing in either air atmosphere (Fig 5-4 CI) or vacuum conditions (Fig. 5-4 BI). From the FESEM micrographs it is possible to observe that, in spite of the difference in color, none of the heat treatments leads to significant changes in the morphology of the produced nanotubes. The honeycomb like morphology is maintained, with open tops and an approximately 100 nm diameter as was previously described in Figure 4-7 (see section 4.1.2). The only difference that can be noticed is a slight thickening of the nanotube walls for the samples annealed on air. However, it does not have a significant effect on the inner diameter of the tubes.

Figure 5-5 shows FESEM micrographs depicting a cross-sectional view of Ti grade 2 samples anodized at 40 V for 6 h prior and after heat-treatment at 500°C , for 3 h, in air. Some detachments and imperfections are visible, which could be attributed to the process

of metallographic preparation, which inevitably introduces damages due to the diverse nature of the two materials, the ductile metal substrate and a porous and fragile oxide. The sample annealed in air atmosphere presents a compact oxide layer at the interface between the nanotubular layer and the substrate (arrow in Fig. 5-5 d) has a thickness of about 150-200 nm, similar to the one formed in the as-polished sample (Fig. 5-2). From these results it is possible to assume that, during the heat treatment in air, oxygen diffuses through the porous structure of the anodic oxide, leading to the thermal oxidation of the metal substrate. From the high magnification micrographs, it is possible to observe that the bottom of the tubes annealed in air is no longer distinguishable, as they are incorporated into the thermal oxide layer.

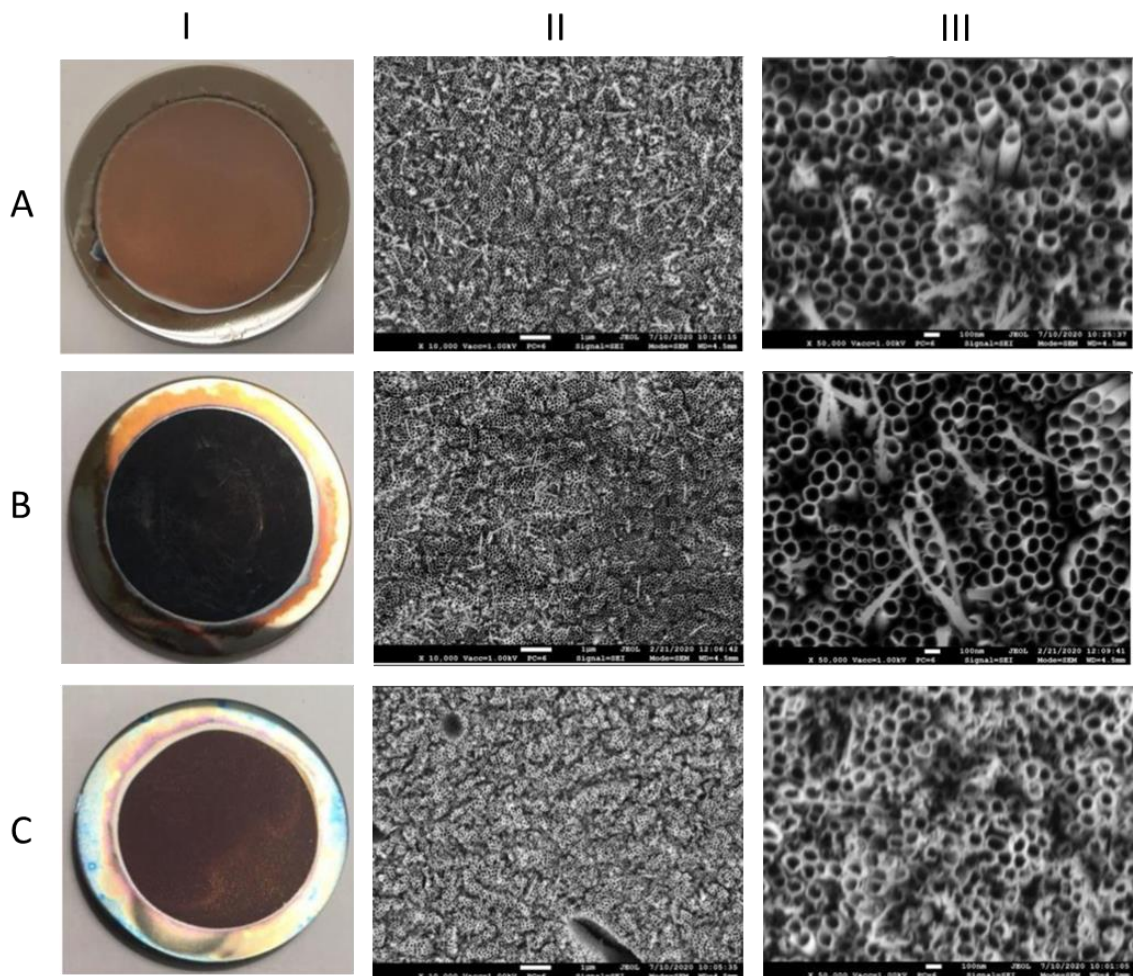


Figure 5-4: A top-view of oxide of Ti grade 2 anodized at 40 V 6 h (A), anodized and annealed at 500°C for 3 h under vacuum conditions (B) or in air atmosphere (C). I-photographs; II - low magnification FESEM micrographs; III – high magnification FESEM micrographs.

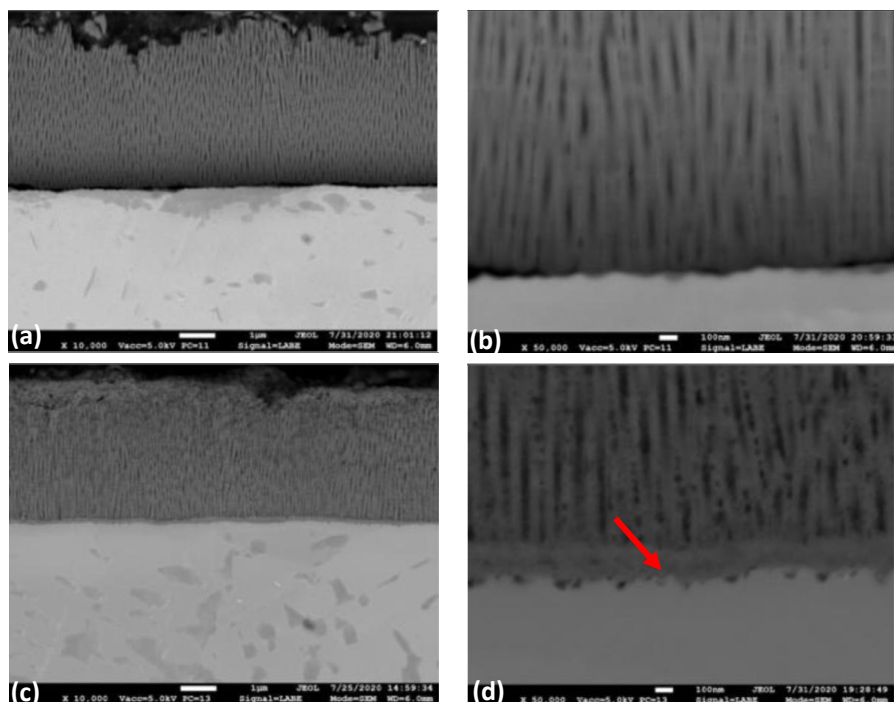


Figure 5-5: Cross section FESEM micrographs of Ti grade 2 samples anodized at 40V and 6h (a and b) and anodized and annealed at 500°C for 3 h in air atmosphere(c and d). The red arrow indicates the thermal oxide layer.

The X-ray diffractograms of as-polished Ti grade 2 as well as Ti grade 2 anodized at 40 V for 6 h are reported in Figure 5-6. No significant differences can be observed comparing the two diffractograms, as all peaks identified correspond to the Ti α -phase. A magnification of the diffractograms at low angles, after superposition of the lines is shown in the inset of figure 5-6. A higher background intensity is observed for the anodized sample between 20° and 30°, where the main peak of TiO_2 (of both rutile and anatase structure) should appear. This indicates that the produced nanotubes are amorphous, which was to be expected as described previously. [2,3,5,8]

Figure 5-7 presents X-ray diffractograms of Ti grade 2 samples anodized at 40 V for 6 h as well as samples anodized, and heat treated at 500°C for 3h in either air atmosphere or vacuum conditions. After HT in vacuum different peaks corresponding to anatase TiO_2 appear together with those corresponding to the Ti α -phase. The same peaks are present in the diffractogram of the heat-treated sample in air. In this case two more small peaks appear which correspond to the rutile TiO_2 . From these results it is possible to conclude that both heat treatments have led to recrystallization of the TiO_2 nanotubes, from amorphous to anatase phase. The rutile peaks, which appear after H.T. in air, can be attributed to the thermal oxide formed at the interface between the tubes and the substrate, considering the results described in section 5.1.1.

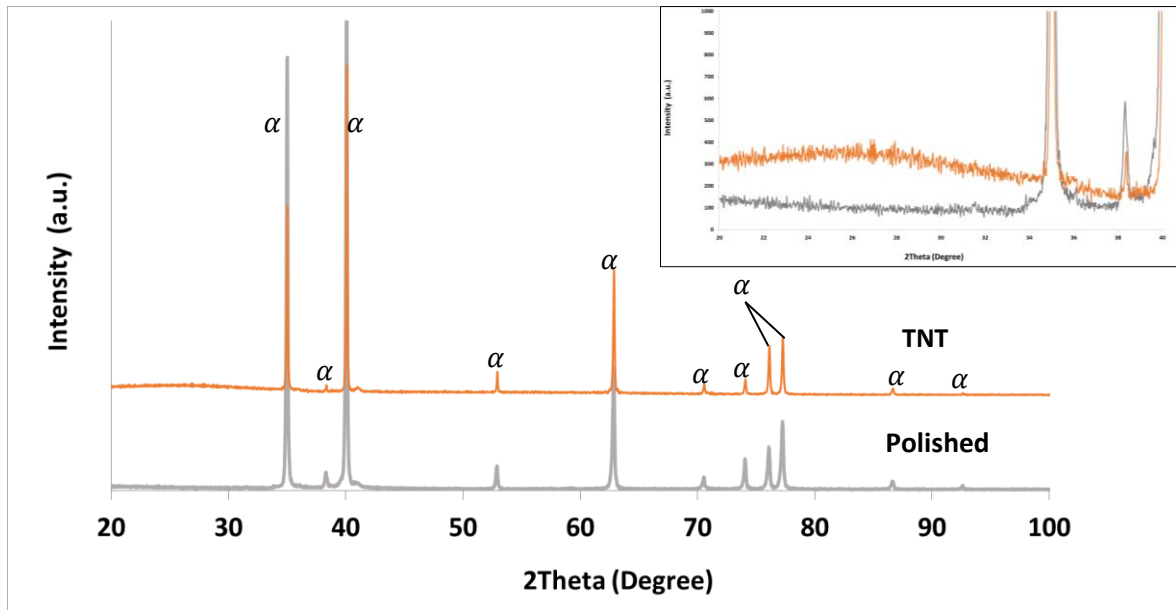


Figure 5-6: X-ray diffractograms of Ti grade 2 as-polished (Polished) and anodized at 40 V for 6 h (TNT).
 α : peaks corresponding to Ti α -phase.

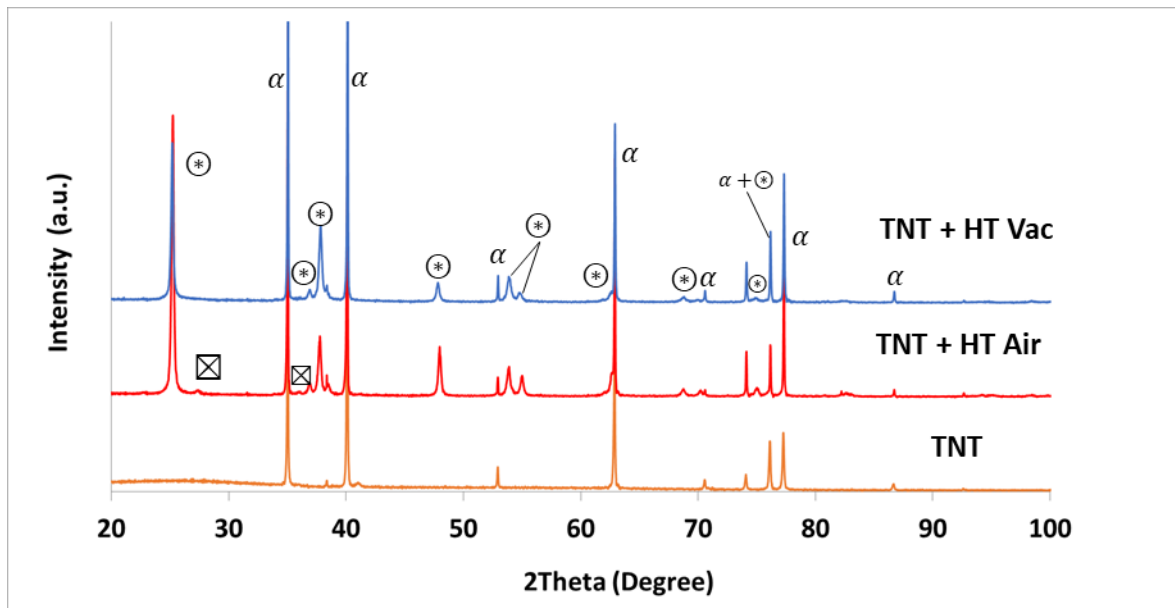


Figure 5-7: X-ray diffractograms of Ti grade 2 as-polished (Polished), anodized at 40 V for 6 h (TNT), and heat treated post-anodization at 500°C for 3 h in air atmosphere (TNT+HT Air) or under vacuum (TNT+HT Vac) α : peaks corresponding to Ti α -phase; \odot : peaks corresponding to anatase TiO_2 ; \boxtimes : peaks corresponding to rutile TiO_2 .

Annealing of TiO₂ nanotubes produced through electrochemical anodization has been extensively investigated over the last two decades. Parameters such as temperature, duration, ramping speed and annealing environment will influence the resulting crystalline structure.^[2,4,5] The work of Varghese *et al.*, was the first to establish the effect of annealing temperature and environments on the crystallinity of first generation (see section 1.3.3.1) TiO₂ nanotubes produced on Ti grade 2. Regarding temperature, an anatase crystalline phase is detectable after heat treatment at a lowest temperature of about 280°C, and becomes more predominant the higher the temperature. Complete conversion, in which no amorphous oxide is present, occurs after annealing at a lowest temperature of about 620°C. On the other hand, anatase to rutile phase transition begins to occur at around 480°C, becoming complete in heat-treatments performed at 680°C.^[9] Later works, such as the ones by Jaroenworarluck *et al.*^[10], Regonini *et al.*^[11] and Hilario *et al.*^[12], corroborate these findings, and today is generally considered that TiO₂ nanotubes can be converted from an amorphous material into an anatase after annealing at temperatures between ca 300 to 500°C, or into rutile after annealing at temperatures above 500°C, which is in accordance with the results obtained in this work.^[2,4,13] Moreover, it is important to mention that Jaroenworarluck *et al.* also observed that phase transition, with regard to temperature, was independent on the nature, either aqueous or organic, of the electrolyte.^[10]

Regarding the annealing environment, Varghese *et al.* tested the phase transition in oxygen-containing environments and in neutral environments, namely dry and wet argon and did not report any difference, considering only that the presence of water promoted the anatase to rutile transition.^[9] In contrast, Hyam *et al.* have more recently reported that heat treatments in neutral environments such as vacuum, argon or nitrogen have an equivalent effect on tube crystallization, and inhibit the anatase to rutile phase transition, which is in accordance to the results obtained in this work.^[14] A possible explanation has been reported by Roy *et al.*, that demonstrated that annealing in oxygen-containing environments leads to the formation of thin rutile oxide layers at the interface between the tubes and the metal substrate, through thermal oxidation, which was also observed in the reported results.^[15] Nevertheless, Fang *et al.* more recently proposed that, during annealing, the metal substrate induces oxygen vacancies on the anodic TiO₂ layer in the proximity to the substrate, inducing the anatase to rutile phase transition. Therefore it is possible that the rutile peak could be attributed in some degree to crystallization of rutile in the anodic oxide.^[16] Thus, the presence of oxygen is not necessary for phase transition of the oxide in anodized samples,^[5] but when present leads to the formation of a thermal oxide at the TNTs-substrate interface, as was previously observed on the bare samples.^[17]

Varghese *et al.* also further deliberated on the effect of annealing on nanotubular morphology. Both due to phase transitions (which involves mass transfer, nucleation and grain growth process) and to the high surface area of the nanostructures (which makes them prone to solid-state sintering), annealing can result in morphological alterations such as loss of area or porosity or even complete loss of morphology. The authors reported a stable morphology for temperatures below 580°C in oxygen-containing environments (although some rutile protrusions emerged at 500°C or higher in the rutile temperature range), while only a reduction in tube diameter and length was observed in argon containing atmospheres. Complete collapse of the structure occurred at a temperature of about 580°C.^[9] Accordingly, Jaroenworarluck *et al.*, reported complete loss of structure at temperatures of about 600°C.^[10] In this work, overall structural stability was maintained, with visible tube wall thickening and wall roughening after heat treatment, which could be attributed to oxide crystallization process.

5.1.3 Effect of anodization and heat treatment on corrosion resistance

Representative potentiodynamic polarization curves obtained on Ti grade 2 samples, as-polished and anodized at 40 V for 6 h in PBS, according to the procedure described in section 2.6, are reported in Figure 5-8. The potential was scanned till reaching 3V vs Ag/AgCl in order to evaluate the effect of both anodizing and post-anodizing heat treatments on the passive behaviour of Ti grade 2, even if in the clinical setting such high polarization potentials are never reached. According to previous studies, the range between 0.4 and 0.5 V vs Ag/AgCl is representative of the anodization conditions in the human body environment (henceforth referred as human body potential range).^[18] The as-polished alloy presents a corrosion potential (E_{corr}) of about -0.14V vs Ag/AgCl and a wide passive zone which extends till 3 V vs Ag/AgCl. Two distinct areas can be observed: a first passive zone which extends till 0.6 V vs Ag/AgCl. With a mean passive current density of about 4.5×10^{-6} A/cm² which progressively increased by increasing the applied potential. The second zone extends up to 3 V vs Ag/AgCl and presents a stable passive current density of about 4.01×10^{-6} A/cm². As described in section 1.1.2, Ti and its alloys are materials known to be resistant to corrosion in physiological environments, mainly due to the presence of chemically stable, protective TiO₂ film on their surface, which was confirmed by the wide passive range obtained in the PDP curve.

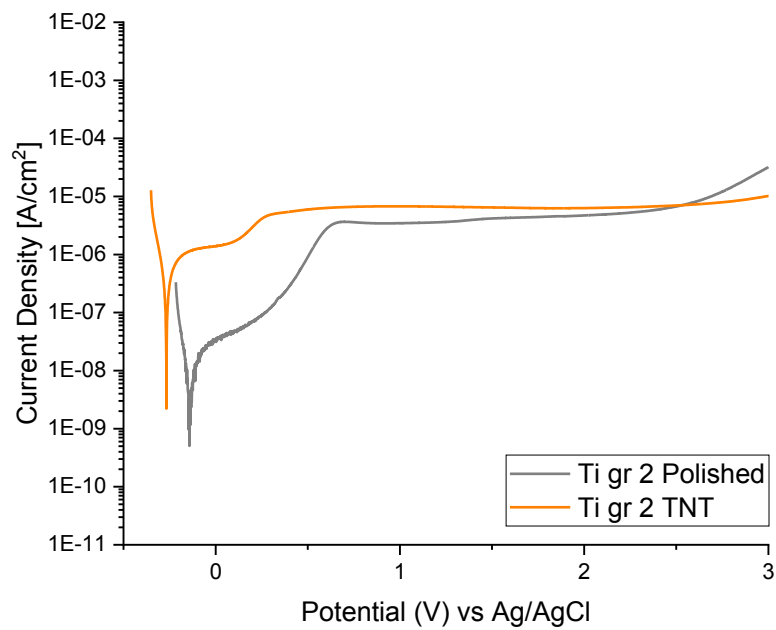


Figure 5-8: Representative potentiodynamic polarization curves of bare (Ti gr 2 polished) and anodized (Ti gr 2 TNT) Ti gr2 in PBS solution.

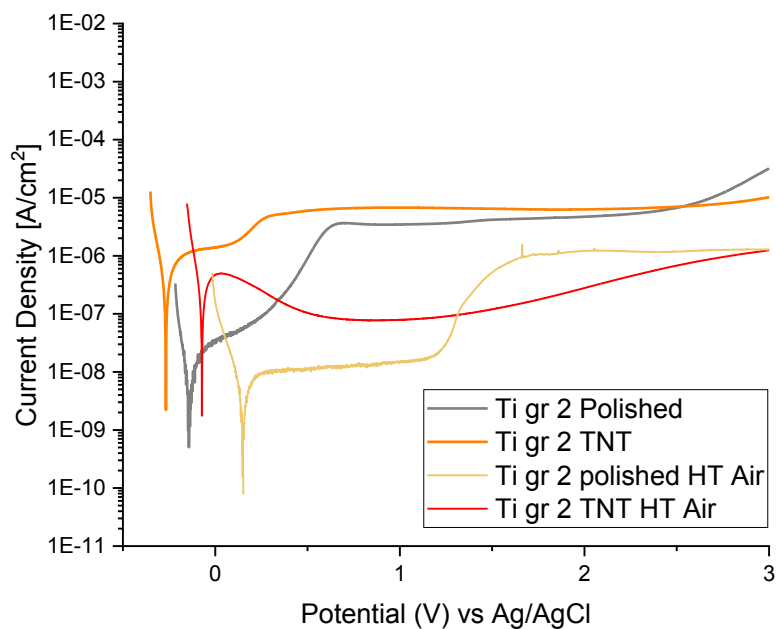


Figure 5-9: Representative potentiodynamic polarization curves of bare (Ti gr 2 polished) and anodized (Ti gr 2 TNT) Ti gr2 both prior and after heat treatment in air atmosphere in PBS solution.

On the other hand, the anodization affects both the corrosion potential and the first passive zone. Indeed, compared to the as-polished alloy the anodized sample presents a decrease of the corrosion potential of about -10 mV and an increase of the passive current density which reached 10^{-6} A/cm² for potentials up to 0.3 V vs Ag/AgCl. By increasing the applied potential the passive current density stabilizes at the same values as the one of the as-polished alloy. Thus, overall, the anodization process did not affect the corrosion behaviour of Ti grade 2. In the available literature, there seems to be some controversy regarding the effect of the anodic nanotubular layer on the corrosion resistance of Ti grade 2. For instance, Hilario *et al.* reported an improvement in corrosion properties due to a decrease in the passive current density when compared to as-polished alloy, from potentials ranging from -0.03 to +1.5V versus OCP.^[12] On the other hand, Park *et al.*, which used the same electrolyte, a specifically prepared simulated body fluid solution, reported similar behaviours between non-anodized and anodized samples.^[19] The biggest difference between these two works is that Hilario *et al.* conducted their experiments at 37°C while Park *et al.* conducted them at room temperature.

Figure 5-9 shows representative potentiodynamic polarization curves of Ti grade 2 samples polished or anodized, and heat-treated in air atmosphere, overlapped to those of the non-heat-treated samples. In general, the heat treatment in air leads to a marked decrease of the overall passive current density and an increase of the E_{corr} . The heat-treated bare alloy presents two distinct passive zones: the first up to 1.3 V vs Ag/AgCl with a passive current density of about 10^{-8} A/cm² which corresponds to the behaviour of the thermal oxide layer and the second one up to 3 V which corresponds to the base alloy after breakdown of the thermal oxide. The effect of the thermal oxide present at the interface between nanotubes and the substrate is noticed also looking to the electrochemical behaviour of the anodized and air heat-treated samples. In this case the presence of the TNTs does not allow to clearly distinguish the contribution of each oxide layer and the transition from the first to the second passive zone is smoother. However, the sample presents a passive behaviour for the whole scanned potential range with the passive current density ranging from 10^{-6} to 10^{-7} A/cm². As described in 5.1.1 and 5.1.2, heat treatment in air leads to the formation of a thermal oxide, which is known to improve the corrosion resistance of non-anodized Ti.^[7] Similarly, heat treatment of anodized samples in air has also been described to improve their corrosion resistance in different works such as the ones of Hilario *et al.*, Park *et al.* and Mazare *et al.* ^[12,19,20] However, these works attribute the changes in the corrosion behavior to the changes in nanotube crystalline

structure, rather than the presence of a thermal oxide between the nanotubes and the substrate, as reported previously, even though they recognize it's existence.

Representative potentiodynamic polarization curves of Ti grade 2 bare and anodized samples after heat-treatment under vacuum conditions are reported in Figure 5-10, overlapped to those of the non-treated ones. The heat-treated bare substrate presents a very similar behaviour to the non-treated one. On the other hand, the heat treatment under vacuum strongly affects the corrosion resistance of the anodized alloy which presents an active behaviour with the anodic current density increasing almost linearly, even if at a low rate, with the applied potential. This could be probably attributed to a partial reduction of the oxide forming the passive film during heat treatment in vacuum as reported by Hyam et al.^[14] The native passive film can be quickly reformed on the surface of the bare Ti sample after exposure to the air, which could explained the similar behavior between annealed in vacuum and non-treated aspolished samples. For anodized samples, given that the nanotubes structure is not affected by the heat-treatment, the anodic layer could create a barrier that obstacles natural re-passivation.

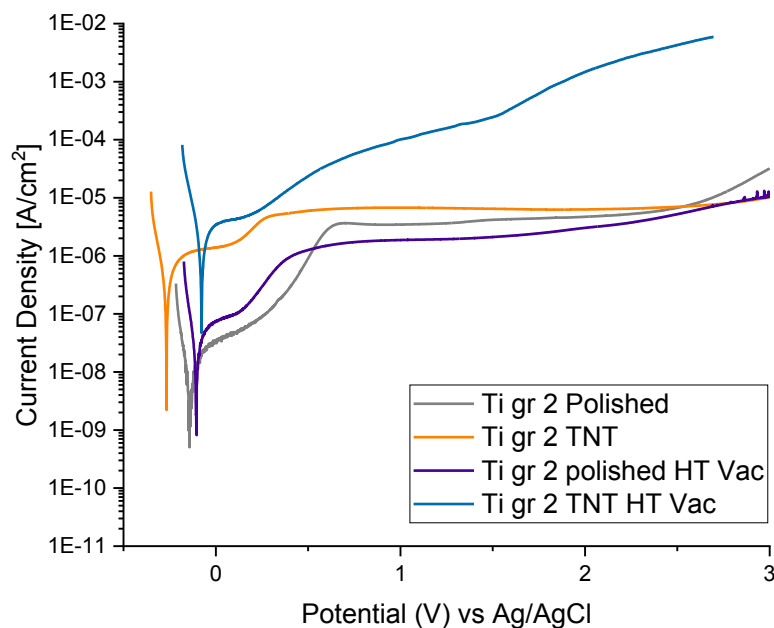


Figure 5-10: Representative potentiodynamic polarization curves of bare (Ti gr 2 polished) and anodized (Ti gr 2 TNT) Ti gr2 both prior and after heat treatment in vacuum in PBS solution.

5.2 Effect of anodization and heat-treatment on Ti grade 5 TNTs structure

5.2.1 Effect of heat treatment on bare samples

Figure 5-11 shows photographs and FESEM micrographs of as-polished Ti grade 5 samples heat treated both in air atmosphere and vacuum conditions at 500°C. From the photographs it is possible to see that the as-polished samples and the samples annealed in vacuum present a similar aspect, with a grey reflective aspect. On the other hand, the samples annealed in air present a copper-red color, however still reflexive. Comparing the low magnification FESEM micrographs of the as-polished and annealed in vacuum specimens, obtained in backscattered electron mode, the alloy microstructure can be better distinguished (fig. 5-11 A and B II). This is due to slight differences on the chemical composition of the surface oxide covering the different grains. The difference is much more intense on the annealed specimen indicating that the HT in vacuum modifies to some extent, at least the native passive film (probably partial reduction and reformation after exposure to the air).^[6] The different microstructure of the nanostructured oxide formed over different grains is more evident at high magnification (fig 5-11 CII and III) and the Ti6Al4V alloy grains are no more distinguishable. Also in this case the thermal oxide is composed by nanometric grains.

Figure 5-12 presents FESEM micrographs showing a cross-sectional view of the heat treated at 500°C in air Ti grade 5 samples. Similarly, to what was described previously in section 5.1.1 for Ti grade 2, these micrographs highlight the morphology of the produced thermal oxide layer which is quite compact, uniform and well adhered to the substrate, having a thickness of about 100 nm.

Figure 5-13 present X-ray diffractograms of the as-anodized Ti grade 5 sample and the samples heat-treated at 500°C, either in vacuum or in air atmosphere. Considering the biphasic structure of the alloy (see section 3.1.2), the identified Bragg peaks correspond to the α and β phases of the substrate (see 3.1.3) for the as-polished sample. The diffractograms of both heat-treated samples present the same peaks. No additional peaks corresponding to Ti oxide have been observed on none of the heat-treated samples. This indicates that the thermal oxide grown on the sample annealed in air atmosphere is probably amorphous.

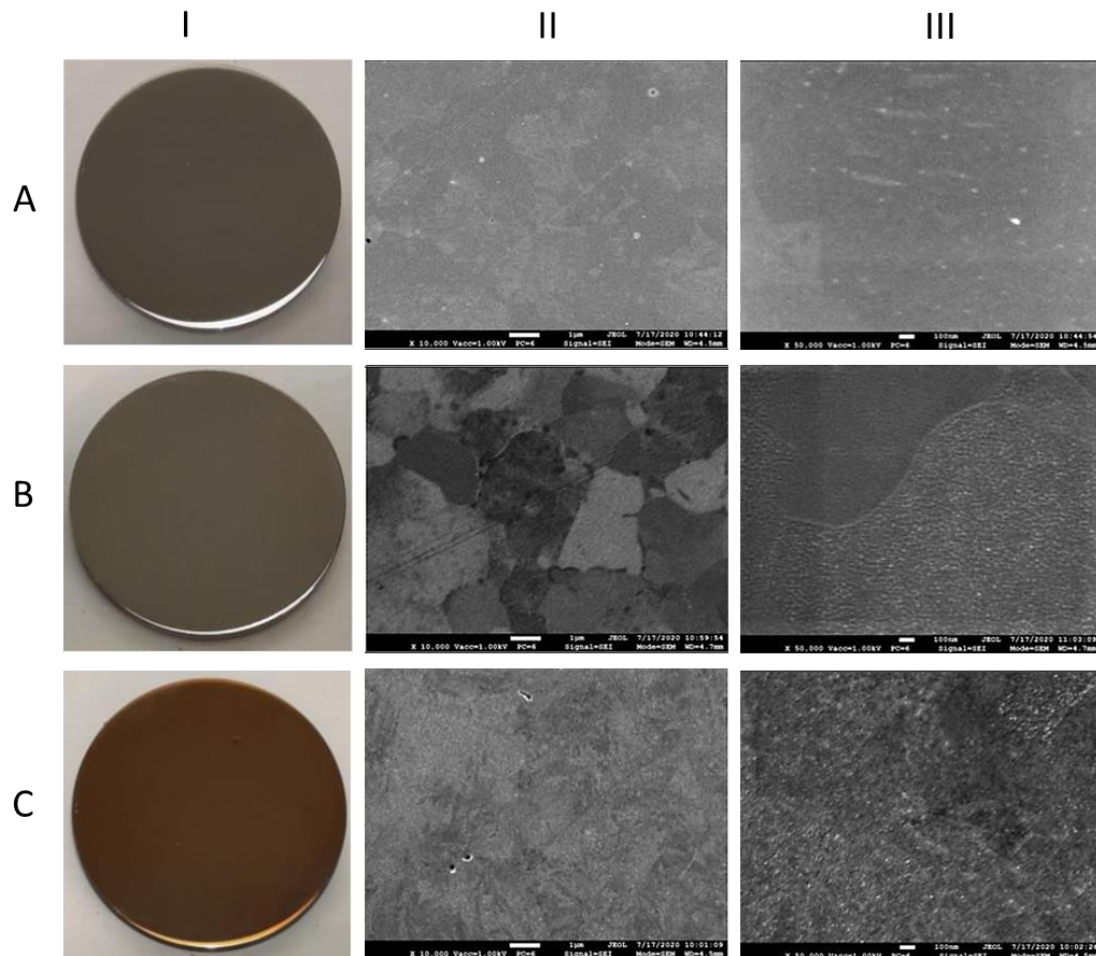


Figure 5-11: A top-view of as-polished Ti grade 5 (A), polished and annealed at 500°C for 3 h under vacuum conditions (B) or in air atmosphere (A). I-photographs; II - FESEM micrograph with a magnification of 10,000 ×; III - FESEM micrograph with a magnification of 50,000 ×.

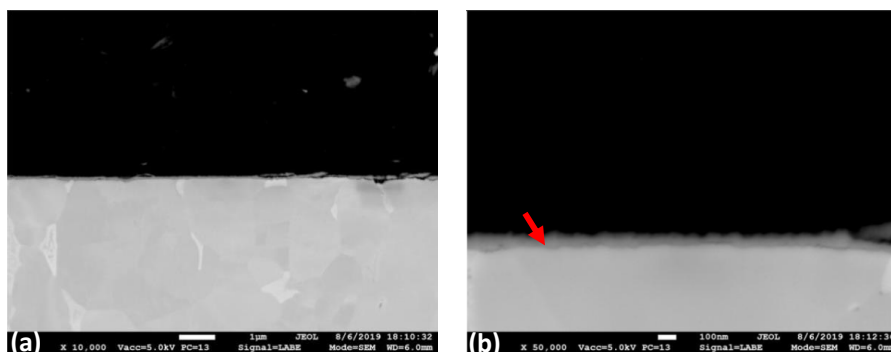


Figure 5-12: FESEM micrographs depicting at low (a) and high (b) magnification a cross section view of a polished Ti grade 5 annealed at 500°C for 3 h in air atmosphere. The red arrow indicates the thermal oxide layer.

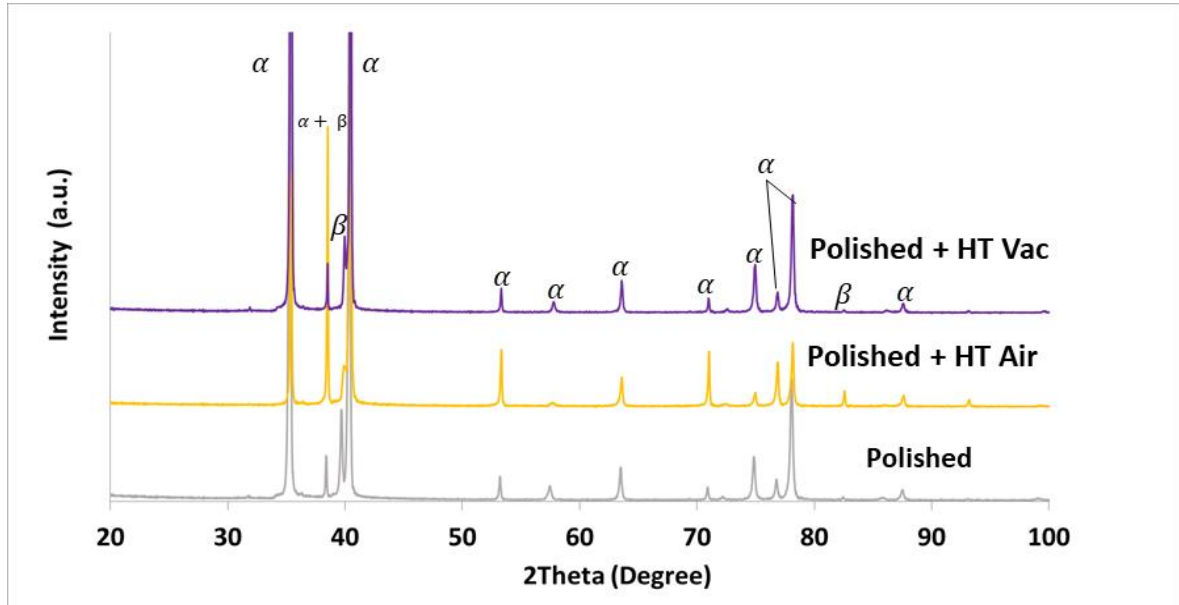


Figure 5-13: X-ray diffractograms of Ti grade 5 as-polished (Polished), and heat treated at 500°C for 3 h in air atmosphere (Polished+HT Air) or under vacuum (Polished+HT Vac). α : peaks corresponding to Ti α -phase; β : peaks corresponding to Ti β -phase.

As explained previously, thermal treatment in air leads to the formation of thermal oxide layer on the surface of the Ti alloy,^[7] while heat treatment performed in vacuum is reported to lead to reduction of the thin native TiO_2 layer.^[6] For this reason, and as reported for Ti grade 2 in section 5.1.1, the heat treated performed on vacuum did not lead to any visible difference in the morphology of the sample (with regard to the as-polished sample), while a brown thermal oxide was formed in the sample heat treated in air. The brown colour obtained for this thermal oxide, in contrast to light blue colour obtained for Ti grade 2, is unexpected. Velten *et al.* performed thermal treatment of both Cp-Ti and Ti6Al4V in temperature range between 400 to 600 °C in times ranging from 5 min to little above 8 h and reported similar light blue color in the oxide formed for both alloys.^[18] A possible explanation could be attributed to the different chemical composition of the produced thermal oxide (which for Ti grade 5, includes both Al_2O_3 and V_2O_5). Similarly, the differences in terms of crystalline structure could also be explained by the chemical composition of the produced oxide. While in section 5.1.1, the produced thermal oxide presented a rutile crystalline structure, the thermal oxide produced on Ti grade 5 seems to be amorphous. The presence of the Al alloying element (whose oxide, Al_2O_3 is present in the formed oxide film) could explain these differences observed between the two alloys. In this case, Al will play a similar role to that of a dopant on the oxide film, retarding oxide crystalline phase transition in such a way that the heat treatment at 500°C for 3 h is not

enough to promote the transition from an amorphous to anatase and then rutile phase of the oxide.

The inhibitory effect of aluminium in the anatase to rutile phase transition of TiO_2 and evolution has been described previously for bulk compact oxides.^[1] Moreover, it is generally believed that TiO_2 transition from amorphous to, first, anatase and then rutile.^[1,16] Thus, these results suggest, based on previous works, that the presence of aluminium inhibits the entire crystallization process. It is also important to take in consideration that V is a promoter of the anatase to rutile phase transition, but the higher amount of Al in the alloy results on a more predominant inhibitory effect.^[1]

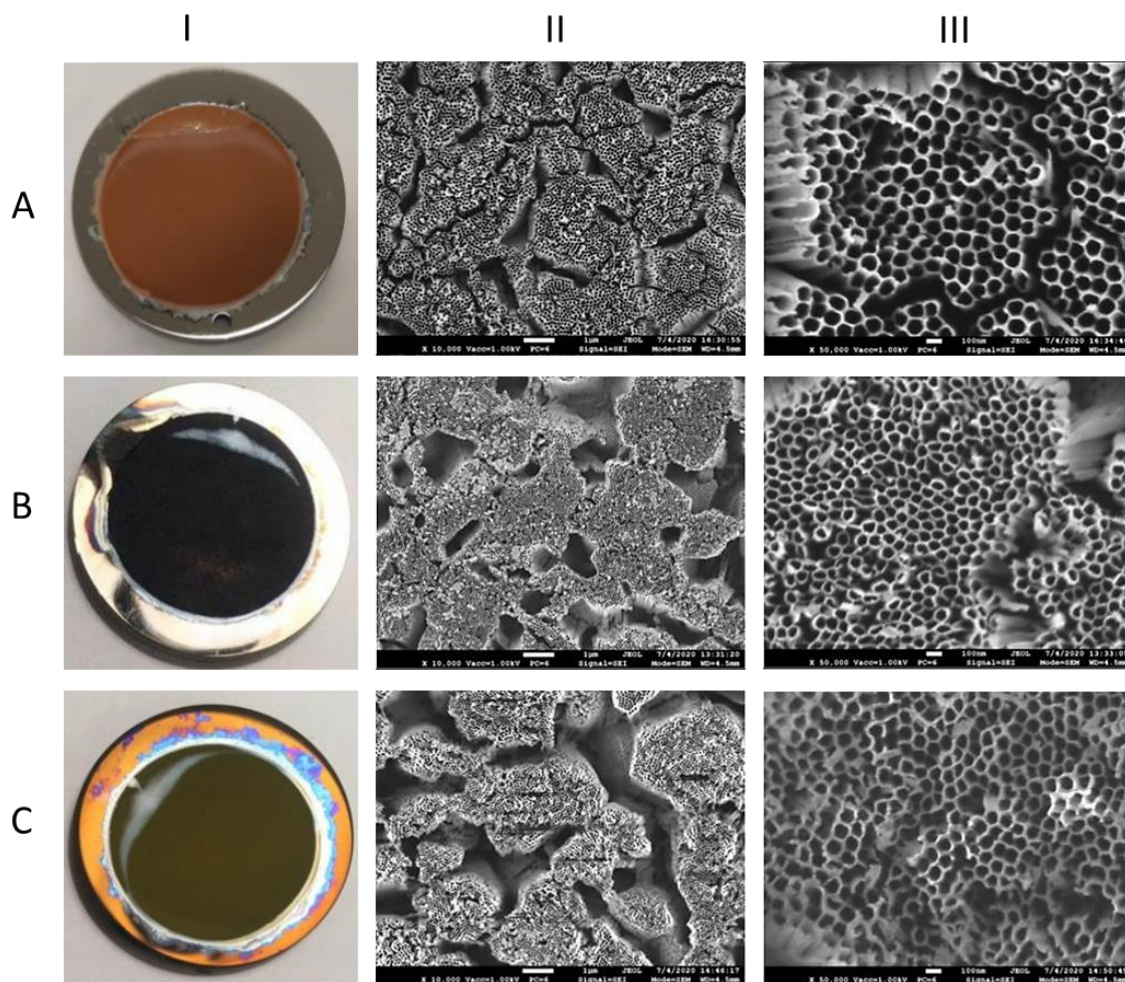


Figure 5-14: A top-view of as-polished Ti grade 5 (A), polished and annealed at 500°C for 3 h under vacuum conditions (B) in air atmosphere (C). I-photographs; II - low magnification FESEM micrograph; III-high magnification FESEM micrograph.

5.2.2 Effect of heat treatment on anodized samples

Figure 5-14 presents photographs and FESEM micrographs of Ti grade 5 samples anodized at 60 V and 1 h, as well as of the samples anodized in the same conditions and heat treated at 500°C for 3h in either air atmosphere or under vacuum conditions. From the photographs is possible to perceive that the as-anodized surface is opaque and with a brown colour, while the anodized surface annealed in air atmosphere presented olive green colour, also opaque. Moreover, the sample annealed under vacuum is black and also opaque. From the FESEM micrographs it is possible to see that, in spite the difference in colour, neither treatment leads to significant changes in the morphology of the produced nanotubes, either on the α or β phase.

This is in accordance with results previously described by different authors.^[2,3,10,16] It should be noted, furthermore, that the dual morphology is completely preserved, with both the honey-comb like morphology of the oxide grown over the α -phase, and the less well define tubular structure of the oxide grown over the β -phase being equally maintained, including the diameter dimensions described in figure 4-7 (see section 4.1.2). The only noticeable difference is a small thickening of the tube walls for the samples heat treated on air, as reported previously for Ti grade 2 (see section 5.1.2). However, it does not have a significant effect in the overall inner tube diameter.

Figure 5-15 show FESEM micrographs depicting a cross-sectional view of Ti grade 5 samples anodized at 60 V for 1 h and as well as anodized and heat treated in either vacuum conditions or air atmosphere. The low magnification micrographs (fig. 5-14 I) show that none of the heat treatments significantly modified the overall structure of the anodic oxide, growing differently over the α and β phases. Some detachments and imperfections better shown at the high magnification micrographs (fig. 5-14 II) could also in this case be produced during the metallographic preparation.

Similarly to what was previously described in Ti grade 2 (see section 5.1.2), the sample annealed in air atmosphere presents a compact oxide layer at the interface between the nanotubular layer and the substrate. It is, thus, possible to assume that, also in Ti grade 5 during the heat treatment in air, oxygen diffuses through the porous structure of the anodic oxide, leading to the thermal oxidation of the metal substrate, as described by Roy *et al.*^[15] The micrograph shows that the bottom of the tubes annealed in air is no longer distinguishable, as they are incorporated in the thermal oxide layer.

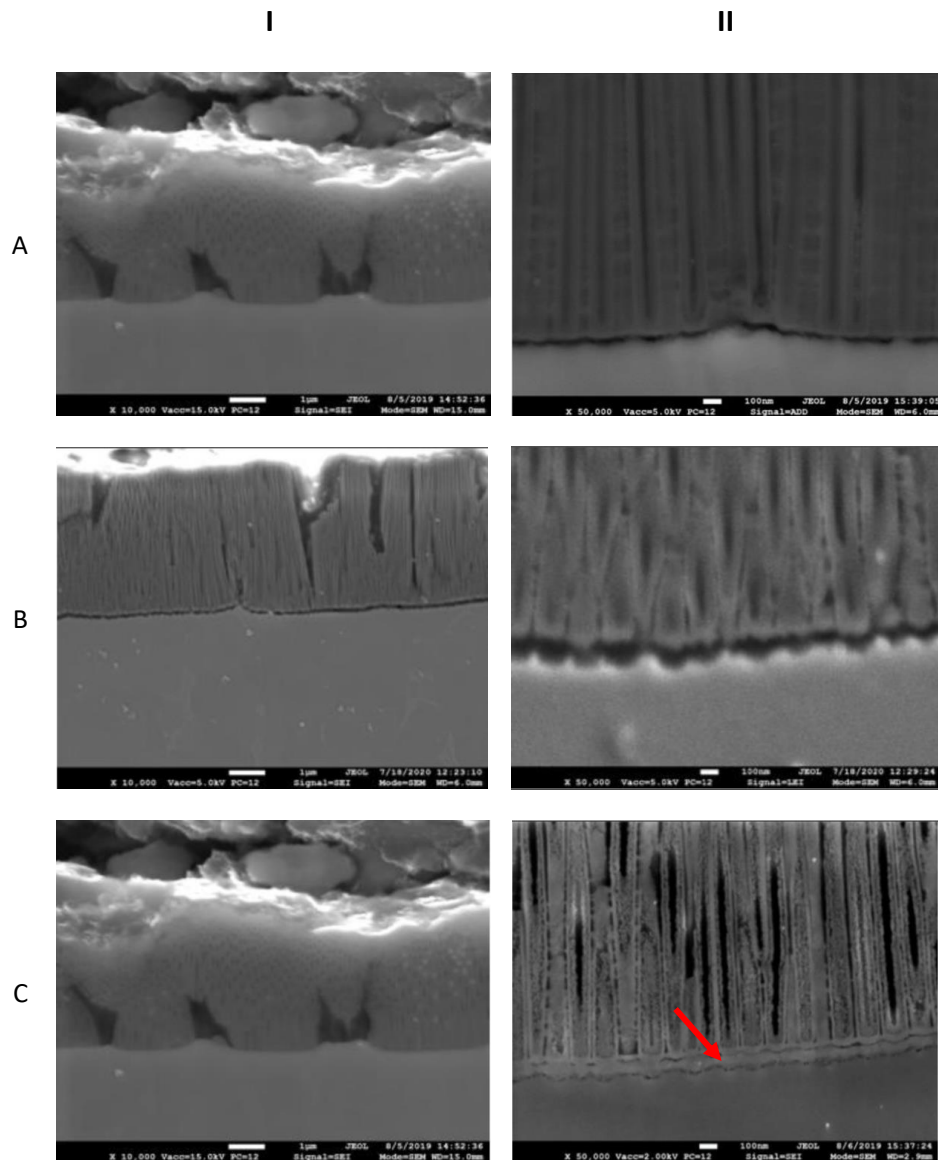


Figure 5-15: Cross section micrographs at different magnifications of the Ti grade 5 samples anodized at 60 V for 1 h prior (A) and after heat treatment at 500°C for 3 h either in vacuum (B) or in air atmosphere (C).

X-ray diffractograms of as-polished Ti grade 5 samples as well as Ti grade 5 anodized at 60 V for 1 h are reported in Figure 5-16. No significant differences can be observed comparing the two diffractograms, as all identified peaks correspond to the Ti grade 5 α and β phases. A magnification of the diffractograms at low angles after superposition of the lines is shown in Fig. 5-16 inset. A higher background intensity is observed for the anodized sample between 20° and 30°, where the principal peaks of TiO_2 (of both rutile and anatase structure) should appear. Similarly to the nanotubes produced over Ti grade

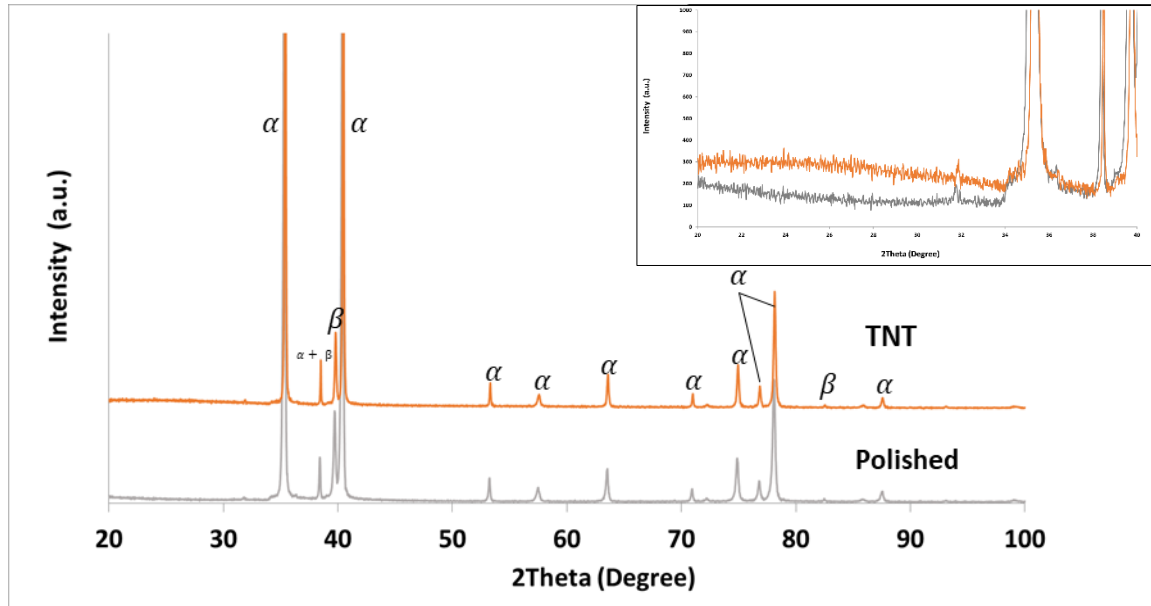


Figure 5-16: X-ray diffractograms of Ti grade 5 as-polished(Polished) and anodized at 60 V for 1 h (TNT). Inset; magnification of superimposed diffractograms at low angles. α : peaks corresponding to Ti α -phase; β : peaks corresponding to Ti β -phase.

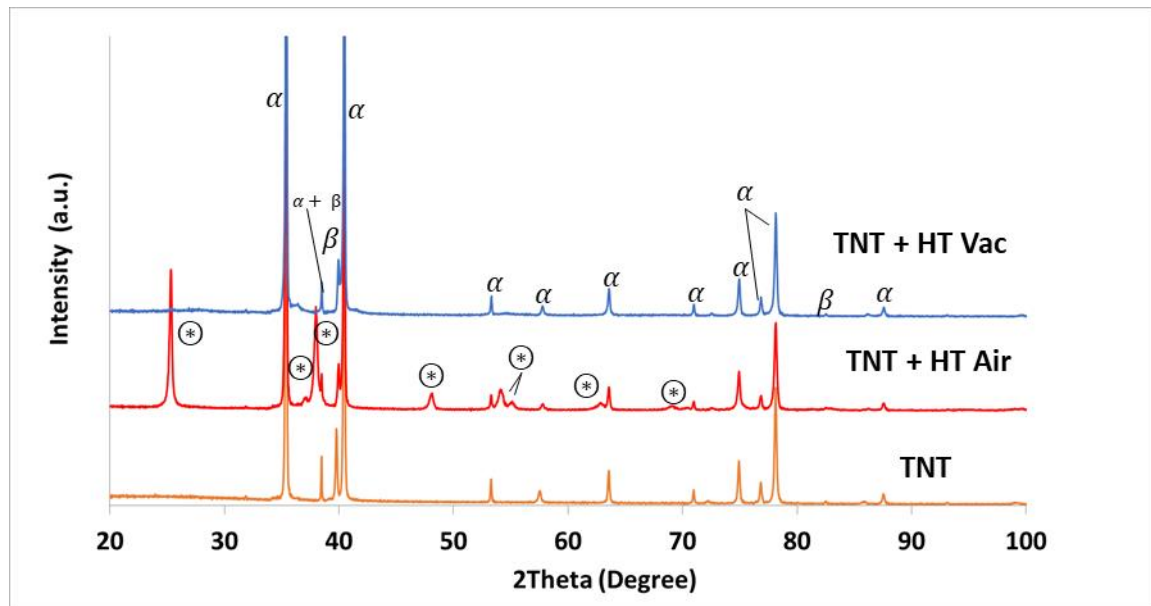


Figure 5-17: X-ray diffractograms of Ti grade 2 as-polished(Polished), anodized at 40 V for 6 h (TNT), and heat-treated post-anodization at 500°C for 3h in air atmosphere (TNT+HT Air) or under vacuum (TNT+HT Vac). α : peaks corresponding to Ti α -phase; β : peaks corresponding to Ti β -phase. \odot : peaks corresponding to anatase TiO_2 .

2 (see section 5.1.2), these results indicate that the produced nanotubes are amorphous, which is in accordance with the existing literature.

Figure 5-17 presents X-ray diffractograms of Ti grade 5 samples anodized at 60 V for 1 h as well as samples anodized and heat treated at 500°C for 3 h in either air atmosphere or vacuum conditions. All diffractograms present the same Bragg peaks corresponding to Ti6Al4V α and β phases. Additional peaks appear only on the diffractogram of the specimen annealed in air atmosphere and they all correspond to the TiO₂ anatase phase. In contrast to the results reported for Ti gr 2 (see section 5.1.2), in Ti grade 5 only the heat treatment in air atmosphere leads to the TNTs recrystallization to anatase phase and no rutile peaks are observed. The ones heat treated under vacuum conditions remain amorphous.

These difference between the two alloys, could be attributed, as discussed in the previous section, to the inhibitory effect of Al the alloying element and, consequently, of Al₂O₃ on the oxide.^[1] The same inhibitory effect of Al has been also described for nanoporous titania anodic oxides by Bayata and Ürgen. In this work, the authors observed that, in the Al-doped TiO₂, the transition from amorphous to anatase only began to take place at temperatures of about 420 °C, while for undoped TiO₂, it began at 280°C as reported first by Verghese *et al.*^[9], and as such its presence has an overall retarding effect on the crystallization of the TiO₂ nanostructure.^[21] On the other hand, the report of Hyam *et al.* states that neutral annealing environments such as vacuum can also have an overall retarding effect on the crystallization process, based on inferior anatase crystallite sizes and absence of rutile peaks on the X-ray diffractograms, for the samples heat treated in vacuum (when compared to the ones heat treated in air or oxygen-only containing atmospheres). However, these authors did not consider the role of the crystallinity of the thermal oxide formed in air atmosphere in their XRD measurements. Thus, although it is not impossible that the vacuum environment has some sort of contribution, it is highly likely that the rutile phase measured on TNTs grown on Ti grade 2, and absent on the heat treated nanotubes of Ti grade 5, is exclusively related to the formation of this thermal oxide, and not to a small crystallization on the anodic layer, inspite of the considerations of the role of the substrate defended by Fang *et al.*^[16]

5.2.3 Effect of anodization and heat treatment on corrosion resistance

Representative potentiodynamic polarization curves obtained on Ti grade 5 samples, as-polished and anodized at 60 V for 1 h in PBS, according to the procedure described in section 2.6, are reported in Figure 5-17. The as-polished Ti grade 5 exhibits a

wide passive range with a current density of about 6×10^{-6} A/cm² and a E_{corr} of approximately -0.31 V vs Ag/AgCl. Anodization leads to an increase of the corrosion potential up to 0.14 V vs Ag/AgCl and a decrease of the passive current density which reaches values of about 9×10^{-7} A/cm², at low potentials, and gradually increases to reach values of the bare sample for potentials over 1 V vs Ag/AgCl. Similarly to Ti grade 2 (see section 5.1.3), and as described in section 1.1.2, Ti grade 5 is shown to be resistant to corrosion in physiological environments, as is evidenced by the wide passive range and low passive current densities. Regarding the effect of anodization, even though there seems to be a slight improvement in the corrosion behaviour, due to a more positive corrosion potential and lower passive current densities for low potentials, the overall behaviour of anodized and not anodized samples is quite similar, with both possessing a wide passive range and, for most of it, similar passive current densities. This is in line with the results obtained for Ti grade 2 (see section 5.1.3) and, similarly, there is some disagreement in literature regarding the effect of nanotubes on the corrosion resistance of the alloys. For instance, the work of Rossi *et al.* reports that anodization has no effect on corrosion resistance even though there is a slightly higher corrosion potential, while Lario *et al.*, who used a NaCl solution as electrolyte instead of PBS, reported a marked improvement with lower passive current densities. [22,23]

Figure 5-18 shows representative potentiodynamic polarization curves of Ti grade 5 samples, as-polished and anodized, after heat treatment in air atmosphere, overlapped to those of the non-heat treated samples. For both types of samples the heat treatment lead to an increase in E_{corr} of approximately + 200 mV, to about -0.13 V vs Ag/AgCl in both samples and to a breakdown of the passive film at around 1.2-1.3 V vs Ag/AgCl. Other than that, the heat-treated as-polished samples present a passive zone with a current density of about 10^{-7} A/cm², while the anodized and heat-treated sample presents a passive current density which is almost two orders of magnitude higher with respect to the bare heat-treated alloy. Considering the results described in the previous section, the breakdown of the passive film seems to be an inherent characteristic of the thermal oxide that is formed on both samples. This is a stark contrast to the behaviour of the Ti grade 2 heat-treated in air (see section 5.1.3), which overall presented a marked improvement on corrosion resistance, with lower passive current density registered for the entire potential scan range. This difference in behaviour between the two alloys could be attributed to the difference in both the chemical composition and structure of the thermal oxide, which contains Al₂O₃ and V₂O₅ and is amorphous on Ti grade 5. [24]

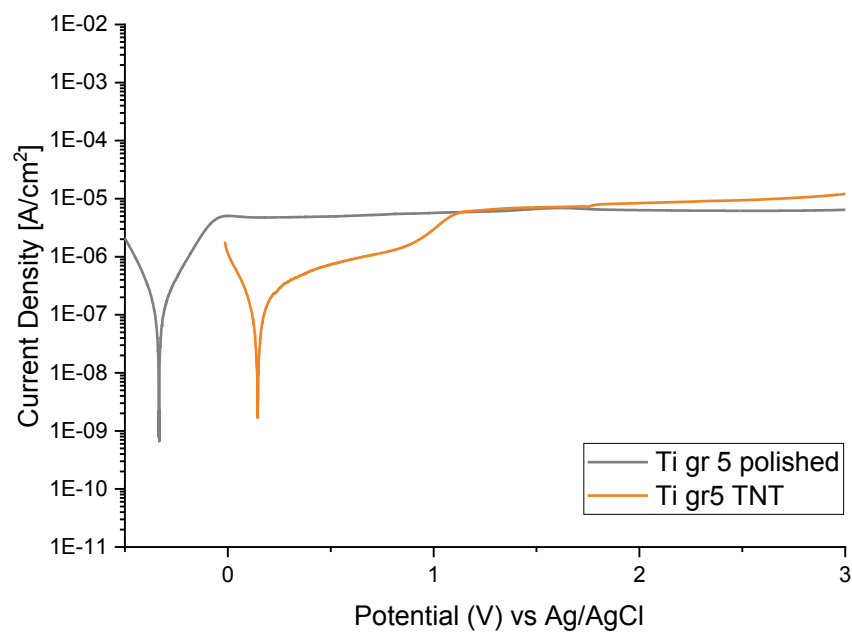


Figure 5-17: Representative potentiodynamic polarization curves of bare (Ti gr 5 polished) and anodized (Ti gr 5 TNT) Ti gr. 5 in PBS.

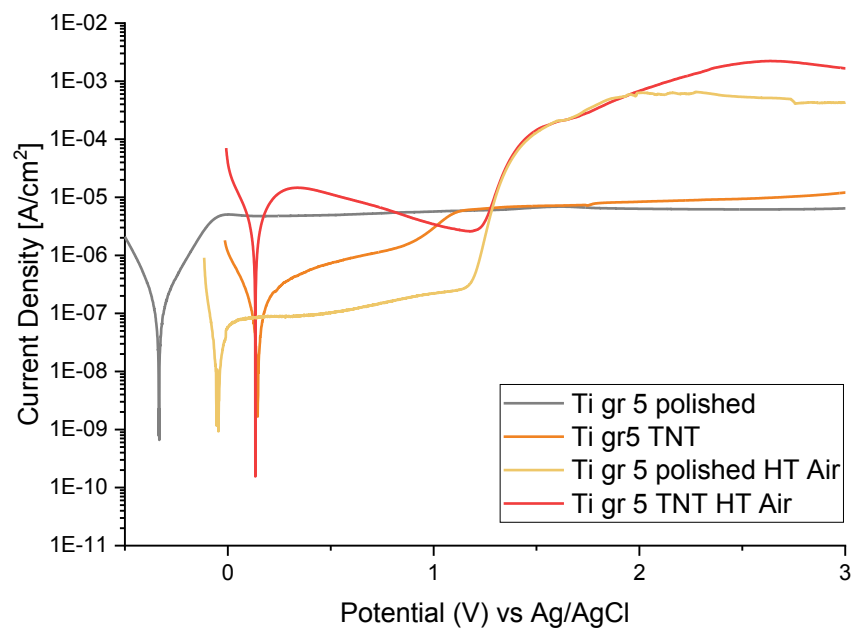


Figure 5-18 Representative potentiodynamic polarization curves of bare (Ti gr 5 polished) and anodized (Ti gr 5 TNT) Ti gr.5 both prior and after heat treatment in air atmosphere in PBS.

Representative potentiodynamic polarization curves of Ti grade 5 samples, bare and anodized, after heat treatment under vacuum conditions are reported in Figure 5-19, overlapped to those of the non-treated samples. The bare heat-treated sample presents a slightly higher E_{corr} and a lower passive current density compared to the non-treated one. This is a stark contrast to the behaviour of as-polished Ti grade 2 samples, also heat treated in vacuum, which presented a similar behaviour. This difference in behaviour could be attributed to the difference in chemical composition of the alloy after reduction (due to vacuum treatment) and posterior re-passivation upon contact with air. On the other hand, the heat treatment under vacuum strongly affects the corrosion behaviour of the anodized samples. Also in this case, as was observed for Ti grade 2, an active behaviour is observed with continuously increasing anodic current density by increasing the applied potential. As described previously, it is known the vacuum environment, during the annealing process leads to partial reduction of the oxide, and the presence of the nanotubular layer can be an obstacle that hinders the re-passivation that is thought to occur with the as-polished sample. ^[14]

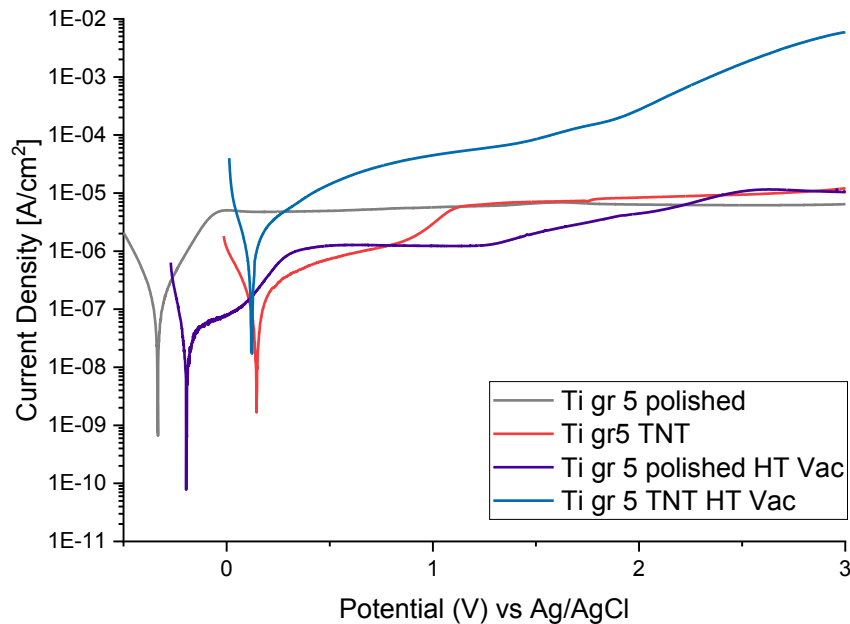


Figure 5-19: Representative potentiodynamic polarization curves of bare (Ti gr 5 polished) and anodized (Ti gr 5 TNT) Ti gr.5 both prior and after heat treatment in vacuum in PBS solution.

5.3 Partial conclusions

As expected, for both alloys, the as-formed TNTs were amorphous and a heat-treatment at 500°C, in air atmosphere, led to crystallization of the anodic oxide into an anatase phase, but the Ti grade 2 sample also presented some degree of crystallization into rutile. On the other hand, a heat treatment at 500°C under vacuum conditions lead to the recrystallization of the anodic oxide over Ti gr.2 to anatase phase but did not affect the one grown over Ti gr.5. Moreover, for both alloys, H.T. in air leads to the formation of a thermal oxide at the substrate-TNTs interface which is composed by rutile over Ti gr.2 but is amorphous when formed over Ti gr.5. These differences in behaviour could be attributed to the presence of Al_2O_3 on the oxide formed on Ti grade 5, which is known to an inhibitor of the transition of anatase to rutile crystalline phase. ^[1,21]

Regarding corrosion resistance, the nanotube growth does not hinder the corrosion resistance of either alloy. Following heat treatment in air, the corrosion behavior seems to be governed by the type of oxide present at the substrate-TNTs interface after H.T. Indeed, the anodized air heat treated Ti gr. 2 samples present a passive behavior for the whole scanned potential range and lower passive current densities with respect to the non-heat treated alloy, proving the higher electrochemical stability of the rutile thermal oxide formed at the interface. On the other hand, the thermal oxide formed over the Ti gr.5 leads to an anticipated breakdown at 1.2V vs Ag/AgCl. Nevertheless in the human body potential range, a heat treatment in air atmosphere lowers the passive current for both anodized alloys and does not compromise their excellent corrosion resistance.

However, when the same heat treatment was performed under vacuum conditions the corrosion resistance of both anodized alloys was strongly affected. An active behaviour was observed in both cases with an increasing anodic current density by increasing the applied potential even if at a low rate. This could be attributed to the reduction of the oxide and oxygen removal due to the vacuum conditions.

Taking in consideration all the above and the purpose of this work, it was decided to proceed performing the heat treatment of the anodized layers in air as it allows the recrystallization of the TNTs into a more biocompatible anatase phase and does not hinder their performance in the human body environment in terms of corrosion.

5.4 Bibliography

1. Hanaor DAH, Sorrell CC. Review of the anatase to rutile phase transformation. *J Mater Sci* 2011;**46**:855–74.
2. Roy P, Berger S, Schmuki P. TiO₂ nanotubes: Synthesis and applications. *Angew Chemie - Int Ed* 2011;**50**:2904–39.
3. Kowalski D, Kim D, Schmuki P. TiO₂ nanotubes, nanochannels and mesosponge: Self-organized formation and applications. *Nano Today* 2013;**8**:235–64.
4. Regonini D, Bowen CR, Jaroenworarluck A *et al.* A review of growth mechanism, structure and crystallinity of anodized TiO₂ nanotubes. *Mater Sci Eng R Reports* 2013;**74**:377–406.
5. Indira K, Mudali UK, Nishimura T *et al.* A Review on TiO₂ Nanotubes: Influence of Anodization Parameters, Formation Mechanism, Properties, Corrosion Behavior, and Biomedical Applications. *J Bio- Tribo-Corrosion* 2015;**1**:1–22.
6. Guillemot F, Porté MC, Labrugère C *et al.* Ti⁴⁺ to Ti³⁺ conversion of TiO₂ uppermost layer by low-temperature vacuum annealing: Interest for titanium biomedical applications. *J Colloid Interface Sci* 2002;**255**:75–8.
7. Jamesh M, Sankara Narayanan TSN, Chu PK. Thermal oxidation of titanium: Evaluation of corrosion resistance as a function of cooling rate. *Mater Chem Phys* 2013;**138**:565–72.
8. Regonini D, Satka A, Jaroenworarluck A *et al.* Factors influencing surface morphology of anodized TiO₂ nanotubes. *Electrochim Acta* 2012;**74**:244–53.
9. Varghese OK, Gong D, Paulose M *et al.* Crystallization and high-temperature structural stability of titanium oxide nanotube arrays. *J Mater Res* 2003;**18**:156–65.
10. Jaroenworarluck A, Regonini D, Bowen CR *et al.* A microscopy study of the effect of heat treatment on the structure and properties of anodised TiO₂ nanotubes. *Appl Surf Sci* 2010;**256**:2672–9.
11. Regonini D, Jaroenworarluck A, Stevens R *et al.* Effect of heat treatment on the properties and structure of TiO₂ nanotubes: Phase composition and chemical composition. *Surf Interface Anal* 2010;**42**:139–44.
12. Hilario F, Roche V, Nogueira RP *et al.* Influence of morphology and crystalline structure of TiO₂ nanotubes on their electrochemical properties and apatite-forming ability. *Electrochim Acta* 2017;**245**:337–49.
13. Indira K, Kamachi Mudali U, Rajendran N. Corrosion behavior of electrochemically assembled nanoporous titania for biomedical applications. *Ceram Int* 2013;**39**:959–67.
14. Hyam RS, Lee J, Cho E *et al.* Effect of annealing environments on self-organized TiO₂ nanotubes for efficient photocatalytic applications. *J Nanosci Nanotechnol* 2012;**12**:8908–12.
15. Roy P, Kim D, Lee K *et al.* TiO₂ nanotubes and their application in dye-sensitized solar cells. *Nanoscale* 2010;**2**:45–59.
16. Fang D, Luo Z, Huang K *et al.* Effect of heat treatment on morphology, crystalline structure and photocatalysis properties of TiO₂ nanotubes on Ti substrate and freestanding membrane. *Appl Surf Sci* 2011;**257**:6451–61.

17. Das S, Zazpe R, Prikryl J *et al.* Influence of annealing temperatures on the properties of low aspect-ratio TiO₂ nanotube layers. *Electrochim Acta* 2016;**213**:452–9.
18. Velten D, Biehl V, Aubertin F *et al.* Preparation of TiO₂ layers on cp-Ti and Ti6Al4V by thermal and anodic oxidation and by sol-gel coating techniques and their characterization. *J Biomed Mater Res* 2002;**59**:18–28.
19. Park HH, Park IS, Kim KS *et al.* Bioactive and electrochemical characterization of TiO₂ nanotubes on titanium via anodic oxidation. *Electrochim Acta* 2010;**55**:6109–14.
20. Mazare A, Totea G, Burnei C *et al.* Corrosion, antibacterial activity and haemocompatibility of TiO₂ nanotubes as a function of their annealing temperature. *Corros Sci* 2016;**103**:215–22.
21. Bayata F, Ürgen M. Role of aluminum doping on phase transformations in nanoporous titania anodic oxides. *J Alloys Compd* 2015;**646**:719–26.
22. Rossi S, Volgare L, Perrin-Pellegrino C *et al.* Dual electrochemical treatments to improve properties of Ti6Al4V alloy. *Materials (Basel)* 2020;**13**:1–16.
23. Lario J, Viera M, Vicente Á *et al.* Corrosion behaviour of Ti6Al4V ELI nanotubes for biomedical applications. *J Mater Res Technol* 2019;**8**:5548–56.
24. García-Alonso MC, Saldaña L, Vallés G *et al.* In vitro corrosion behaviour and osteoblast response of thermally oxidised Ti6Al4V alloy. *Biomaterials* 2003;**24**:19–26.

6 ANTIMICROBIAL FUNCTIONALIZATION

This chapter focuses on the antimicrobial decoration/functionalization of the previously produced TiO₂ nanotubes over the Ti6Al4V alloys. For this purpose, were chosen the most common inorganic antimicrobial agents silver (Ag), zinc (Zn) and copper (Cu). The aim of this work is to decorate the TNTs with either Zn, Cu or Ag nanoparticles, at low amounts, without altering the TNTs morphology and to obtain an as uniform as possible distribution of these particles over the whole surface. This work comprises the following activities:

- Decoration/functionalization of TNTs with Ag through an electroless deposition process.
- Decoration/functionalization of TNTs with Zn or Cu through electrodeposition processes.
- In vitro testing of antimicrobial effect of the produced surface modifications against *Staphylococcus. epidermidis* (ATCC 35984) one of the most common strains in medical device related infections and, only of TNTs with Ag, against MG63 human osteosarcoma cells, to test biocompatibility.

Based on the previous results, the decoration/functionalization was performed on Ti6Al4V anodized at 60 V for 1 h and heat treated at 500°C for 3 h in air atmosphere. The samples were evaluated through FESEM, EDXS. Antimicrobial activity was assessed by determination of viable colonies formation units (CFU), and biocompatibility by lactate dehydrogenase test (LDH).

6.1 Electrodeposition of Zn and Cu

Fig. 6-1 shows a cyclic voltammogram (C-V) obtained in 3.2mM Zn(NO₃)₂ in a three electrode system using heat treated TNTs as working electrode, Pt as counter and Ag/AgCl as reference electrode. The potential was scanned from -2 to 1.5 V vs Ag/AgCl at a scan rate of 0.1 V/s. From the CV curve, the reduction peak at about -1 V vs Ag/AgCl was identified as the reduction peak of Zn²⁺ to Zn. Based on this potential of -1.6 V vs Ag/AgCl was chosen as deposition potential for Zn to ensure Zn growth. For process optimization, different experimental parameters were tested, including deposition time (1, 3, 5, 10, 15 and 30 min),

different agitation conditions (no agitation, or ultrasound) and different temperatures (room temperature around 25°C, or high temperatures at around 70°C).

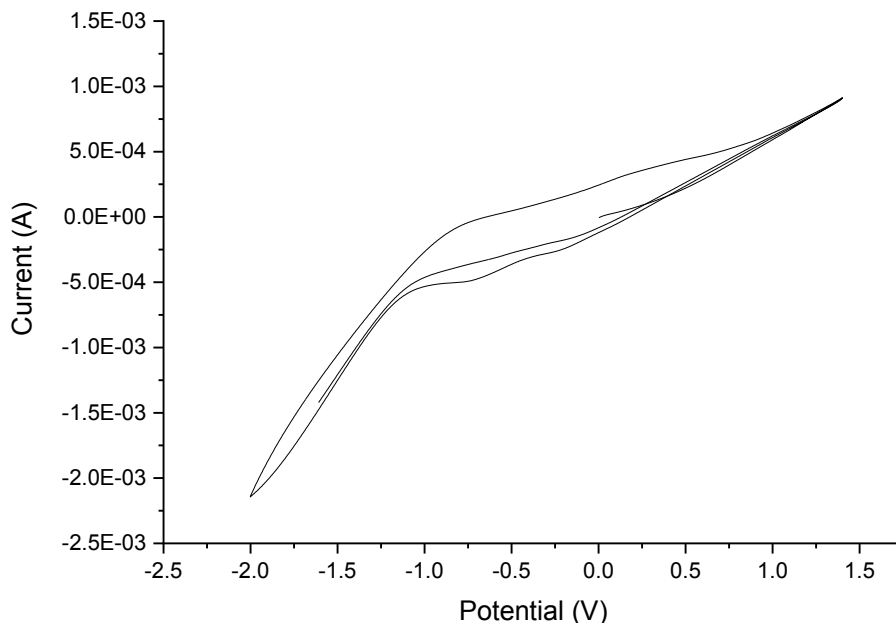


Figure 6-1: Cyclic voltamograms in 3.2 mM $\text{Zn}(\text{NO}_3)_2$ on anodized Ti6Al4V samples.

For deposition times inferior to 10 min, no deposited zinc was detected. For 10, 15 and 30 min of deposition, the amount of deposited Zn was very similar, approximately 4.73 ± 0.15 wt.%, 4.83 ± 0.2 wt.%, and 3.9 ± 0.05 wt.% respectively, measured by EDXS on the surface of the TNTs over a $10 \times 10 \mu\text{m}$ area. The values listed are the mean values of 15 independent EDXS measurements. Figure 6-2 shows FESEM micrographs depicting the morphology of Zn crystals deposited on the TiO_2 nanotubular layers for different deposition times. After 10 min deposition time, the low magnification micrograph shows that the deposited zinc is not uniformly distributed (Figure 6-2 A I), with the high magnification micrographs showing that ZnNPs are concentrated in clusters accumulated on the nanotube tops (Figure 6-2 A II). The increase in deposition time to 15 min, leads to a more uniform distribution over the surface (Figure 6-2 B I), with individualized Zn nanoparticles of similar diameter grown on the tube tops (Figure 6-2 B II). A further increase in time to 30 min of deposition, led to a similar morphology (Figure 6-2 C I and II). Thus, a deposition time of 15 min was selected for further experiments.

Figure 6-3 shows the effect of ultrasounds (Fig. 6-3 B) and temperature (Fig. 6-3 C) on the deposition of Zn/ZnO on TNTs. The application of ultrasounds the electrochemical process, led to the deposition of a much higher amount of zinc (35.09 ± 0.2 wt.%). Contrary to the sample deposited without ultrasounds, no ZnNPs are formed on the top of the tubes.

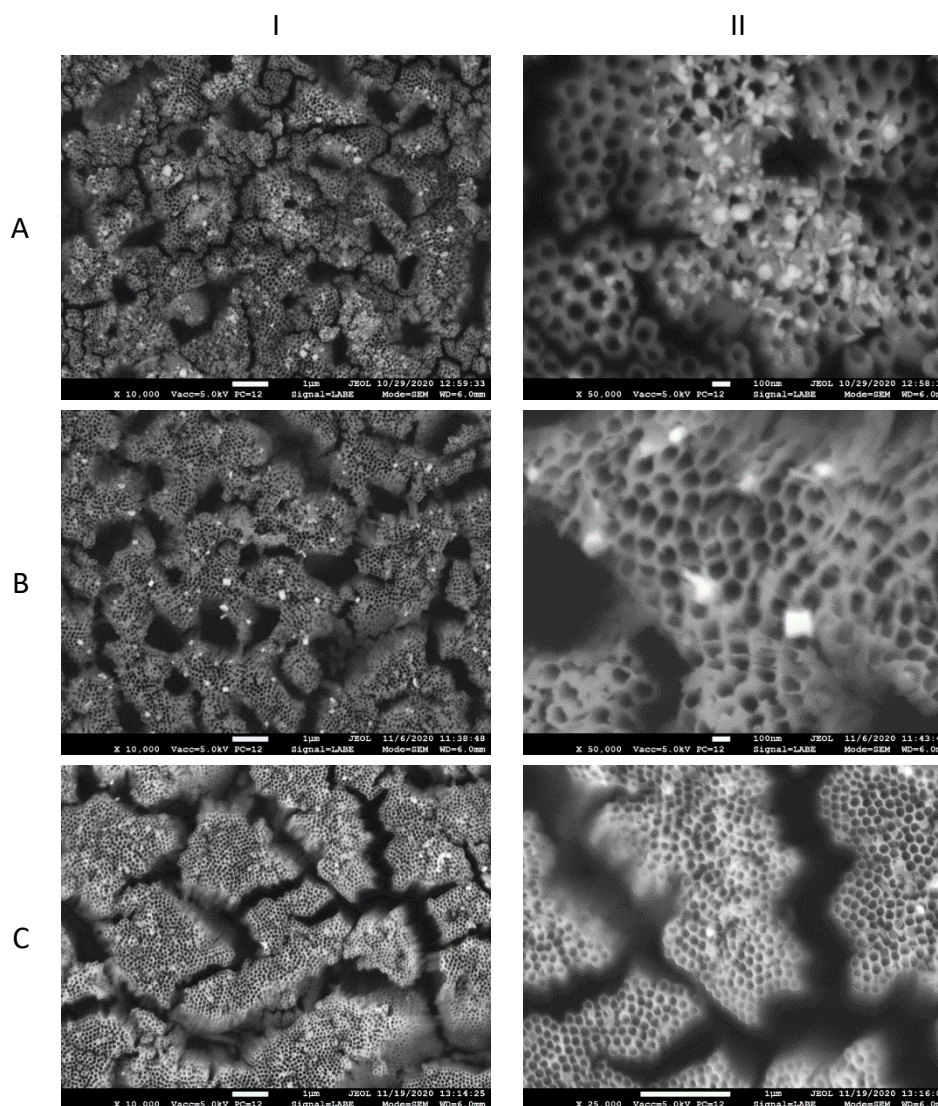


Figure 6-2: FESEM micrographs, at low (I) and high magnification (II), of TNTs after electrochemical deposition of ZnNPs for 10 min (A), 15 min (B) and 30 min (C).

Instead, the top of the anodized layers is completely covered by a zinc oxide/hydroxides (Fig 6-3 BI) that accumulates on the tube tops (Fig. 6-3 BII) and tubular morphology was lost. High temperatures superior to 50°C should prevent the formation of $\text{Zn}(\text{OH})_4^{2-}$ and promote the deposition of single ZnO crystals on top of the tubes.^[1] The increase in temperature to

70°C however, led to a non-uniform distribution of Zn, with crystallites forming in specific zones of the samples as evidenced by the low magnification micrographs (Fig. 6-3 CI). A closer look at these zones (Fig. 6-3 CII) shows that Zn oxides are that grown on the top of the tube, and the tubular morphology is lost. Thus, based on these results, the deposition of Zn/ZnO on TiO₂ nanotubes with was performed at room temperature, without mixing, for 15 min.

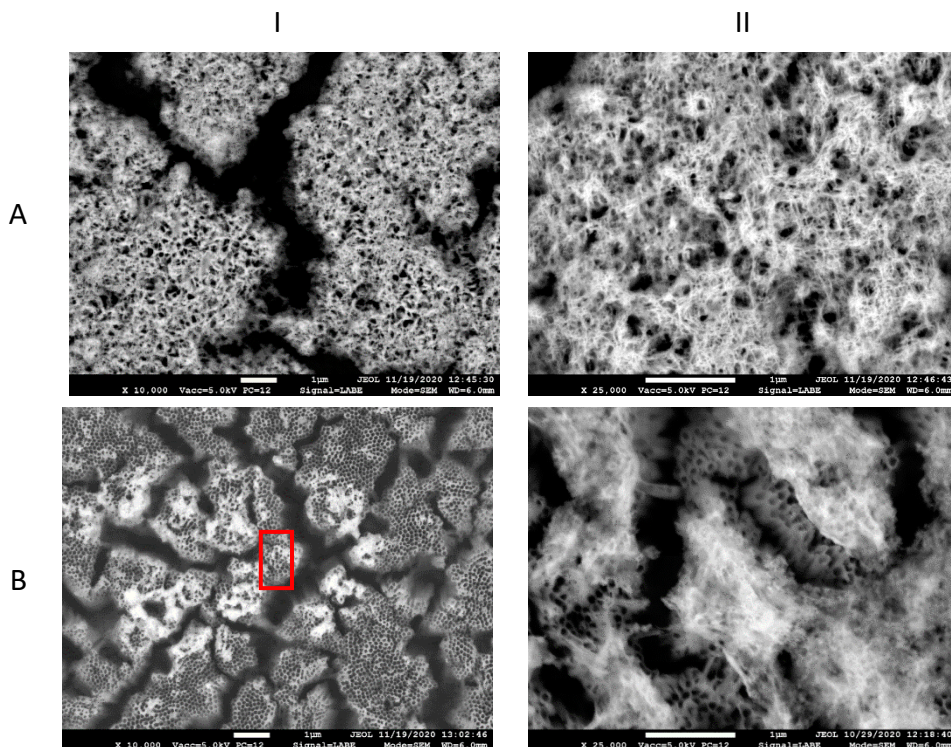


Figure 6-3: FESEM micrographs, at low (I) and high magnification (II), of TNTs after electrochemical deposition of ZnNPs for 15 min, in ultrasound at room temperature (B) or with no mixing at 70°C (C). The high magnification image C II is taken in the zone highlighted by the red frame.

Fig. 6-4 shows cyclic voltammogram (C-V) curves for the electrodeposition of Cu on heat treated TNTs, at a scan rate of 0.1 V.s⁻¹ and a potential ranging from -2.0 V to 0.5 V, in a 3.2 mM CuSO₄ solution acidified at pH 2 with H₂SO₄, in a three electrode system using a heat treated TNTs as working electrode, Pt as counter electrode and Ag/AgCl as reference electrode with a scan rate of 0.1 V/s. Two reduction peaks can be distinguished, one at about -0.36 V vs Ag/AgCl and a second one at about -0.8 V vs Ag/AgCl. For this reason, different attempts have been done to deposit Cu at -0.6, -0.8 and -1 V vs vs Ag/AgCl for 90 s.

The amount of deposited Cu has been estimated through EDXS analyses on the top surface of the TNTs over a $10 \times 10 \mu\text{m}$ area. No Cu nucleation was observed for the deposition preformed at -0.6 V vs Ag/AgCl. The revealed amount of Cu for the specimen polarized at -0.8 V vs Ag/AgCl was of $1.3 \pm 0.1 \text{ wt.}\%$ while for the one polarized at -1 V vs Ag/AgCl was of about $4.06 \pm 0.31 \text{ wt.}\%$. However, no Cu nanoparticles were visible on the sample polarized at -0.8 V vs Ag/AgCl (not pictured), while the sample anodized at -1 V vs Ag/AgCl present the formation of nano clusters of Cu, with a diameter of approximately 250 nm , on the top of the tubes (Figure 6-5 AI and AII). A longer deposition of 180s was performed at -1 V vs Ag/AgCl, with or without ultrasounds (Figure 6-5 B and C). Both the increase in time, and the use of in ultrasounds led to an increase in the amount of deposited Cu ($7 \pm 0.7 \text{ wt.}\%$ and $22.8 \pm 5.5 \text{ wt.}\%$). While an increase in deposition time led only to higher amount of Cu clusters of the same dimension, on the top of the tubes, ultrasounds led to the formation of bigger clusters and a much higher amount of deposited Cu. As such, a deposition at -1 V vs Ag/AgCl, for 180 s (Fig. 6-5 B) was chosen for antimicrobial tests.

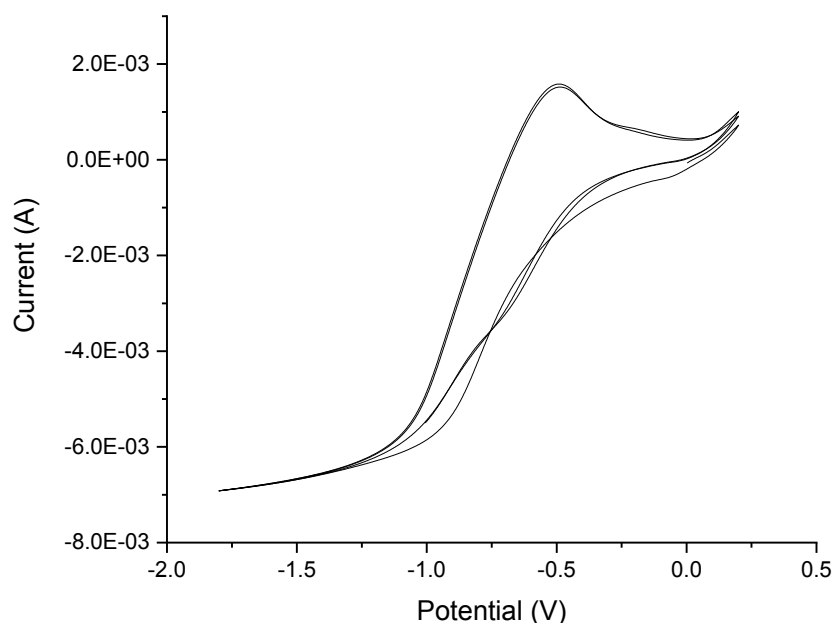


Figure 6-4: Cyclic voltammogram of deposited Cu on anodized Ti6Al4V samples.

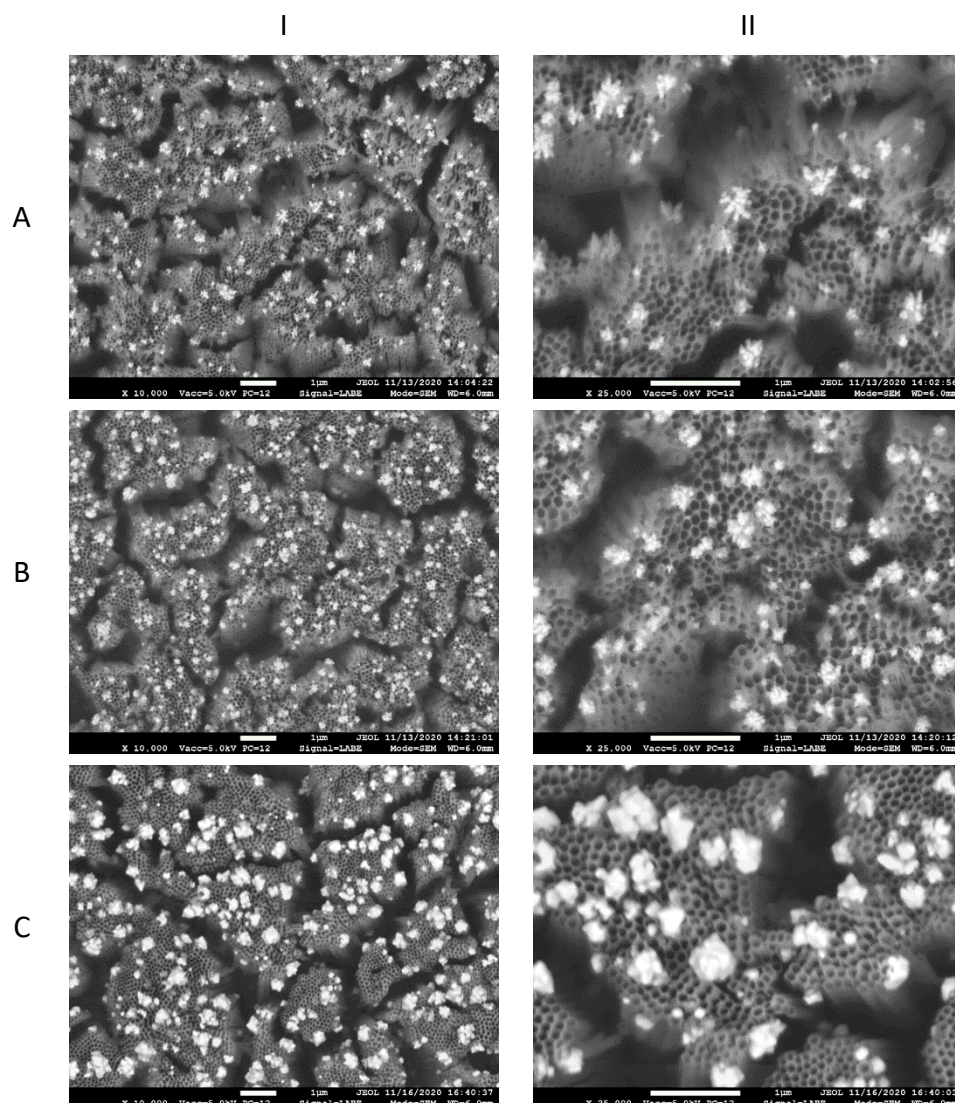


Figure 6-5: FESEM micrographs, at low (I) and high magnification (II), of TNTs after electrochemical deposition of Cu nanoparticles at -1 V vs Ag/AgCl for 90 s (A), 180s (B) and 180 sec with ultrasound (C).

6.1.1 Antibacterial activity of Zn and Cu-decorated TNTs

The antibacterial activity of Zn and Cu decorated TNTs (TNT-Zn and TNT-Cu, respectively) was determined through the quantification of viable *S. epidermidis* cells in suspension (Figure 6-6 a), and viable bacteria adhered to the samples (Figure 6-6 b), as described in section 2.8.2. After 2h of incubation of the bare Ti samples, the total count in live bacteria cells in suspension (Fig. 6-6 a) was of about 2.19×10^5 CFU/ml, which is in line with the initial inoculum of 2×10^5 CFU/ml. Moreover, the number of live adhered *S.*

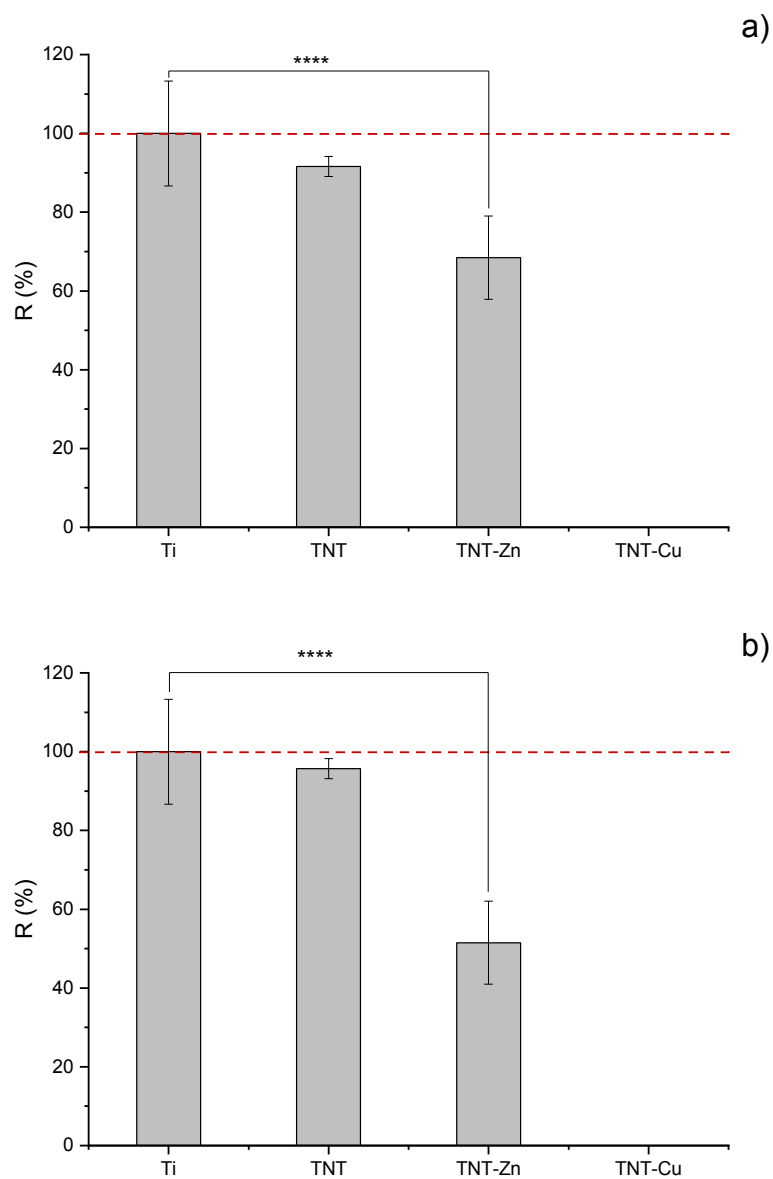


Figure 6-6: Antibacterial efficiency of TNT functionalized with ZnO (TNT-Zn) or copper (TNT-Cu) compared with as-polished Ti6Al4V alloy (Ti) and anodized and heat-treated Ti6Al4V (TNT), against *S. epidermidis*. (a) planktonic bacteria viability (b) adherent bacteria viability. The data is expressed as means \pm standard deviations (n=5). One-way Anova test was utilized to determine the level of significance against Ti samples: * $p < 0.1$, ** $p < 0.01$, *** $p < 0.001$, **** $p < 0.0001$.

epidermidis to the surface of the sample was of about 7.81×10^3 CFU/cm² (Fig. 6-6 b). This is in line with previous reports^[2] that state the capacity of these bacteria strain to abundantly adhere to the surface of bare Ti. The cell viability of Ti, either in suspension or adhered, was considered as base for the calculation of the percentage of all viable cells for all the other samples. The presence of non-functionalized nanotubes does not seem to have any effect on the bacteria survivability in suspension, with a count of viable cells of 2.08×10^5 CFU/ml or approximately 91.62%, in the medium. Similarly, adhered live bacteria was of about 7.5×10^3 CFU/cm² for the anodized sample, or approximately 95% of R(%) value. In general, these results indicate that anodization of Ti6Al4V, particularly the particular dual-morphology of TiO₂ nanotubes (with 70-100 nm diameter in the α -phase), does not seem to inhibit the adhesion of cells to the surface of the metal.

On the other hand, both TNT-Zn and TNT-Cu showed a remarkable bactericidal effect. The viable cells in suspension in PBS, after 2 h of incubation with TNT-Zn, was significantly reduced to 1.50×10^5 CFU/mL, only 68.46 % of those of Ti (Fig. 6-6 a). Similarly, the number of viable bacteria adhered to the surface of the sample was only of 4.02×10^4 CFU/ml, only 51 % of the viability of adhered cells to Ti (Fig. 6-6 b). The susceptibility of *S. Epidermidis* to TNT-Zn (in the range of 5.2 wt.%) is in line with previous report of Roguska *et al.*. In this work this authors also reported, surprisingly, that a higher amount of Zn led to loss of antibacterial effect, which the authors attributed to the resulting surface morphology due to deposition of higher amount of ZnNPs on the surface.^[2] An even greater effect was obtained TNTs-Cu samples, which led to 100 % loss of bacterial availability, in both planktonic or adhered bacteria. The higher antimicrobial effect of Cu, when compared to Zn, is reported in the literature^[3] and was to be expected.

6.2 Electroless deposition of Ag

Figure 6-7 shows the surface of TNTs after electroless deposition of silver nanoparticles (AgNPs) preformed under different conditions (see 2.7.2). Figures 6-7 a and b were obtained after anodized samples were incubated in the silver amine complex solution for 20 min, under magnetic stirring. These micrographs revealed that silver did not form a continuous layer but an inhomogeneous film on top of the tubes, with AgNPs aggregated in island-like clusters. Figures 6-7 c and d were obtained after anodized samples were incubated in silver amine complex solution for 15 min, under ultrasounds. The micrographs show that the distribution of the AgNPs were more uniform, with the particles attaching to the inner walls of TNTs and

along the top walls of the tubes. Thus, submitting to ultrasounds during the incubation step allowed for a more fine distribution of AgNPs than magnetic stirring.

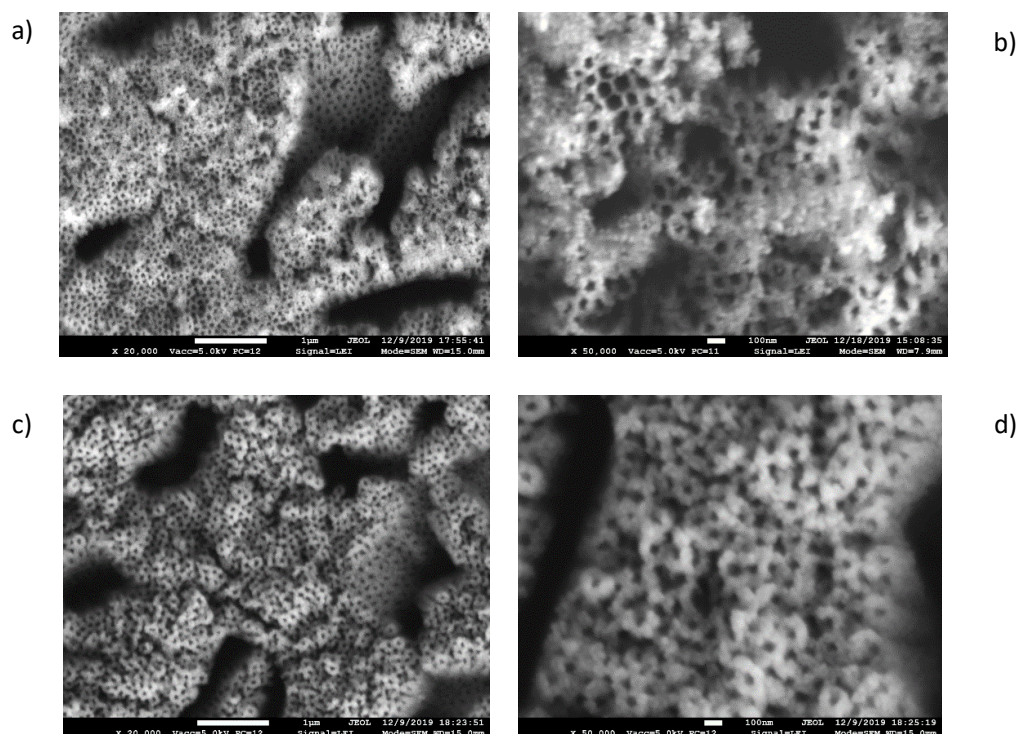


Figure 6-7: FESEM micrographs of silver nanoparticle on TiO_2 nanotubes, grown on Ti6Al4V alloy, prepared with different exposure times to the silver amine complex solution, under distinct stirring conditions and different reduction times. (a) low and (b) high magnification prepared after 20 min incubation and 1 min deposition, under stirring. (c) low and (d) high magnification prepared after 20 min incubation and 3 min deposition, under ultrasounds.

Nevertheless, a substantial accumulation of silver at the tube tops is still observed for the deposition performed in ultrasound. Through EDXS analysis, the amount measured was of 23.66 wt.%, too high for biocompatibility purposes. Silver is known of its high cytotoxic effect, having maximum antimicrobial action at very low concentrations.^[3] Thus, in attempt to decrease the excessive deposition of silver, two further, alternative, optimization steps were performed. In the first, the silver amine complex solution was filtrated and in the second, 1:10 dilution of the solution was performed, before incubation of the samples. Figure 6-8 shows the effect of these two steps on the morphology of the deposited AgNPs. Filtration effectively reduced the amount of silver deposited and allowed a uniform distribution, with very fine particles attached to both the top and inner surface of the tubes (Fig 6-8 a and b). The amount

measured was of about 8wt%. On the other hand, the dilution of the silver-amine solution, resulted in clusters of about 250 nm in diameter, that are distributed over the tube tops. The deposited silver was of about 4 wt.%. Due to the low amount achieved under these conditions, they were selected for biocompatibility and antimicrobial assays.

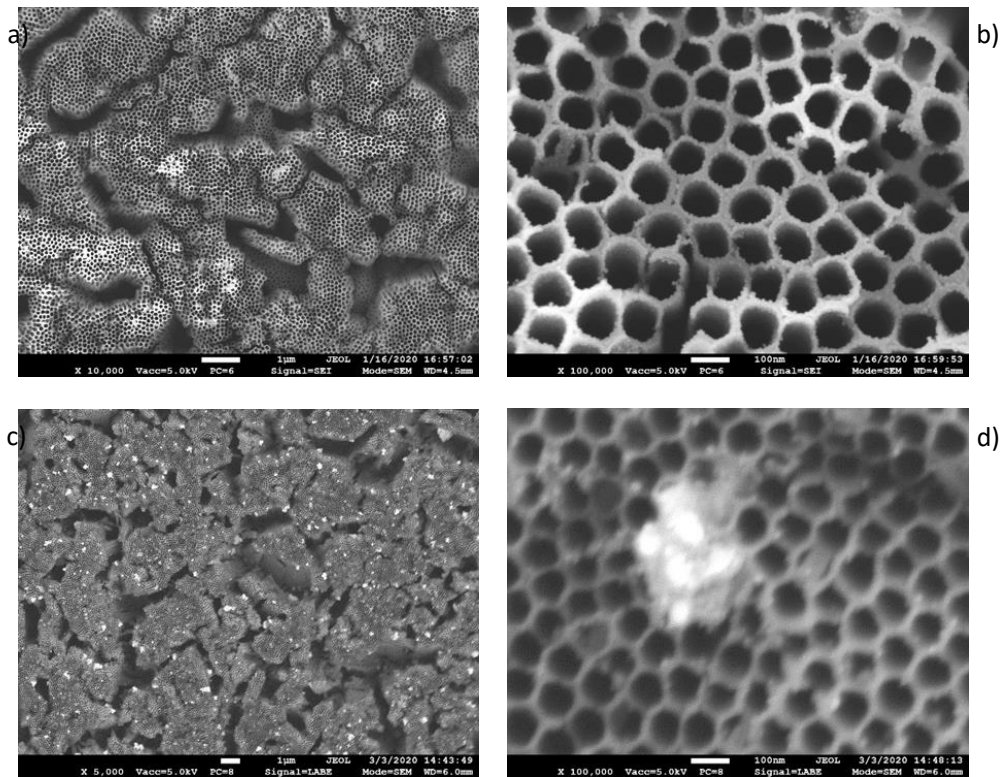


Figure 6-8: FESEM micrographs of silver nanoparticle on TiO_2 nanotubes, grown on Ti6Al4V alloy, prepared with different exposure time to the silver amine complex solution, under distinct stirring conditions and different times of reduction. (a) low and (b) high magnification prepared after 20 min incubation and 1 min deposition, under stirring. (c) low and (d) high magnification prepared after 20 min incubation and 3 min deposition, under ultrasonics.

6.2.1 Biocompatibility of TNTs-Ag

Figure 6-9 a shows the relative amount of lactate-dehydrogenase (LDH) released by viable MG63 cells adhered to the surface of the bare Ti6Al4V (Ti), Ti functionalized with silver (Ti-Ag), Ti anodized and heat-treated Ti6Al4V (TNT), and TNT functionalized with 4% and 8% silver (TNT-Ag-low and TNT-Ag-high respectively). All values are reported with respect to the

viability measured for bare Ti6Al4V alloy. The TNT samples present a 22% higher cellular viability. This could be attributed to the both the diameter and the anatase crystalline phase of the TNT sample. Thus these results support that the fabrication of TiO₂ nanotubes with a diameter of 70-100 nm, improves the bioactivity the Ti6Al4V alloy, which enhanced cell metabolic activity. On the other hand, the incorporation of silver on nanotubes leads to 51% reduction (for 4 wt.% of deposited silver, TNT-Ag-low) or 69% reduction (for 8wt.% of deposited silver, TNT-Ag-High) on the metabolic activity of MG63 cells. These results could indicate that the amount of deposited silver is toxic for bone cells. Nevertheless, it is important to consider that MG63 cells are derived from human-osteosarcoma, and not from healthy bone tissue. Thus, although they may offer an indication of the behavior of healthy osteoblasts, these cells may present susceptibility to silver, which is regarded as an anti-cancer agent.^[4]

Curiously, the addition of silver to the bare Ti grade 5 alloy (Ti-Ag), only led to a reduction of 34% in MG63 cell viability. It is possible that the unique morphology of nanotubes, together with change in surface energy, potential or chemistry provided by the deposited AgNPs somehow affected the adhesion of cells perhaps by important factors such as protein adsorption. On the other hand, the hollow nature of tubes may also lead to accumulation of a higher amount of silver which can potentially explain these results.

6.2.2 Antimicrobial activity of TNT-Ag

The antibacterial activity of Ag-decorated TNTs was assessed by determination of contact-killing action, through the count of viable *S. epidermidis* cells adhered to the samples, as described in section 2.7.2. For TNT-Ag, incubation with bacteria was preformed in the Müller Hinton Broth growth media, instead of PBS as described in 6.1.1. According to De Leersnyder *et al.* the use of complete growth media, leads to higher cell survival and higher concentrations of antimicrobial agent are necessary to obtain similar results obtained minimal support solutions such as PBS.^[5] Given that silver is generally regarded as a highly effective inorganic antimicrobial agent, potent at very low amounts, when compared with other solutions such as Cu or Zn, a complete growth medium was chosen in order to highlight it's effects.^[3] The results are reported in Figure 6-9 b. The viability of bacteria is represented in terms of percentage with regard to the viability of *S. epidermidis* cells adhered to the bare Ti6Al4V samples. After 2h of incubation in Müller-Hinton Broth the amount of adhered bacteria on the bare Ti6Al4V (Ti) was of about $9,38 \times 10^4$ CFU/cm² (Figure 6-9 b). In anodized samples (TNT), bacterial cells present a 34.32% higher viability, with 2.31×10^5 CFU/cm² of adhered cells.

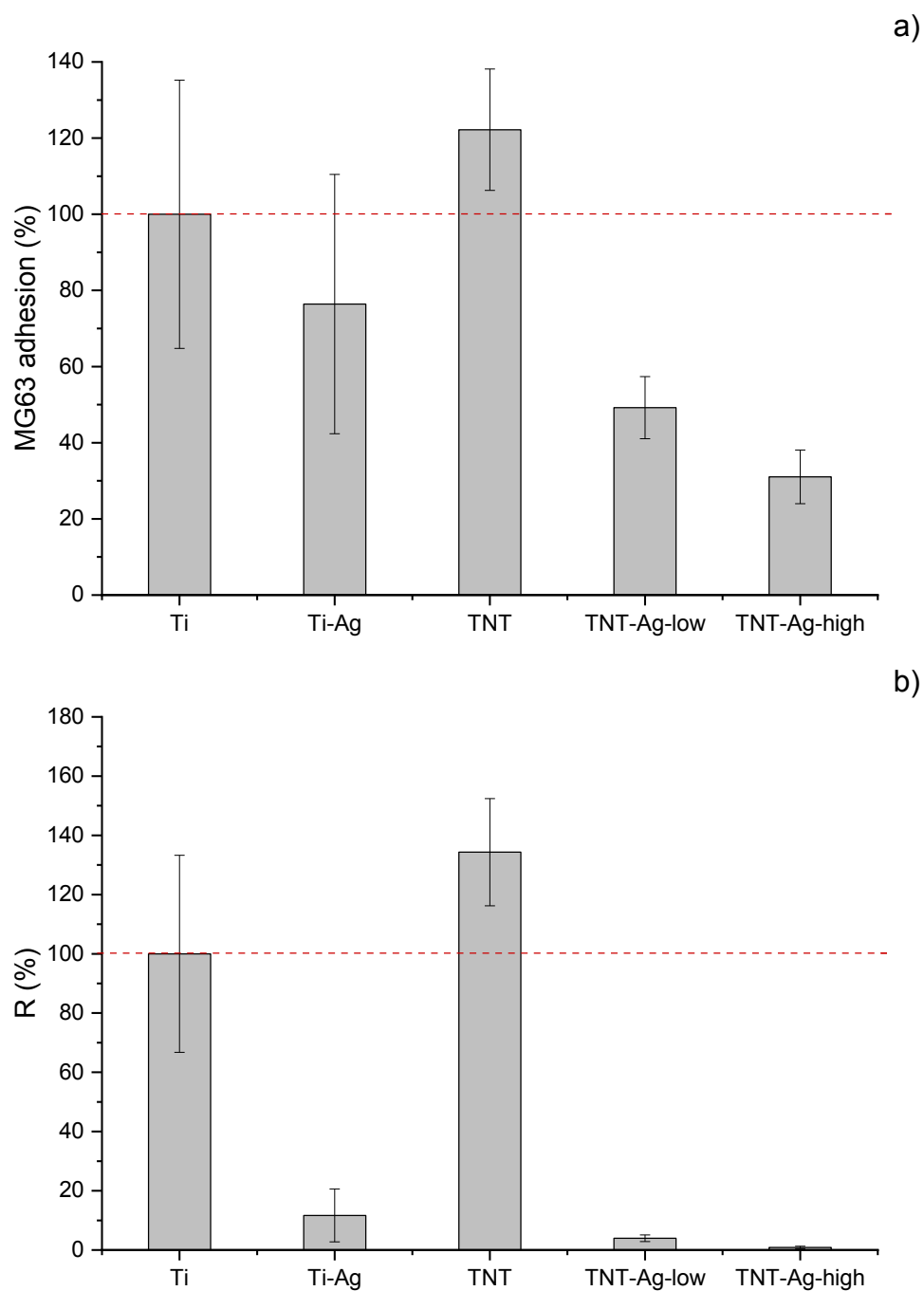


Figure 6-9: (a) MG63 cell viability and (b) antibacterial efficiency against *S. epidermidis* of Ti6Al4V functionalized with silver (Ti-Ag), anodized Ti6Al4V (TNT), anodized titanium functionalized with either 4wt.% (TNT-Ag-low) and with 8wt.% (TNT-Ag-high). All percentages were calculated with regard to the cellular viability (a) or bacterial viability (b) measured in bare Ti6Al4V (Ti). The data is expressed as means \pm standard deviations (n=5).

These could be attributed to the same factors that also lead to a higher bone cell viability, namely, increased protein accumulation on tube tops.^[6] In the presence of silver however, there was a sharp reduction in bacteria viability. The TNT-Ag-low solution presents a reduction of 94% of bacterial viability, to 1.99×10^3 CFU/cm², while for TNT-Ag-high the reduction is of 99%, remaining only 4.39×10^2 CFU/cm². Moreover, the Ti_Ag sample presents a reduction of 87%, with only 4.88×10^3 CFU/cm². These results show the high susceptibility of *S. epidermidis* against silver, which is further enhanced by the presence of nanotubes. As described previously, it is possible that the hollow nature of the tubes allows for a higher amount of silver to be incorporated, when compared to the flat bare sample. Alternatively, as described in section 6.2.1, it could also be that both incorporation of AgNPs and tube morphology play a synergistic role that influences cellular adhesion to the substrate. AgNPs could be responsible for altering the surface energy and potential characteristics of nanotubes, which would influence protein adsorption and hinder bacterial adhesion.

6.3 Partial Conclusions

In this part of the work, functionalization of TNTs produced on Ti6Al4V alloy, with the most effective inorganic antimicrobial agents, namely Zn, Cu and Ag, was thoroughly described. For Zn and Cu, decoration of annealed TNTs was achieved through an electrochemical deposition process, after determination of the ideal potential for deposition (considering a target amount of around 4-10wt.%). In general, under optimized conditions, the obtained samples show nanoparticles or nanocrystals grown on top of the tubular layer for both Cu and Zn. Other factors, such as temperature or ultrasound stirring did not allow for a finer distribution along the tube walls. On the other hand, Ag was deposited through an electroless deposition process. In general, the produced nanoparticles were very fine and had a much lower size than crystals/nanoparticles obtained in the deposition of Zn and Cu. Moreover, the application of ultrasound was essential to achieve a very uniform distribution along the tubular walls. Filtration of silver-amine complex solution was necessary to effectively reduce the amount of deposited silver. In general, it can be concluded that the electroless deposition process allowed for a more ideal distribution of antimicrobial agent along the tube morphology, with the ultrasound mixing being an important parameter to achieve and more uniform distribution of the deposited silver.

Antimicrobial assays performed on these samples confirmed that functionalization by these agents showed a high antibacterial activity, especially Ag and Cu, with a lower, but still significant activity being measured for Zn. On the other hand, the presence of nanometric scale morphology of the tubes did not seem to have any antimicrobial effects, with the bacteria grown on complete Müller Hinton Broth presenting instead an increased adhesion. However, the deposition of Ag over TNTs shows an increased antimicrobial activity (above 95% reduction in bacterial viability) if compared to the deposition of Ag over bare Ti6Al4V (only 87%). This could be attributed to the hollow structure of the TNTs which could contain higher amount of Ag. Nevertheless, Ag has shown to also strongly inhibit viability of MG63 cells, although this could be attributed to specific anticancer potential of Ag that on cytotoxic potential to healthy bone cells. On the other hand, osteoblast-like MG63 cells revealed an increased metabolic activity (up to 22% more) than the ones adhered to the flat Ti sample. Thus, the presence of nanotubes seems to provide some degree of bioactivity to Ti grade 5 with potential for antimicrobial action if functionalized with antimicrobial agents. Thus, a process optimization with low amounts of Ag could offer an equilibrium between the osteogenic effect of nanotubes and antibacterial performance of Ag.

6.4 Bibliography

1. Zoolfakar AS, Rani RA, Morfa AJ *et al.* Enhancing the current density of electrodeposited ZnO-Cu 20 solar cells by engineering their heterointerfaces. *J Mater Chem* 2012;**22**:21767–75.
2. Roguska A, Belcarz A, Pisarek M *et al.* TiO₂ nanotube composite layers as delivery system for ZnO and Ag nanoparticles - An unexpected overdose effect decreasing their antibacterial efficacy. *Mater Sci Eng C* 2015;**51**:158–66.
3. Lemire JA, Harrison JJ, Turner RJ. Antimicrobial activity of metals: mechanisms, molecular targets and applications. *Nat Rev | Microbiol* 2013;**11**,
4. Majeed S, Bakhtiar NFB, Danish M *et al.* Green approach for the biosynthesis of silver nanoparticles and its antibacterial and antitumor effect against osteoblast MG-63 and breast MCF-7 cancer cell lines. *Sustain Chem Pharm* 2019;**12**:100138.
5. De Leersnyder I, De Gelder L, Van Driessche I *et al.* Influence of growth media components on the antibacterial effect of silver ions on *Bacillus subtilis* in a liquid growth medium. *Sci Rep* 2018;**8**, DOI: 10.1038/s41598-018-27540-9.
6. Jäger M, Jennissen HP, Dittrich F *et al.* Antimicrobial and osseointegration properties of nanostructured titanium orthopaedic implants. *Materials (Basel)* 2017;**10**:1–28.

7 FINAL REMARKS

In this work, a surface modification for both Cp-Ti (ASTM grade 2) and Ti6Al4V (ASTM grade 5) alloys, was designed to provide antimicrobial activity to their surface, without hindering neither the native corrosion resistance of the base alloys, nor their good biocompatibility. This surface modification consisted of TiO₂ nanotubes decorated with selected inorganic antimicrobial agents, namely Zn, Cu and Ag. In this system, the TNTs act as reservoirs for the agents, providing both an active antimicrobial action, through a release-killing mechanism, and a passive antimicrobial action, through contact-killing mechanisms. Moreover, these nanotubular structures provide nanotopographical features that improve osteoblast-like cell adhesion. To achieve this purpose, three main targets were defined on this project:

- Production of TiO₂ nanotubes through electrochemical anodization and process optimization to obtain reproducible results and inner tube diameters between 70 and 100 nm, to improve osteointegration;
- Investigation into thermal modification of the crystalline structure of the produced TNTs, and their effect on the corrosion resistance of the alloys;
- Decoration of TNTs with inorganic antimicrobial agents, namely, Zn and Cu, through electrochemical deposition processes and Ag through an electroless deposition process, and test of their antimicrobial activity against a common implant-related infection pathogen, *S. epidermidis*, and human osteoblast-like MG63 cells.

Electrochemical anodization has been demonstrated to be an easy, controllable process, which allowed producing well-defined and well-adhered TNTs on the surface of Ti alloys. Tubes with an inner diameter between 70 to 100 nm, were achieved at an applied potential difference of 40 V for 6 h for Ti grade 2 and of 60 V for 1 h for Ti grade 5. Ageing of the electrolyte and definition of a specific applied potential and time, for each alloy, was necessary to achieve reproducible results. In general, it was observed the chemical composition has a great influence on the morphology and growth of the nanotubes, with single crystalline α -phase Ti grade 2 (about 99.8% of Ti), presenting an overall slower morphological development, requiring longer times to achieve nanotubular definition, when compared with Ti6Al4V alloy. This could be attributed to a higher electrochemical stability of

Ti in fluoride containing electrolytes, when compared to either Ti-Al, or Ti-V in Ti grade 5. This notion is further supported by the differences in overall morphology obtained for both alloys. While an uniform tubular morphology was obtained, under optimized conditions, for TNTs grown over Ti grade 2, TNTs with dual-morphologies were grown over the two phases of the Ti grade 5 alloy, for any given voltage or time, with nanotubes grown over the β -phase being shorter and with thicker walls. Thus, nanotubular development is ultimately dependent on the specific susceptibility of the substrate to the chemical etching by the fluorides in the electrolyte.

Both alloys were shown to possess a passive behavior, with a wide passive range, in physiological solutions, through potentiodynamic polarization measurements. Electrochemical anodization and nanotube production on their surface did not affect their corrosion behavior, overall. On the other hand, as-anodized TNTs were shown to be amorphous and a heat-treatment preformed in air, at 500°C for 3 h, has been shown to be an effective way of inducing their crystallization into an anatase phase, without affecting nanotubular morphology. Nevertheless, a thermal oxide was formed between the tubes and the metal substrate, which was amorphous in Ti grade 5, but with a rutile crystalline phase in Ti grade 2. This could be due to the different chemical composition of the alloys, more specifically, the presence of the alloying element Al in Ti grade 5 which has been described to inhibit the crystallization process and phase transition of TiO_2 .^[1,2] In general, heat-treatment led to a decrease in the passive current density for both alloys, but at a potential of 1.2-1.3 V vs Ag/AgCl both alloys suffer a breakdown of the passive layer, which is attributed to the thermal oxide formed. While Ti grade 2 repassivates, the Ti grade 5 alloy undergoes corrosion. To avoid this, a similar heat treatment was performed under vacuum conditions, and while it prevented the formation of the thermal oxide, it was not able to induce crystallization of the anodic oxide on Ti grade 5 and led to the loss of the passive behavior of both alloys. Thus, considering the human body potential range, heat-treatment at 500°C in air is the most effective way to induce crystallization of TiO_2 nanotubes.

Neither anodization, nor heat-treatment, provided Ti grade 2 or Ti grade 5 with antimicrobial action against *S. epidermidis* bacteria, whose viability was affected only when Cu, Zn or Ag were incorporated in anodic oxide. Both the electrochemical deposition of Zn or Cu, and the electroless deposition of Ag processes, under optimized conditions, allowed the decoration the nanotubular structures without affecting their morphology. On the other hand, the presence of crystalline TNTs on the surface of Ti grade 5 has been shown to increase human-osteoblast-like MG63 viability. However, these cells were seriously affected by the

incorporation of silver, and a decrease in the incorporated amount of this agent (from 8 wt.% to 4 wt.%) has been shown to greatly improved the viability, while maintaining a similar antimicrobial action. Thus, it is possible that further optimization of the amount of Ag incorporated into TNTs, can allow an ideal viability of MG63 cells while maintaining a strong antimicrobial action.

In general, the fabrication of TiO₂ nanotubes, with an anatase phase, through electrochemical anodization followed by annealing at 500°C for 3h in air, has been shown to be an effective, and cost-effective solution to provide both a reservoir for antimicrobial agents and a bioactive surface for improved bone cell adhesion. Moreover, the incorporation of inorganic antimicrobial agents through electroless or electrochemical deposition allows to successfully functionalize this bioactive surface against *S. epidermidis*.

7.1 Suggestions for future work

The aim of this work was to describe the production of TiO₂ nanotubes through electrochemical anodization on both Cp-Ti and Ti6Al4V in terms of influence of process parameters on nanotube morphology, obtained structure and it's tailoring through controlled heat treatments, and the effect that these treatments had on the corrosion resistance of the alloys. Moreover, this work provided some initial results on the potential of techniques such as electrochemical and electroless deposition with inorganic antimicrobial agents and their antimicrobial performance. Thus, there is so much more that could be researched in the future to further complete this work:

- Further optimization of the deposition of Ag, through electroless deposition, or Zn and Cu, through electrochemical deposition, into the nanotubular structures in order to achieve even higher antimicrobial action and better biocompatibility;
- Deposition of Ag, Cl, Zn through other deposition methods such as hydrothermal deposition, atomic layer deposition, chemical vapor deposition, ion implantation or sputtering, and comparison of the results in terms of amount deposited, morphology and cost;
- Testing, considering the well-known broad antimicrobial spectrum of inorganic agents, the produced surfaces against other types of microorganisms such as gram-positive bacteria, or fungus such as *Candida*;
- Testing of the produced nanotubes against other bone cell types such as MSC cells or MC3T3-E1 pre-osteoblast cells. It is important to consider that MG63 cells are

derived from carcinoma and silver is known for being a potential anti-cancer agent, thus the reported loss of viability of these cells could be attributed to the anticancer activity of silver (even though other osteosarcoma derived cells, such as SAOS-2 have been demonstrated to not be negatively affected by the presence of silver);

- Testing of the produced TNTs, functionalized with Ag, Zn and Cu in terms of antibiotic release over time (doing a leachate test over several days, and assessing the amount released through techniques such inductively coupled plasma atomic emission spectroscopy, ICP-AES) and their resistance against common sterilization procedures applied in orthopedic implants, which comprise physical methods such as UV, gamma or plasma irradiation or heat treatments wither under wet or dry conditions, as required by the European Agency for Evaluation of Medicinal Products.^[3]

7.2 Bibliography

1. Hanaor DAH, Sorrell CC. Review of the anatase to rutile phase transformation. *J Mater Sci* 2011;**46**:855–74.
2. Bayata F, Ürgen M. Role of aluminum doping on phase transformations in nanoporous titania anodic oxides. *J Alloys Compd* 2015;**646**:719–26.
3. The European Agency for the Evaluation of Medicinal Products Evaluation of Medicines for Human Use. *Decision Trees for the Selection of Sterilisation Methods.*, 2000.